



HAL
open science

Miniaturised Microwave Biosensor Conception and Implementation for Carotid Atherosclerosis Diagnosis

Rania Shahbaz

► **To cite this version:**

Rania Shahbaz. Miniaturised Microwave Biosensor Conception and Implementation for Carotid Atherosclerosis Diagnosis. Electronics. Sorbonne Université, 2023. English. NNT : 2023SORUS748 . tel-04692233

HAL Id: tel-04692233

<https://theses.hal.science/tel-04692233v1>

Submitted on 9 Sep 2024

HAL is a multi-disciplinary open access archive for the deposit and dissemination of scientific research documents, whether they are published or not. The documents may come from teaching and research institutions in France or abroad, or from public or private research centers.

L'archive ouverte pluridisciplinaire **HAL**, est destinée au dépôt et à la diffusion de documents scientifiques de niveau recherche, publiés ou non, émanant des établissements d'enseignement et de recherche français ou étrangers, des laboratoires publics ou privés.

Sorbonne Université

ED 391 - Sciences mécaniques, acoustique, électronique et robotique de Paris

(SMAER)

Génie Electrique et Electronique de Paris (GeePs)

CNRS - CentraleSupélec

Miniaturised Microwave Biosensor Conception and Implementation for Carotid Atherosclerosis Diagnosis

Par Rania SHAHBAZ

Thèse de doctorat de Science

Dirigée par Hamid KOKABI et Fabien KOSKAS

Co-encadrée par Jean-Michel DAVAINÉ, Frédérique DESHOURS et Georges
ALQUIE

Présentée et soutenue publiquement le 29 Juin 2023

Devant un jury composé de :

Rapporteurs :

M. COSCAS Raphaël, Professeur à l'Université de Versailles-Saint-Quentin-en-Yvelines,
Université Paris-Saclay - Praticien Hospitalier à l'Hôpital Ambroise-Paré - AP-HP

Mme RICHALOT Elodie, Professeure à l'Université Gustave Eiffel (ESYCOM)

Examineurs :

Mme DESHOURS Frédérique, Maîtresse de Conférences à Sorbonne Université (GeePs)

M. ESCARGUEIL Alexandre, Professeur à Sorbonne Université, Centre de Recherche Saint-
Antoine

Mme GRENIER Katia, Directrice de recherche CNRS, Laboratoire d'Analyse et
d'Architecture des Systèmes (LAAS)

M. KOKABI Hamid, Professeur à Sorbonne Université (GeePs)

M. KOSKAS Fabien, Professeur, Société d'exercice libéral à responsabilité limitée (SELAR)

Mme VIGNERAS Valérie, Professeure à l'École Nationale Supérieure de Matériaux,
d'Agroalimentaire et de Chimie (INP)

Invité :

M. DAVAINÉ Jean-Michel, Maître de Conférences à Sorbonne Université - Praticien
Hospitalier à l'Hôpital Pitié Salpêtrière - AP-HP

Dédicace

إلى مملكتنا الغالية التي جعلت الحياة أجمل وسهّلت دروب النجاح والخير، وجعلت الأمن والأمان عنوانًا دائمًا في كلّ يوم.
كلمات الثناء لا توفيك حقك.
شكرا على عطائك.

Ma chère France, merci de m'avoir accueillie et aimée. Je te serai toujours reconnaissante.

Acknowledgements

This PhD has been a truly life-changing experience for me, and it would not have been possible without the encouragement and support of many people.

This journey and success would not have been possible without the scholarship program that I was granted by the Ministry of Education in Saudi Arabia to do my PhD in France.

I do not have the words to express my gratitude to Prof. F. Koskas for believing in me and proposing me this thesis and for our insightful conversations; it has been an honour.

I would like to thank Prof. H. Kokabi for allowing me to participate in this project and trusting and supporting me along the way.

I am very grateful to Dr F. Deshours and Prof. G. Alquie (my microwave/electronics parents) for always being there when I needed their support, reviewing my progress constantly, and guiding me through my PhD studies. Without your help, this would not have been possible.

Special thanks to Dr J-M Davaine for all the direction, mentoring, encouragement, counselling and brilliant criticism (&for your patience!). I will never forget your support and the valuable discussions we had along the road.

I would also like to extend my thanks to Dr E. Charpentier, Prof. I. Brocheriou and Mr G. Lenaour for all the assistance and outstanding advice.

I am also grateful to Dr M. Ponnaiah, who has offered me invaluable statistical recommendations and took the time to help me with my data.

It was a pleasure collaborating with Mrs J. Masini, Mr Y. Chatelon, Prof. G. Sou, Miss C. Hamel-Dellenbach and many others in our lab who did everything they could to support my PhD trip.

I would like to acknowledge my advisor in the Cultural Office of the Embassy of the Kingdom of Saudi Arabia, Dr J. Alsheibani, for his constant assistance throughout this PhD.

My besties in Saudi, my dear Parisians, my London family, my colleagues in the lab and my friends all over the world, I know I wasn't always the best at keeping in touch during my PhD (probably the worst), and I can't thank you enough for your patience. I feel so lucky to have such amazing friends who were always willing to listen, provide advice, and cheer me on during my PhD journey. Thank you for being such an important part of my life.

Cyprien, je ne sais pas comment j'en serais arrivé là sans toi. Merci d'avoir cru en moi, même quand je n'arrivais plus moi-même à croire que je pouvais y arriver. Tes mots doux et ta confiance en moi m'ont inspiré. Merci d'être qui tu es.

I finish with Saudi, where the most fundamental source of my life energy resides: My family. Their support has been unconditional all these years, and I need to thank them in Arabic now:

اخوتي الكبرى روان واخواني عمر وعبدالله وعبدالعزيز أنتم السند والقوة، في كل ثانية من وجودكم في حياتي وجدت النور والأمل شكرا على دعمكم

إذا علمتني مرحلة الدكتوراه أي شيء، فقد علمتني كيف كانت تربيته استثنائية. ماما وبابا أنا مدينة لكم بكل الخير في حياتي
بعد الله. لقد منحتوني العالم حقًا
شكرا على إيثاركم غير المشروط ، ودعمكم وصبركم ودعائكم وتضحياتكم التي لا تعد ولا تحصى التي فتحت لي العديد
من الأبواب للنمو والنجاح، وجميع الأشياء الصغيرة والكبيرة التي علمتموني إياها على طول الطريق. رسالة الدكتوراه هذه
منكم ولكم يانور عيوني

Table of Contents

Acknowledgements	2
List of abbreviations	7
Summary	10
Résumé	11
General Introduction	12
Chapter I - An Overview of Atherosclerotic Stenosis of the Carotid Artery: Clinical Presentation, Diagnosis, and Management Strategies	15
<i>1.1. Prevalence, aetiology, and diagnosis</i>	15
<i>1.2. The role of generally available diagnostic imaging techniques</i>	23
<i>1.2.1. Pre-op</i>	24
<i>1.2.2. Post-op</i>	37
<i>1.3. Synopsis of the advantages and disadvantages of each approach</i>	39
<i>1.4 Conclusion</i>	41
Chapter II - Microwave Technology in Medicine: Emerging Applications and Advancements	42
<i>2.1. State-of-the-art of Radio Frequency (RF) applications in medicine</i>	43
<i>2.1.1. History</i>	43
<i>2.1.2. Overview of the Microwave systems</i>	47
<i>2.2. Biological tissues dielectric model</i>	56
<i>2.2.1. Debye model and Cole-Cole equation</i>	56
<i>2.2.2. Microwave interaction with heterogeneous biological tissues</i>	59
<i>2.2.3. Permittivity profile and dielectric properties of biological tissues from current databases</i>	61
<i>2.3 Conclusion</i>	66
Chapter III - Implementation and Development of the Miniaturised Microwave Sensor Forethought for Diagnostic Purposes	67
<i>3.1. Microwave measurement instrumentation</i>	67
<i>3.2. Microwave Systems for dielectric constant measurement</i>	69
<i>3.3. Sensor design and fabrication process</i>	74
<i>3.3.1 Resonant technique with planar sensor</i>	74
<i>3.3.2 Sensor design</i>	75

3.4. Equivalent electrical model of CSRR	77
3.5. Adaptation of the sensor for biological tissue measurement.....	79
3.6. Calibration of the sensor with ideal samples.....	81
3.7 Conclusion.....	83
Chapter IV - Exploring Atherosclerotic Carotid Plaques Through Multiple Modalities: Medical Imaging, Histology, and Microwave Biosensor	84
4.1. Study design.....	84
4.2. CT	85
4.3. DUS	88
4.4. CEA.....	89
4.5. Surgical observation score	90
4.6. Histopathology	91
4.7. Microwave	94
4.8. Conclusion.....	100
Chapter V: The Outcomes of Experiments Conducted on Atheromatous Carotid Plaques.....	101
5.1. Statistical Comparison of Imaging and Histopathological Techniques for the Evaluation of Carotid Artery Disease	101
5.1.1 DUS vs Histology results	105
5.1.2 CT vs Histology & DUS results	109
5.1.3. Microwave CSRR biosensor vs Histology and radiological imaging modalities .	113
5.2 Multivariate analysis and multimodel prognostic score to predict VPs	115
5.3. Interpretation of the results in light of previous research.....	117
5.4 Conclusion.....	124
Chapter VI - Moving Beyond the Single Layer: Navigating the Transition to in-vivo Multilayer Models	126
6.1 Animal tissues.....	127
6.2 Multilayer model	132
6.3 Phantoms	137
6.4 Conclusion.....	141
Conclusion & Perspectives.....	142
Bibliography	144
Publications associated with this research.....	161
Appendix 1	163
Appendix 2.....	164

Appendix 3.....	165
List of figures.....	166
List of tables.....	170
Résumé	171

List of abbreviations

ACAS:	Asymptomatic Carotid Atherosclerosis Study
ACE-I:	Angiotensin-Converting Enzyme Inhibitors
ACST:	Asymptomatic Carotid Surgery Trial
ADS:	Advanced Design System
ARB:	Angiotensin Receptor Blocker
ARFI:	Acoustic Radiation Impulse Force Imaging
ASA:	American Stroke Association
BB:	Beta Blocker
BMT:	Best Medical Therapy
CA:	Carotid Artery
CAD:	Coronary Artery Disease
CAS:	Carotid Artery Stenosis
CCA:	Common Carotid Artery
CCPS:	Cathepsin Cysteine Proteases
CEA:	Carotid Endarterectomy
CECU:	Contrast Enhanced Carotid Ultrasound
CHF:	Coronary Heart Failure
CPW:	Co-Planar Waveguide
CSRR:	Complementary Split Ring Resonator
CT:	Computed Tomography
CTA:	Computed Tomography Angiography
DALYS:	Disability-Adjusted Life Years
DICOM:	Digital Imaging and Communications In Medicine
DNA:	Deoxyribonucleic Acid
DSA:	Digital Subtraction Angiography
DUS:	Doppler Ultrasound
ECEA:	Eversion Carotid Endarterectomy
ECST:	European Carotid Surgery Trial
EM:	Electromagnetic
EMC:	Electromagnetic Compatibility
ESVS:	European Society of Vascular Surgery
ETSI:	The European Telecommunications Standards Institute
FDG:	Fluorodeoxyglucose
GBD:	Global Burden of Diseases, Injuries, And Risk Factors
GHz:	Gigahertz
GSM:	Greyscale Median
HDL-C:	High-Density-Lipoprotein Cholesterol
HFSS:	High-Frequency Structure Simulator
HIFU:	High-Intensity Focused Ultrasound
HR-MRI:	High Resolution Magnetic Resonance Imaging
HSCRP:	High Sensitivity C-Reactive Protein

HU:	Hounsfield Unit
ICA:	Internal Carotid Artery
ICG:	Indocyanine Green
ICT:	Imagerie Cardiovasculaire et Thoracique
IEEE:	Institute of Electrical and Electronics Engineers
IFAC:	Italian National Research Council Database
IJV:	Internal Jugular Vein
IL-1 β :	Interleukin-1 β
IL-6:	Interleukin6
INSERM:	Institut National de la Santé et de la Recherche Médicale
IPH:	Intraplaque Haemorrhage
IR:	Infrared
ISM:	Industrial, Scientific, And Medical
ITIS:	Information Technologies in Society
LDL-C:	Low-Density Lipoprotein Cholesterol
LP:	Lipid Pool
LPKF:	Leiterplatten-Kopierfräsen
LPPLA2:	Lipoprotein-Associated Phospholipase A2
LRL:	Line-Reflect-Line
LRNC:	Lipid Rich Necrotic Core
MATX:	Matrix
MDCT:	Multidetector Computed Tomography
MHz:	Megahertz
MMP:	Matrix Metalloproteinase
MPRAGE:	Magnetization-Prepared Rapid Gradient-Echo
MRA:	Magnetic Resonance Angiography
MRI:	Magnetic Resonance Imaging
MSI:	Mass Spectrometry Imaging
MUT:	Material Under Test
MWI:	Microwave Imaging
NASCET:	North American Symptomatic Carotid Endarterectomy Trial
NIRF:	Near-Infrared Fluorescence
NVE:	Neo vessels from the Endothelium
NVP:	Non-Vulnerable Plaque
NVV:	Neo vessels from the Vasa Vasorum
OAT:	Oral Anticoagulant Therapy
OCT:	Optical Coherence Tomography
OM:	Osteoid Metaplasia
OMT:	Optimal Medical Therapy
OPG:	Osteoprotegerin
OX-LDL:	Oxidized Low-Density Lipoprotein
PAD:	Peripheral Arterial Disease
PAT:	Photoacoustic Tomography
PCB:	Printed Circuit Boards

PC-CT:	Phase-Contrast Computed Tomography
PDA:	Pixel Distribution Analysis
PET:	Positron Emission Tomography
PFA:	Perivascular Fat Attenuation
PTFE:	Polytetrafluoroethylene
PVFA:	Perivascular Fat Attenuation
RBS:	Rutherford Backscattering Spectrometry
RF:	Radio Frequency
RLC:	Resistor (R), Inductor (L), Capacitor (C),
ROI:	Region Of Interest
SAA:	Serum Amyloid A
SAR:	Specific Absorption Rate
SCM:	Sternocleidomastoid Muscle
SIMF:	Service d'Imagerie Morphologique et Fonctionnelle
SMA:	Sub Miniature Version A
SMCS:	Smooth Muscle Cells
SRR:	Split Ring Resonator
SWE:	Shear Wave Elastography
TAI:	Thermoacoustic Imaging
TCFA:	Thin-Cap Fibro-Atheroma
TIA:	Transient Ischemic Attack
TNF α :	Tumour Necrosis Factor
TOSM:	Through – Open – Short – Match
TRL:	Through-Reflect-Line
TRM:	Through-Reflect-Match
US:	Ultrasound
VA:	Veterans' Affairs
VEGF:	Vascular Endothelial Growth Factor
VNA:	Vector Network Analyser
VP:	Vulnerable Plaques
YM:	Young's Modulus

Summary

Microwave imaging has gained significant attention in the field of medical imaging due to its ability to penetrate through the body and differentiate the dielectric properties of human tissues and hence distinguish abnormal tissues from healthy ones.

This thesis uses a miniaturized microwave biosensor that can quantify the relative permittivity of biological tissues. This kind of biosensor exhibits desirable features such as portability, simplicity of design, low cost, and lack of risk to the healthcare provider and the patient. This miniaturized CSRR biosensor has been developed to quantify the composition of atherosclerotic plaques in the carotid artery locally.

Initial tests with the sensor were performed on fifty carotid artery atherosclerotic plaques. Histological analysis of those lesions, CT and ultrasound scanning of the corresponding patients were performed to validate the sensor's findings. A comprehensive statistical analysis was performed to correlate the microwave results to histology and compare them with current radiological modalities. In addition, the biosensor was employed to characterize a variety of animal biological tissues representing the human neck model. Thereupon it was tested on a human neck phantom. Preliminary data were compared with results from electromagnetic modelling and 3D simulations of the biosensor loaded by the tested materials. Since the original sensor prototype was designed on a high-loss substrate, it had limited detection depth. Therefore, further CSRRs better suited to detecting in deeper tissues were developed simultaneously.

The simulation results for the microwave biosensor were almost equivalent to the actual data. Results showed that the microwave biosensor could distinguish between high-risk and low-risk carotid plaques and characterize individual biological layers but lacked precision for multilayer models. Despite facing several constraints, the miniaturized microwave biosensor can differentiate between diverse biological tissues. With the identification of the issues and obstacles, there is a possibility that a device suitable for in-vivo use in healthcare settings can be manufactured in the near future.

Résumé

L'imagerie par micro-ondes suscite une grande attention dans le domaine médical en raison de sa capacité à pénétrer dans le corps et à différencier les propriétés diélectriques des tissus humains, ce qui permet de distinguer les tissus anormaux des tissus sains. Dans cette thèse, un biocapteur micro-ondes miniaturisé, capable de quantifier la permittivité relative des tissus biologiques, est utilisé en raison de ses nombreux avantages tels que la portabilité, la simplicité de conception, le faible coût et l'absence de risques pour le praticien et le patient. Basé sur une structure CSRR, il a été développé pour mesurer localement la composition des plaques d'athérosclérose dans l'artère carotidienne.

Les premiers tests du capteur ont été effectués sur une cinquantaine de plaques d'athérosclérose de la carotide. L'histologie, le scanner et l'échographie des lésions des patients ont été effectués pour valider les résultats du capteur. Une analyse statistique complète a été réalisée pour corréliser les résultats des micro-ondes à l'histologie et les comparer aux techniques radiologiques actuelles. Par ailleurs, le biocapteur a été utilisé pour caractériser une variété de tissus animaux afin de simuler le modèle du cou humain. Il a aussi été utilisé par comparaison pour caractériser un fantôme de cou humain. Les données préliminaires ont été comparées aux résultats de la modélisation électromagnétique et des simulations 3D du biocapteur chargé par les matériaux testés. Le prototype original du capteur ayant été conçu sur un substrat relativement à forte pertes, sa sensibilité est limitée en profondeur et nécessite de développer d'autres CSRRs mieux adaptés à la détection de tissus plus épais.

Les résultats de simulation électromagnétique du biocapteur sont tout à fait comparables aux données expérimentales. Ils ont permis de montrer que le biocapteur pouvait distinguer les plaques carotidiennes à haut risque de celles à faible risque et caractériser les couches biologiques individuelles, mais qu'il manquait de précision pour les modèles multicouches.

General Introduction

The surgical indications for Carotid endarterectomy (CEA) have become ambiguous in recent years due to the progress in the Optimal Medical Therapy (OMT) of atherosclerotic vascular diseases. Therefore, developing new, non-invasive methods to gauge the vulnerability of carotid plaques and determine CEA indications is crucial. Histopathological analysis post-operation of the extracted plaque is currently the only method to describe its composition accurately. This shortage and need were presented by Prof. Koskas & Dr Davaine, vascular surgeons at Hôpitaux Universitaires Pitié Salpêtrière - Charles Foix, to Prof. Kokabi, Dr Deshours, and Prof. Alquie in GeePs laboratory. The latter team proposed their idea of a microwave biosensor for it to be developed and operated to distinguish atherosclerotic plaques in the carotid artery via the neck window. The fruit of this collaboration was this PhD. The sensor's concept is that it can distinguish biological tissues, such as fragile plaques, from calcified stable ones by measuring the difference in their dielectric constant. Thus, a vulnerable plaque would have a permittivity rating probably similar to blood, whereas a stable calcified plaque would most likely have a reading as low as bone.

The primary goal of the PhD was to evaluate the sensor's performance on ex-vivo carotid plaques and compare its results with histology and current radiological modalities such as Doppler Ultrasonography (DUS) and Computed Tomography (CT). The objective is to establish a link between them and histology, the current gold standard for characterising atherosclerotic plaque composition. Hounsfield Unit (HU) and Gray-Weale classification were used as markers in CT and DUS results, respectively. The calcification, fibrous cap and Lipid-Rich Necrotic Core (LRNC), and Introplaque Haemorrhage (IPH) levels were determined by semi-quantitative analysis for the histopathological findings. A microwave biosensor Complementary Split Ring Resonator (CSRR) was employed to analyse the carotid plaques ex-vivo via the s-parameters using the resonant technique to extract the relative permittivity by an Electromagnetic (EM) 3D software.

In order to correlate the biosensor results to histology and evaluate how these findings stack up against other radiological modalities, a complete statistical analysis was carried out. According to preliminary findings, two different clinical patterns of carotid lesions were observed. The first is defined by type 2&3 lesions according to Gray-Weale classification in DUS, more frequently symptomatic plaques and presenting higher values of dielectric constant in microwave analysis. This group comprised lesions significantly more likely to be vulnerable in histology. In contrast, the second group was characterized by type 4&5 Gray-Weale lesions, more frequently asymptomatic with lower dielectric constant values. This second group presented characteristics of a non-vulnerable plaque in histology. Moreover, it was possible to establish an algorithm based on the association of DUS and microwave imaging that is able to identify vulnerable plaques with high sensitivity and specificity.

The second part of the PhD saw the development of more concentrated measurements geared to regulating most parameters that can influence the dielectric constant observations. As a result, the new focus included managing and modifying factors, such as temperature, humidity and the pressure applied to the sample to present results of ex-vivo measures as close as possible to in-vivo values. These variables were monitored during some of the carotid plaque measurements. However, this original focus of the work on carotid plaques was limited by the COVID-19 pandemic (access to the hospital was restricted for several months, followed by a decrease in carotid artery operations due to a shortage of surgical theatres). Consequently, testing the layers preceding the carotid plaque was incorporated as a second objective of this doctorate. The bench-testing included multilayers of animal tissues simulating the neck, which were analysed on various occasions, followed by tests on human neck layers' phantoms.

Towards the end of this journey, this thesis focused on the following objectives (which a fellow doctoral candidate is pursuing), to reach the most appropriate sensor model by comparing various sensor sizes and substrates and evaluating the prototype using simulations and measurements. Modifications have been implemented to the initial structure to improve the sensitivity, resolution, and penetration depth of the EM waves in the human body at the neck level. In addition, the fact that the thicknesses of these tissues vary from one patient to the other

was considered. These improvements include the geometrical shape of the resonator, the substrate and the design frequency, and these investigation tracks have been exploited to design two other sensors based on CSRRs. Furthermore, to incorporate the sensor into a pressure control system that supports the user in monitoring and detecting the pressure applied to the tissue.

This thesis's first chapter includes a literature review on the necessity of a marker or technique that can safely and accurately define the composition and vulnerability of the carotid atherosclerotic plaque.

The second chapter of this thesis is the state-of-the-art of currently available microwave imaging biosensors and their strengths and weaknesses.

The third chapter provides an in-depth analysis of the electromagnetic simulations used to evaluate the microwave biosensor manufactured in our lab and the theory and technology underpinning it.

Methods and findings of the carotid plaque analysis are presented in chapters four and five, respectively.

In chapter six, the enhancements that were made to the method are discussed, as well as the testing of multilayer biological models, and suggestions are made for further improvements in the future.

Chapter I - An Overview of Atherosclerotic Stenosis of the Carotid Artery: Clinical Presentation, Diagnosis, and Management Strategies

Carotid atherosclerotic disease is characterised by plaque build-up in the arteries that supply blood to the brain. It is a common cause of ischemic stroke, which occurs when blood flow to the brain is blocked. The prevalence of atherosclerotic carotid disease increases with age and is more common in men than women. The incidence of stroke due to carotid artery disease has decreased in recent years due to improved management of risk factors such as hypertension, hyperlipidaemia and smoking.

The primary cause of atherosclerotic carotid disease is the collection of fatty deposits, cholesterol, and other substances in the walls of the carotid arteries. This accumulation can cause the artery to narrow, reducing blood flow to the brain. Other risk factors for developing carotid artery disease include diabetes and family history.

Carotid artery disease can be diagnosed using several methods, including physical examination, imaging studies, and blood tests. Imaging studies such as ultrasound, computed tomography, and magnetic resonance imaging can be used to evaluate the degree of stenosis or narrowing of the carotid arteries.

Treatment of carotid artery disease may include lifestyle changes such as quitting smoking, managing blood pressure and cholesterol and adopting a healthy diet and exercise regimen. Medication or surgery may be necessary to prevent stroke in more severe cases.

1.1. Prevalence, aetiology, and diagnosis

In 2017, according to the Global Burden of Diseases, Injuries, and Risk Factors Study (GBD), stroke was the third-leading cause of death and disability combined (as measured by disability-adjusted life years [DALYs]) and the second-leading cause of death in the world in 2017 [1] responsible for almost 12% of total deaths [2]. Contemporaneously with the GBD, the National Institute of Health and Medical Research (INSERM) [3] in France published that more than

140,000 new stroke cases are diagnosed annually in France. That is one stroke every four minutes. 20% of people who have a stroke do not live through the first year. This makes strokes the most common cause of acquired physical disability in adults and the second most common cause of dementia (after Alzheimer's disease) [3]. Incidence rates are found to be around 10 % in men and 6 % in women over the age of 80 [4].

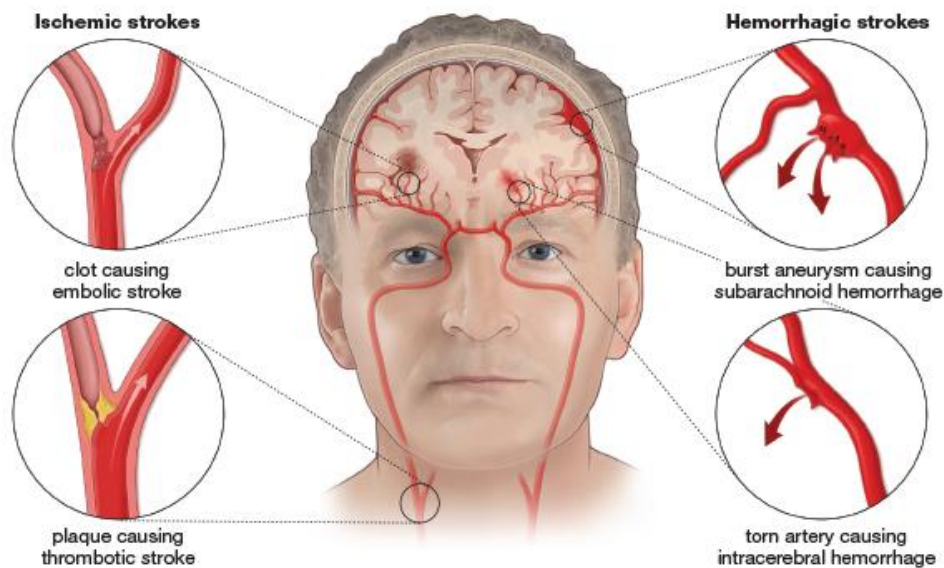


Figure 1. Types of strokes: Ischemic and Haemorrhagic [5]

The American Stroke Association (ASA) divides strokes into two types: ischemic and haemorrhagic (Fig.1). Ischemic stroke is the leading cause of new strokes (representing roughly 62% of all incident strokes in 2019). Haemorrhagic strokes include intracerebral haemorrhage, which comes after in prevalence (around 27%) and less common is subarachnoid haemorrhage (about 9%) [1].

In ischemic stroke, there is an abrupt interruption in blood flow to the brain, which is the defining feature of this type. Here, narrowing or blocking arteries that supply blood to the brain occurs. Ischemic strokes can be either thrombotic or embolic. When there is a blood clot in one of the arteries carrying blood to the brain, this is known as a thrombotic ischemic stroke. Atherosclerosis, fatty deposits lining the vessel walls, is the primary cause of ischemic thrombotic stroke, i.e. large-artery atherosclerotic stroke, e.g. carotid artery stenosis or occlusion (Fig.2). In embolic ischemic stroke, a portion of the blood clot dislodges, enters the

bloodstream, and travels through the brain's arteries until it reaches vessels too narrow to allow passage. Atrial fibrillation, an irregular heartbeat, is a leading cause of embolism. It can cause cardiac clots to detach and migrate to the brain [6], [7].

A haemorrhagic stroke happens when a brain blood artery ruptures or leaks. The two distinct types of haemorrhagic strokes mentioned above are intracerebral haemorrhage which occurs when a brain artery ruptures, filling the surrounding tissues with blood and subarachnoid haemorrhage, characterised by bleeding between the brain and the meninges [8], [9].

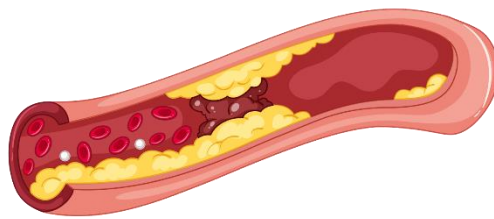


Figure 2. Fatty deposits lining the wall of the carotid artery.

Carotid Artery Stenosis (CAS) is the result of systemic atherosclerosis. Consequently, any risk factor predisposing a patient to progressive atherosclerosis may manifest as carotid artery stenosis. Risks include smoking, hyperlipidaemia, hypertension, heredity, male gender, and age [10]. Carotid artery occlusion is frequently asymptomatic and undiagnosed until it impairs blood flow to the brain [11]. In 2013, *Flaherty et al.* published their article on “Carotid Artery Stenosis as a Cause of Stroke”, which has been cited 343 times since. It was made clear that atherosclerosis of large cerebrovascular vessels is a significant cause of stroke and even results in the highest risk rate of early recurrent ischemia of any stroke subtype. Stroke risk factors can be classified into many categories, including large vessel atherosclerotic disease. CAS is a frequent medical problem. Experts speculate that atherosclerotic disease of the carotid arteries accounts for about 15–25 % of all cases of acute ischemic stroke and is also linked to an elevated risk of coronary events and vascular mortality [12]–[17]. In 2020, CAS was predicted to have a global incidence of 21.1% among adults aged 30-79 [18].

Diseases caused by CAS can be classified as either symptomatic or asymptomatic, with the distinction significantly impacting the course of treatment. When a patient has symptoms of CAS, like acute neurological ischaemia, Transient Ischemic Attack (TIA) or amaurosis fugax,

the patient is usually sent to the emergency room or seen as soon as possible by a vascular surgical service. Asymptomatic CAS, recognised after discovering a carotid bruit or as an incidental finding on imaging, is the second possible clinical scenario. In this context, the patient had no CAS symptoms until then [19].

Atherosclerotic lesions in the Internal Carotid Artery (ICA) form along the carotid bulb wall (Fig.3). An area of low wall shear stress, flow separation, and loss of unidirectional flow is produced by the extension of the bulb just distal to this major branch point. This likely accounts for the localized plaque at the carotid bifurcation by allowing higher interaction of atherogenic particles with the artery walls at this spot [20]. Because of its convenient location, this atheroma can be effectively treated by removing the plaque, drastically decreasing the patient's chance of having a stroke [20].



Figure 3. Anatomical dissection of a carotid bifurcation with an atherosclerotic plaque [21]

In 1954, with the first Carotid Endarterectomy (CEA), surgical prevention of stroke was first introduced. Multiple randomised trials published between 1995 and 2010 demonstrated that targeted intervention is the most effective way of treating CAS [19]. The preventative utility of CEA for symptomatic patients with CAS tighter than 70% as determined on angiograms was established in 1991 by the North American Symptomatic Carotid Endarterectomy Trial

(NASCET) and the European Carotid Surgery Trial (ECST). Furthermore, three other randomised clinical trials — the Veterans Affairs Cooperative Study (VA), the Asymptomatic Carotid Atherosclerosis Study (ACAS), and the Asymptomatic Carotid Surgery Trial (ACST) — established the benefit of CEA in patients with a 60-99% degree of asymptomatic CAS [22]. Asymptomatic patients with less than 49 % stenosis did not benefit from surgery [12], and [23] confirmed and suggested only medical therapy for asymptomatic patients with < 60% stenosis. In terms of the size and scope of their impact, those trials rank among the most often cited and influential to date.

Conventional angiography, the gold standard for assessing CAS for decades, was used as the imaging reference method in the NASCET, ECST, and ACAS trials. Since the advent of non-invasive alternatives such as Doppler Ultrasound (DUS), Magnetic Resonance Imaging (MRI) and Computed Tomography (CT), angiography has become less common in the research of carotid artery pathology [24], [25].

In most cases, the degree of stenosis in the ICA is measured using one of two methods: NASCET or ECST (Fig.4). The degree of stenosis can be quantitatively assessed by calculating the percentage by which the lumen's diameter has decreased relative to a reference site; in the case of the NASCET method, this reference site is the supra-bulbar internal carotid artery, while in the case of the ECST method, it is the stenosis site itself. The stenosis degree could vary depending on the technique used [26].

Patients that suffer from a stroke or TIA and have a severe (> 70%) extracranial ICA stenosis have a much lower chance of having another stroke if they have early revascularisation with CEA [27]. The main goal of surgery is to reduce the risk of a second stroke caused by an unstable plaque. A combined surgical and medicinal treatment plan lowered the risk of a second stroke [12]. Therefore, the gold-standard treatment for symptomatic CAS is CEA [12], [28], [29].

In 2003, [30] stated that the degree of CAS is the single most critical factor in determining the outcome of a CEA. Nevertheless, since then, improvements in medical therapy, such as statins, antithrombotic and antihypertensive medications, and lifestyle changes (such as smoking cessation, weight loss, healthy diet, and being more active) have helped lower the number of cerebrovascular events linked to CAS [22] which rendered the surgical treatment of CAS with

hemodynamic significance controversial [4]. The multiple reports of improved outcomes with medical therapy alone called into question the absolute incremental benefit of intervention to prevent stroke in asymptomatic individuals [19]. In the study by *Reiff et al.* on 513 patients published in *The Lancet* journal, they stated that the risk of any stroke, mortality within 30 days, or ipsilateral stroke during the 5-year monitoring period was not shown to be lower with CEA plus Best Medical Therapy (BMT) or carotid artery stenting plus BMT compared to BMT alone. However, they warned that due to the small sample size, it is critical to exercise caution when interpreting these findings [22].

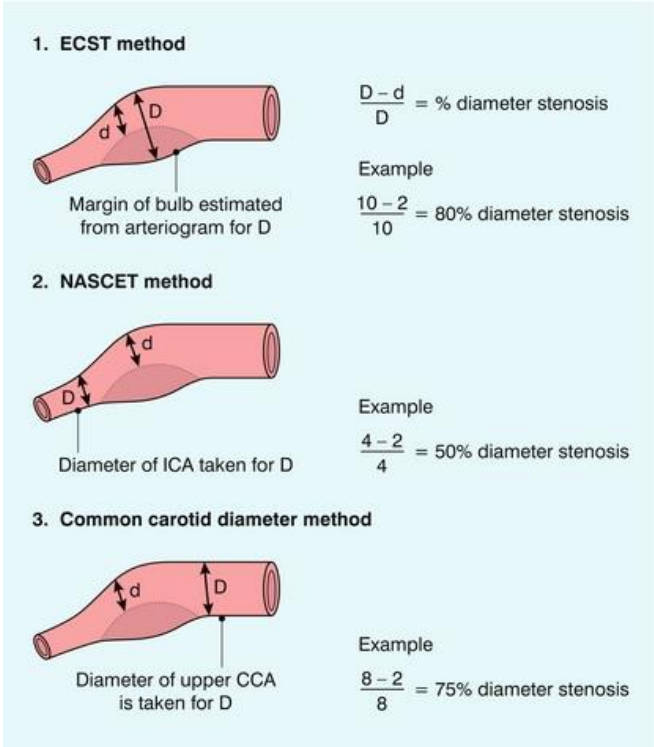


Figure 4. Differences between NASCET and ECST in the measurement of internal CAS [31]

CAS is a common cause of surgical intervention, and it is performed on many patients each year. Treating CAS via CEA or a stent can drastically reduce stroke risk. Nevertheless, stenting, though less invasive than surgery, presents significant risks regarding minor stroke; roughly 3 to 9% of patients undergoing interventional treatment are predicted to have a stroke or death due to such intervention [17], [32]. As aforesaid, about half of the people who have sudden strokes because of CAS become disabled or die. *Allison Halliday* argued that these people with

disabilities are not advised to have surgery or a stent to prevent future strokes. She also added that in spite of the fact that asymptomatic patients who have severe stenosis share risk factors with those with cardiovascular disease, widespread screening is not currently suggested. However, she insisted that there is still a need to identify high-risk patients who could gain from surgical intervention; these could be those who are less likely to take their medications as prescribed or who have long-term diseases like diabetes [33]. Improved cardiovascular risk management can be achieved by using risk prediction models to select individuals for focused screening to detect asymptomatic CAS [13]. *David Spence* added that individuals with asymptomatic CAS have a periprocedural risk of stroke or mortality of around 2.7% with carotid stenting and 1.5 % with CEA (i.e., well above that with BMT) [34].

Within the field of vascular surgery, the debate over whether or not to operate on patients who have no symptoms persists [35]. Although the data used in the landmark trials mentioned earlier is more than 20 years old, it still provides strong evidence for surgery for asymptomatic patients [36]. Patients whose surgeries are delayed, for example, during the first COVID-19 pandemic and lockdown, should have received excellent medical care and close monitoring as the consequences of postponed treatments are hard to evaluate because of the low rate of complications in asymptomatic individuals. Prospective stroke registries could be used in the future to evaluate the risks of delaying carotid revascularisation for symptomatic and asymptomatic stenosis [15].

Moreover, medical management has become increasingly influential since the 90s, particularly in treating hypertension, dyslipidaemia, and diabetes mellitus [12]. Currently, in asymptomatic individuals, the incidence of spontaneous stroke has been reduced by around 1% per year due to advances in medical treatments, suggesting that these patients can be managed appropriately without undergoing CEA [15]. In 2021, on behalf of the Oxford Vascular Study, *Howard et al.* published a population-based cohort study, systematic review, and a meta-analysis on the risk of stroke in relation to the degree of asymptomatic CAS and found that patients with high-grade stenosis who are treated with BMT have a significant risk of stroke; implying that the positive effects of surgical intervention may be understated. In addition, they questioned revascularization in individuals with moderate stenosis who are treated with BMT because of the low risk of stroke [37].

Furthermore, [38],[10], [12], [30], [39] warned that the degree of stenosis is not the only factor to consider when determining whether or not a carotid plaque poses a threat of distal embolization; other plaque features can either raise or decrease this risk. Carotid atherosclerosis characteristics, including luminal stenosis and surface irregularities, have traditionally been used to foretell ischemic episodes. For a long time, the degree of luminal stenosis has been a critical factor in deciding whether medicinal or surgical intervention is necessary to treat such lesions. Nevertheless, reliance on luminal stenosis as the key prognosticator for ischemic events has been called into doubt in recent years, as strokes have been observed in patients with mild to moderate CAS. The morphologic properties of plaques have instead attracted attention, with the hope that the presence or absence of certain susceptible elements inside a plaque could reveal important data about its stability [14], [16], [40].

When plaques in the carotid artery rupture, thrombus forms, and emboli travel to the brain, causing infarction. Therefore, knowing the stenosis and instability of the plaque is crucial to avoid stroke. Plaque rupture can be avoided with a proper diagnosis and treatment plan for Vulnerable Plaques (VP) [41].

[42] Identified Thin-Cap Fibro-Atheroma (TCFA) as a central component of an unstable, high-risk plaque prone to rupture, i.e. VP. They determined that an LRNC, inflammation, and a thin fibrous cap contribute to a plaque's fragility.

The role of VP has recently been emphasised, and some findings have shown that occurrences of cerebral ischemia in individuals with ICA lesions are not limited to cases with severe stenosis [43]. As a matter of fact, the degree of stenosis alone does not take into account the physiological, anatomical, and hemodynamic complexity of carotid atheromatous plaques [32], [44], [17]. It is publicly acknowledged that the composition of the plaque in terms of lipid, calcium, and/or fibrous tissue significantly impacts its clinical behaviour. In particular, the calcium component of an atherosclerotic plaque, both at the early and late stages of its formation, strongly influences the wall's stiffness, stability, and risk of rupture [45], [46]. Stroke risk is believed to be reduced in people with calcium-rich plaques, especially those located superficially [39]. Enhanced profibrotic pathways and decreased inflammation were observed in highly calcified plaques, a molecular signature predictive of plaque durability [47]. Further validating the relevance of plaque morphology in risk assessment of patients with CAS,

prediction modelling found that plaque composition, including LRNC, Intraplaque Haemorrhage (IPH) and Matrix (MATX), was superior to the degree of stenosis in predicting CAS symptoms [48].

Plaque morphology can be recognised to a limited extent using current imaging techniques, but information about molecular processes is only available through post-mortem or post-op study [17]. Currently, histopathology is the only recognised approach for identifying the composition of carotid artery plaques [18]. However, the plaque needs to be extracted to be examined, which disregards the purpose of this examination. Current medical research acknowledges TCFA, LRNC, and the presence of IPH as the best markers of vulnerability [49], [38], [43]. Therefore, there is an urgent need for high-performance imaging techniques to detect VP, yet no one approach or morphological marker is universally approved [4], [48]. Conventional imaging methods for atherosclerosis have mainly concentrated on characterising anatomic aspects of the atherosclerotic plaque instead of pathophysiological processes [17]. Various studies have compared imaging results to the histological findings regarding plaque morphology and composition. The following section will provide specific information regarding imaging characteristics linked with VP using the most prevalent imaging modalities.

1.2. The role of generally available diagnostic imaging techniques

The 2023 guidelines from the European Society of Vascular Surgery (ESVS) recommended the assessment of additional plaque parameters with the radiological techniques currently in use in the case of high-risk asymptomatic patients. This gives credibility to the hypothesis that non-invasive imaging of carotid plaque morphology may one day lead to improved risk prediction based on plaque features rather than the degree of stenosis only [48], [47] (Table 1).

Table 1. ESVS listed the imaging features associated with an increased risk of stroke in patients with asymptomatic 50-99% CAS treated medically [47]

Imaging parameter	Stenosis severity in %	Annual rate of ipsilateral stroke
Plaque area on computerised ultrasound plaque analysis	70-99	< 40 mm ² : 1.0% 40-80 mm ² : 1.4% >80 mm ² : 4.6%
JBA on computerised ultrasound plaque analysis	50-99	<4 mm ² : 0.4% 4-8 mm ² : 1.4% 8-10 mm ² : 3.2% >10 mm ² : 5.0%
IPH on MRI	50-99	
Plaque lucency on DUS	50-99	Predominantly echolucent: 4.2% Predominantly echogenic: 1.6%
≥1 spontaneous MES during ≥1 h TCD monitoring	50-99	
Spontaneous embolization plus uniformly or predominantly echolucent plaque	70-99	Yes: 8.9% No: 0.8%
JBA = Juxtaluminal Black Area; MES = Microembolic Signals; TCD = transcranial Doppler.		

The pros and cons of the methods employed to identify the carotid plaque's composition pre and post-operation are presented and addressed in the next paragraph.

1.2.1. Pre-op

A. Ultrasound

DUS is the primary imaging modality for assessing CAS today [47] in spite of the fact that the degree of stenosis was mainly determined by angiography in the large landmark trials, e.g. NASCET and ECST [50], [51]. High-resolution ultrasound is a valuable tool for the characterisation of plaque structure. Most studies performed so far on ultrasonographic plaque morphology agree that anechogenic (weakly reflecting ultrasound) or heterogeneous plaques

(presenting with a complex pattern of echogenicity and with at least one hypoechogenic area) carry a higher risk of subsequent neurological symptoms in comparison with echogenic (strongly reflecting ultrasound) or homogeneous ones (plaques with a uniform texture). A classification known as the Gray-Weale classification is used to group atherosclerotic plaques using DUS according to their heterogeneity [35], [52], [53].

Further, a few studies determining the surface characteristics of the plaque in ultrasound have found that irregularity and ulceration were also associated with an increased risk of subsequent stroke [52]. [53] Reviewed eight DUS studies examining abnormalities in the plaque's luminal surface. DUS had a relatively low sensitivity (60%) for detecting ulcers, but surface roughness was more reliable (97% sensitivity, 81% specificity). With a sensitivity of 47% and a specificity of 63%, the European Carotid Plaque Study Group employed B-mode scan to detect ulcerated plaque. Five investigations yielded varying findings with a modest increase in average sensitivity (60%, from 38% to 94%) and specificity (74%, from 38% to 92%). [54] directly compared CT and DUS and found that CT was more accurate at detecting plaque ulceration than DUS (sensitivity 93.8% vs 37.5% and specificity 98.6% vs 91.5%) [55]. A direct comparison between CT and DUS for detecting plaque haemorrhage was published by [56], showing that CT is more reliable for diagnosis (sensitivity 100% vs 78.2% and specificity 70.4% vs 59.2%).

DUS is an easily accessible, reliable, low-cost, and valuable method for making a definitive diagnosis, ranking the risk of stroke, and deciding on a course of therapy for patients with CAS. Subjectivity and operator dependence, notwithstanding, remain its primary limitations. Moreover, carotid DUS has its own restrictions. It is rather difficult to scan in a "hostile" neck, and often, the results are uninformative in the case of high bifurcation above the level of the mandibular angle. In the event of a heterogeneous plaque, it is quite difficult to estimate its vulnerability. It is frequently hard to tell if it is a fibrotic or lipidic plaque when it is a homogeneous plaque, as fibrous plaques that are uniformly distributed can exhibit poor echogenicity, which can be misinterpreted as a soft plaque constituted of a liquid component. Moreover, in the case of calcified plaques, the visualisation is limited due to acoustic shadowing, which makes it difficult to assess the inner segments. Further, ultrasonic waves may

be significantly reflected at the interface of soft and hard segments in a complex atherosclerotic plaque, leading to an underestimate of the plaque's volume [55], [57].

In the 2000s, objective ultrasound assessments were developed to avoid subjectivity and to ensure 100% reproducible results. The computer-assisted method called Texture Analysis was established to characterise the plaque constituents and objectively measure changes in the plaques. Several methods exist today, but the Grayscale Median (GSM) remains the main one. It is the most frequently studied, and it calculates the frequency distribution of grey pixel values within the plaque. For example, a GSM value of 0 to 5 is assigned to blood and a GSM value of 185 – 195 to adventitia using linear scaling [58]. Those mathematical parameters computed from the distribution of pixels characterise the texture type and, thus, the underlying structure of the objects shown in the image (Fig.5).

It is worth noting that these threshold values differ from one study to another. In a study on 52 patients, plaques with GSM < 32 had a higher incidence of cerebral infarction than those above this value [59]. Correlations between GSM values and histopathological findings ranged from 46% to 75% in computer-assisted assessments of DUS images [17]. Histological analysis of carotid plaques removed at the surgery has shown that plaques with a low grey scale value have more lipid deposition and haemorrhage. By contrast, echo-rich plaques contain more fibrous tissue [60]. GSM and Juxtaluminal Black Area (JBA) can be employed to visualize the histopathological markers of VP, such as ulceration and IPH, validating their potential value as clinical and research surrogates for plaque vulnerability. However, GSM and any other Texture Analysis method used depend evidently on initial machine settings; therefore, there is a lack of reproducibility, which can be noted across the variable cut-offs in the literature used to determine vulnerable/stable plaques. In addition, GSM analysis uses only a single longitudinal slice and requires post-processing software like Adobe® Photoshop®.

Improvements in other fields of DUS include Contrast Enhanced Carotid Ultrasound (CECU), developed lately and used to visualise the adventitial vasa vasorum and intraplaque neovascularization. Hyperplasia of adventitial vasa vasorum and intraplaque neovascularisation have been shown to be essential features in plaque development. Furthermore, analyses of unstable carotid lesions demonstrated that the presence of IPH and microvessel density were directly associated with plaque rupture.

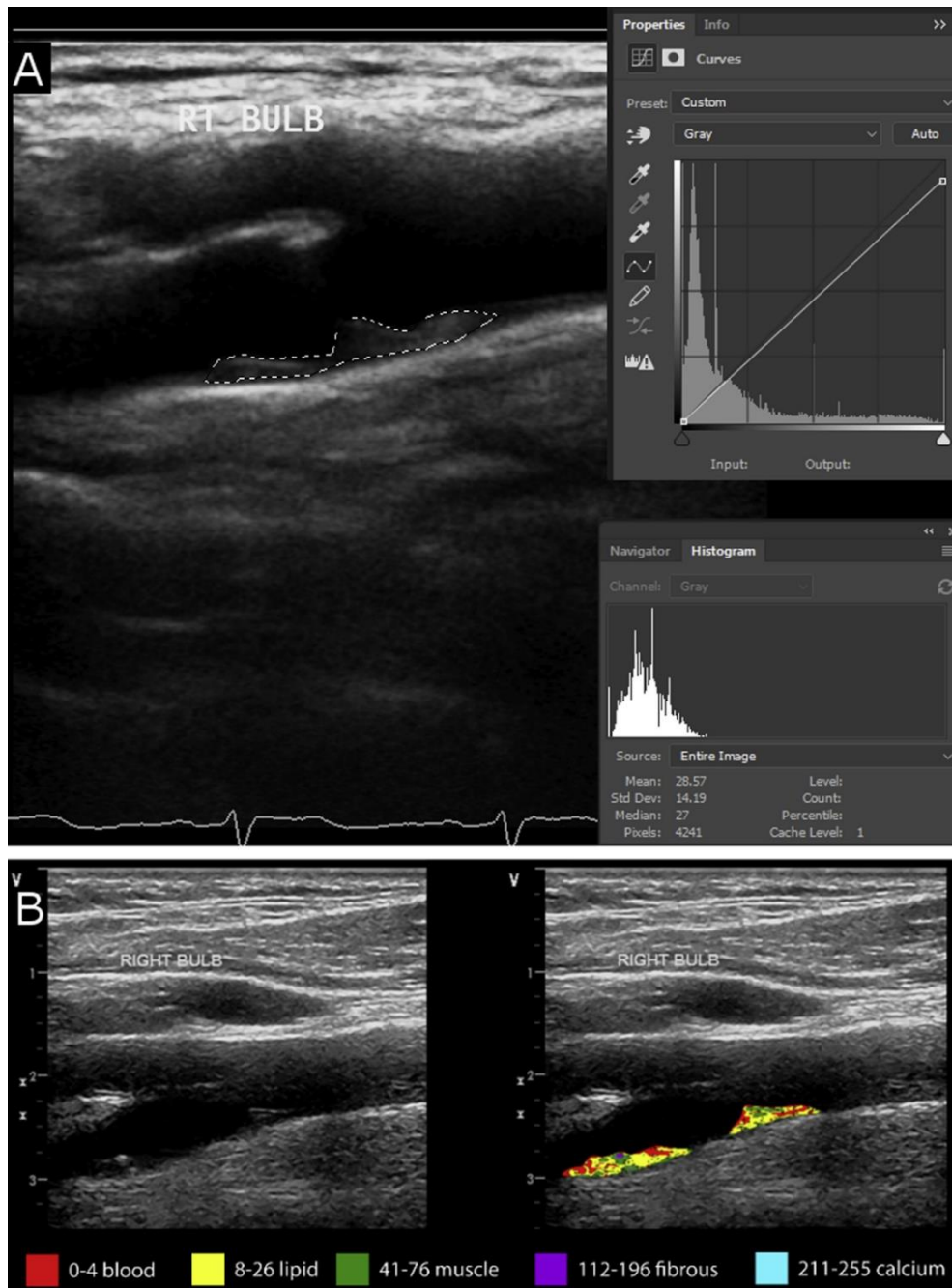


Figure 5. Plaque composition analysis by GSM and Pixel Distribution Analysis (PDA) [61]

It was reported that symptomatic atherosclerotic carotid plaques were associated with abnormal and immature intraplaque microvessels and noted that such vessels could contribute to plaque friability by promoting vascular leakage and deposition of inflammatory cell recruitment within the plaque [62]. Recent studies confirmed an association between intraplaque

neovascularisation, plaque vulnerability and cardiovascular events. A positive correlation between the histological density of neovessels and the presence of neovascularisation in carotid plaques was detected by CECU [62]. Therefore, using CECU imaging may provide a non-invasive adjunctive "window" to stratify VP and may serve as a valuable screening tool to identify patients at high risk of CAS symptoms. Nonetheless, this method necessitates alterations to the technical/power configuration of the ultrasound machine in addition to the administration of ultrasound-enhancing agents [63].

Carotid strain elastography, Shear Wave Elastography (SWE) and Acoustic Radiation Impulse Force Imaging (ARFI) are recent ultrasound methods that can assess the mechanical properties of the arterial wall. ARFI exploits acoustic radiation force to generate shear wave propagation in tissue. SWE has been shown to provide information regarding plaque stiffness with lower Young's Modulus (YM) associated with VPs [64]. Combining these ultrasound techniques may provide information on the arterial wall's composition (including inflammation) and mechanical properties. High strain values are associated with softer plaques.

In conclusion, adding computed greyscale analysis of plaque to DUS examinations and/or strain imaging/ARFI could assist in identifying individuals who may benefit from more concentrated management to halt or prevent future risk of stroke and silent stroke due to the presence of VP.

B. Computed Tomography Angiography

Computed Tomography Angiography (CTA) and Magnetic Resonance Angiography (MRA) are the best available non-invasive imaging modalities for the assessment of CAS, as both techniques have been validated against the gold standard, i.e. Digital Subtraction Angiography (DSA). Morphological parameters such as lumen abnormalities (stenosis, aneurysm or occlusion) and arterial wall characterization are evaluated using CT and MRI. MRI is the modality of choice to characterize the arterial wall [41] due to high tissular contrast, while CT is routinely used to visualise the arterial lumen abnormalities preoperatively.

CTA enables fast and isovolumetric high-resolution images with excellent contrast enhancement in the lumen to quantify luminal stenosis. In addition to stenosis measurements, carotid plaque composition can be assessed using CT attenuation related to the difference in X-ray attenuation. Radiologists employ Hounsfield Unit (HU), a relatively quantitative radio

density assessment, in their CT scan analysis. In CT reconstruction, greyscale images are created using the radiation absorption/attenuation coefficient within a tissue. Tissue density directly correlates to how much an X-ray beam is weakened by its presence [65]. Plaque composition is reflected in the HU value; lower HU values are linked to an increased likelihood of unstable plaques with LRNC and IPH [66].

With an overall agreement of roughly 75% between CT results and histology, CT has also been demonstrated to identify plaque ulceration, calcification, and lipid cores [17]. The seminal work by [67] established three types of carotid artery plaques based on their attenuation values: lipid (<60 HU), mixed (between 60 and 130 HU), and calcified (>130 HU). It might even be possible to extrapolate the true impact of the IPH component with the help of volumetric quantification analysis methods and a newly proposed CT threshold (25 HU of attenuation) for the identification of IPH [38]. However, the plaque's HU value might vary greatly depending on the keV chosen. The HU-based classification of plaque (lipid, mixed, calcified) should be made in relation to the energy level used [68]. Furthermore, a meta-analysis done on 36 articles by [69] found that a consistent and accurate method of characterising non-calcified plaque based on HU values has yet to be developed. Significant variation exists between the reported plaque-specific HU values (Fig.6). Lumen contrast enhancement and reconstruction kernel are known parameters affecting HU values of non-calcified plaque.

Due to variations in examination type, vessels of interest, and CT scanning, there are no universally accepted criteria for characterising non-calcified plaques based on CT attenuation value. That is why relying on averages in the clinic is not recommended. Reference CT attenuation values of lipid-rich and fibrous plaques can be determined for the local setting using the proposed hierarchical classification by [69]. In addition, CT is affected by artefacts such as calcium blooming, poor soft tissue contrast, and overlapping material densities from LRNC and IPH [48].

Recently, multiple studies in cardiovascular imaging [70], [71] demonstrated the role of Perivascular Fat Attenuation (PVFA) as an imaging biomarker of inflammation which is correlated with adverse outcomes, in particular for ischemic cardiopathies [70], [72]. For carotid atherosclerosis, the HU value of the perivascular fat surrounding ICAs on routine CT imaging could be used as a non-invasive biomarker to detect fat inflammation and vulnerable

plaque. Histopathologic markers of inflammation, such as elevated levels of pro-inflammatory cytokines and macrophage activity, have been demonstrated to correlate closely with increased perivascular fat density [73]. Previous work [74] showed that symptomatic patients had a higher PVFA in patients referred for severe CAS. The ipsilateral ICAs in patients with stroke or TIA had considerably higher peri-carotid fat density than ICAs in healthy individuals. HUs were substantially higher near stenotic ICAs than nonstenotic ICAs in the same subject [74]. While there is growing evidence that CT-based approaches can be used to assess risk factors associated with carotid plaque, the relevance of CT in assessing fat changes next to the arterial wall remains unclear.

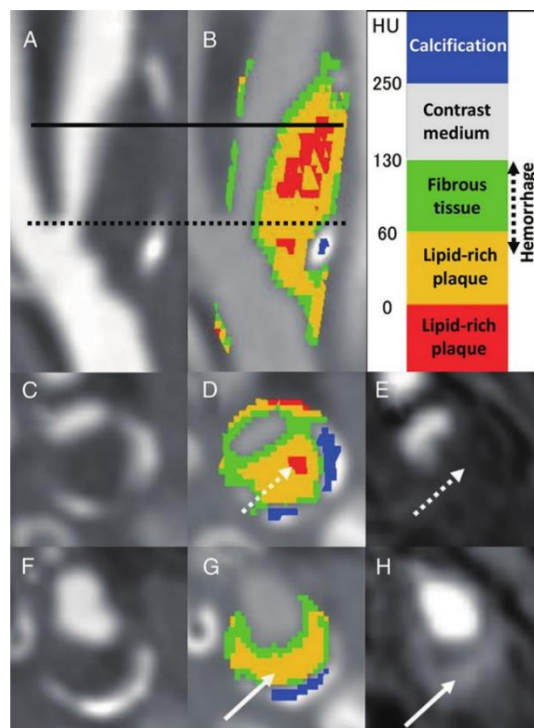


Figure 6. On a colour map of the HU (B) at the same level as a sagittal section of carotid artery stenosis (A), the inner area of plaque was colour-coded based on the HU. An HU of 130–250 reflects contrast medium in the vascular lumen. Of solid-line sections (C) source image, (D) colour map, (E) time-of-flight image, there was no IPH on the time-of-flight image, and CT showed a red area with an HU of ≤ 0 (dotted arrows). Of dotted-line sections (F) source image, (G) colour map, (H) time-of-flight image, intraplaque haemorrhage was detected on the time-of-flight image. CT confirmed the disappearance of the area with an HU of ≤ 0 (arrows) [75].

Variability in Region Of Interest (ROI) placement can impact density measurement on CT. Comparing HU values between patients may be hindered because HU measurements taken on different CT scanners across platforms can impact the HU values. It could make it more challenging to establish a single threshold number to signify inflammation [74]. In this regard, [39] suggested that automated classification algorithms like the one given in their study may help enhance plaque characterisation's reproducibility and may be beneficial in investigations tracking the development of atherosclerotic disease over time. The carotid wall image is processed by an automated classification computer system to determine the "type" of each image pixel (connective tissue, LRNC, IPH, and calcifications) [39]. Computer-aided linear discrimination analysis demonstrated excellent detectability of LRNCs with and without IPH by integrating early and delayed post-contrast CT data. The good detectability of the "double cut-off" method indicated that it is utilisable in clinical practice, but due to the limited sample size, it was not possible to recommend a specific cut-off CT value or line [41].

Another recently proposed solution is the grating-based Phase-Contrast CT (PC-CT) of arteries via high photon energy, which yields high-quality soft tissue contrast. At both 23 keV and 53 keV, PC-CT successfully differentiated arterial wall layers in healthy arteries. Phase contrast imaging has the potential to be used for in-vivo imaging of atherosclerosis, and the application of high photon energies is a necessary step toward this. However, many other technical challenges must be resolved first, including the scan time, motion artefacts and the radiation dose that must be lowered to safe levels [16].

In the ESVS journal, VasCuCAP software was proposed to analyse reconstructed pictures. With this programme, it is possible to generate 3D segmentations of soft tissue plaques with higher resolution and better component distinction. Restoring picture intensities and allowing differentiation between tissue types like LRNC and IPH is possible using a patient-specific 3D point spread function. Nevertheless, the study's design and cohort prevent its findings from being implemented in clinical settings [48].

Despite these beneficial aspects of CT, CT cannot be done at the bedside as sonography can, and it lacks MRI's superior tissue contrast resolution [39]. In addition, CT's major drawback is that it is the leading cause of radiation exposure among all medical imaging procedures. These ionizing rays from CT can induce mutagenesis, carcinogenesis and DNA damage. CT contrast

agents can also lead to a condition known as contrast-induced nephropathy. This happens in 2-7% of individuals who receive these agents, and the risk is more considerable for those who already suffer from renal impairment [76].

C. Magnetic Resonance Angiography

With no radiation exposure, superior soft tissue contrast, and lack of need for invasive procedures, MRA is ideally suited for clinical assessment of CAS [43]. MRA has been used extensively recently to study carotid plaques. In addition to its relatively better contrast resolution, MRA's ability to visualise haemorrhagic plaques makes it a more practical tool for diagnosing such plaques than CT [48]. Strong morphological characterisation of carotid plaques in vivo, including detecting complicated plaques, which include those with surface rupture and IPH, is possible via MRI [77]. MRIs showed a sensitivity and specificity of 84% in identifying ulceration and IPH [17]. It has the highest sensitivity and specificity amid radiological modalities for detecting VPs [55].

High-Resolution MRI (HR-MRI) can differentiate symptomatic from asymptomatic plaques [17]. Therefore, imaging plaque morphology in carotid artery disease with MRI appears to be the most accurate technology currently available in clinical practice. In patients with high-grade CAS, atherosclerotic plaques exhibited LRNC with IPH when analysed with high signal intensity on MR imaging using 3D inversion-recovery-based T1-weighted sequences (MPRAGE). MPRAGE is beneficial for the evaluation of CA plaque progression [43]. Furthermore, combining specific weighted images (SII on FS T1- and FS T2-) may better diagnose high-risk soft plaques made primarily of liquid components than colour DUS [57]. Conversely, it is widely known that MRI has important drawbacks, including motion artefacts, a lengthy investigation period, inaccessibility, and high costs [55], [63].

D. Positron Emission Tomography (PET)

Positron Emission Tomography (PET) with radionuclide scintigraphy has become an extensively researched imaging modality for identifying inflammatory processes in carotid artery plaques [78]. In addition, radionuclide tracers for macrophage metabolism, macrophage

recruitment, and inflammatory markers have been designed and may one day be used to image inflammatory activity [17]. Functional molecular imaging approaches appear to correctly identify processes in VP, especially when paired with comprehensive anatomical imaging by HR-MRI or CT and employed in a multimodal environment [54], [17]. Near-Infrared Fluorescence (NIRF) utilises activatable probes that produce fluorescent images in the near-infrared light region to detect the enzymatic action of proteolytic enzymes like Matrix Metalloproteinases (MMPS) and Cathepsin Cystein Proteases (CCPS). One biological mechanism for cap erosion and subsequent plaque destabilisation is the release of proteolytic enzymes like MMPs and CCPs. Before NIRF can be used in in-vivo research on humans, however, technical advances and preclinical toxicity assessments are required [79].

Carotid PET imaging has indicated that increased fluorodeoxyglucose (FDG) uptake correlates with regions of inflammatory cells (macrophages and foam cells) and, to a lesser extent, loose extracellular matrix and neovascularization in atherosclerotic plaque. FDG uptake is higher in symptomatic patients [63]. Hybrid imaging with CT or MRI may help overcome PET's drawback of imprecise tracer localization, which hinders its utility in carotid plaque characterisation. More research is needed before these techniques are suitable for general clinical use, although hybrid PET/CT and PET/MRI are promising for carotid plaque characterisation [63]. Nevertheless, ionising radiation from these techniques directly harms the human body by energising nucleic acids in cells, and indirectly, by contact with the molecular environment, ionising radiation causes damage to cells. The end outcomes of both of these processes are the generation of reactive oxygen/nitrogen species and the damage to the DNA structure [80].

E. Angiography

Every patient who took part in ECST or NASCET had a conventional angiography done. Angiogram-related strokes have forced a change in policy. Death or stroke after 30 days following CEA was 2.3% in the Asymptomatic Carotid Atherosclerosis Study (ACAS), and 50% of peri-operative strokes were associated with angiography [47].

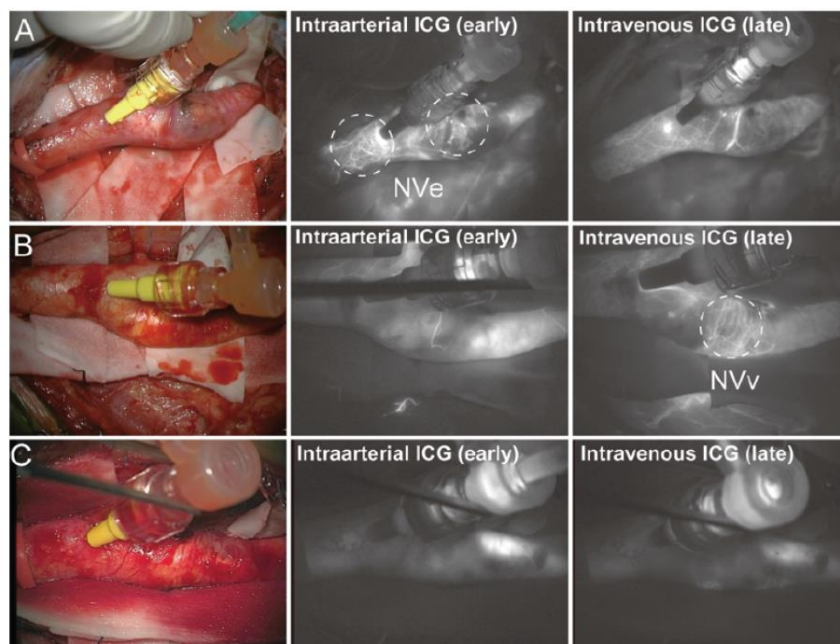


Figure 7. The ICG-based neovessel appearance is categorized into three groups.

A: Neovessels from the endothelium (NVe) were characterized by an immediate appearance and early washout of the ICG within the neovessels after intraarterial injection. B: Neovessels from the vasa vasorum (NVv) were characterized by a delayed appearance of the ICG within the vessels 10 seconds after the appearance of ICG in the carotid lumen with intravenous injection. C: Plaques showing no neovessels with both intraarterial and intravenous ICG injections were categorized as “none.” The dashed circles show neovessels [81].

Although angiography is no longer part of the CAS routine imaging protocol, new angiographic methods are proposed. In patients with CAS, neovascularization has been identified as a significant element of plaque vulnerability that may lead to the development of IPH. When the intima thickens past the diffusion limitations of oxygen and nutrients, neovascularization occurs, in which adventitial blood vessels [62] develop and extend into the intima to supply the hypoxic region. Using DUS, CT, and MRI, adventitial enhancement was initially proposed as a measure of neovascularization [82], [83]. Plaque neovascularization is assessed by comparing plaque enhancement in pre- and post-contrast pictures. While the pathophysiology and clinical relevance of plaque enhancement are still unknown, some authors have claimed that neovascularization cannot be the only element involved in plaque enhancement because certain plaques with considerable enhancement do not display neovascularization [81]. A study using Indocyanine Green (ICG) video angiography to perform a dynamic assessment of

neovascularization found that connectivity of inwardly projecting neovessels with the lumen is linked to an increased risk of symptoms and stroke after artery-to-artery embolism (Fig.7) [81].

F. Blood tests

Inflammation is a key pathogenic factor in the development and expression of atherosclerotic disease. The assessment of the patient's inflammatory and immunological profile may lead to better classifications of asymptomatic patients, as well as individuals who are susceptible to stroke recurrence. At the microscopic level, various blood inflammatory markers have been presented as risk assessment tools for patients with VPs. Among these are fibrinogen, serum amyloid A (SAA), interleukin6 (IL-6), and lipoprotein-associated phospholipase A2 (LpPLA2), which was recognized as a predictor of ischemic stroke. In multiple large epidemiological studies, high-sensitivity C-reactive protein (hsCRP) was demonstrated to predict the risk of stroke in a reproducible manner. Moreover, the presence and features of the plaque may be accurately predicted by master cytokines like IL-6 and TNF α . Matrix metalloproteinase (MMP) is a protease produced by inflammatory cells. Consequently, MMP is a traditional indicator of inflammation and a possible risk factor for plaque rupture [84], [85].

Table 2 summarizes some of the microscopic characteristics that may be used as predictors of VPs. The entire list can be found in [84], [85]. There is some evidence that the components listed in Table 2 that are associated with the mechanism of plaque progression (such as lipid metabolism and inflammation) contribute to the overall process of plaque advancement. There are substantial changes in the expression levels of these variables between stable and susceptible plaques, which may help identify VPs. In other words, their presence might not be unique to susceptible plaques, but their highly varied expression levels might make them valuable markers.

Table 2. Summary of few inflammatory biomarkers associated with plaque progression and instability

Category	Factors	Related cells	Source	Related mechanism
Inflammatory markers	CRP; hs-CRP	Macrophages	Serum; Plaques	Inflammation
	IL-6,IL-17A, IL-18,IL-21, IL-23,IL-1 β ,	-	Plaques	Inflammation
	TNF- α	T cells	Serum;	Inflammation
	IFN- γ MIP-1 β MCP-1	Macrophages Macrophages Monocytes	Plaques Plaques Plaques	Macrophage polarization - Monocyte recruitment
	YKL-40	Macrophages	Serum	Cell migration; Angiogenesis; Tissue remodelling
	SuPAR	ECs; Monocytes; T-lymphocytes;	Plaque; Plasma	-
Other factors	BIRC6	ECs; SMCs; Macrophages	Plaques	Apoptosis; Autophagy -
	Osteoprotegerin	-	Serum; Plaques	-
	Osteopontin	-	Serum	-
	Insulin	SMCs; Macrophages	Serum	Angiogenesis; Macrophage gathering
	Fibrinogen	-	Serum	Secondary haemostasis

Asymptomatic and symptomatic CAS have diametrically opposing Osteoprotegerin OPG and calcic patterns [45], [86]. Osteoid Metaplasia (OM) is a high osteoprotegerin receptor activator of NF-kB (RANK)/RANK. Ligand RANK-RANKL (OPG) triad is fundamental in bone homeostasis, and pericytes presence and enhanced circulating OPG levels are all trademarks of asymptomatic plaques. According to these contrasting patterns, circulating OPG may be a valuable plasmatic prognostic indicator for plaque vulnerability in clinical settings. However, no known imaging technique can reliably differentiate OM from other forms of vascular calcification [45], [86].

Furthermore, [87] proposed that a basic biomarker profile consisting of hsCRP, homocysteine, and total bilirubin may be used to evaluate patients with progressing atherosclerosis. If severe asymptomatic CAS is observed, an extended profile comprising inflammatory biomarkers such as TNF- α , SAA, IL-6, and IL-1 β , as well as lipid markers including LDL-c and HDL-c, ox-LDL, TRLs, Lp(a), and adipokines where available, should be explored. In conjunction with imaging characteristics, these serum biomarkers can be used to identify patients with VPs.

1.2.2. Post-op

- Histopathology

In 1995, the report from the Committee on Vascular Lesions of the Council on Arteriosclerosis (AHA) [49] recommended looking for specific components that stand out among cellular changes in advanced human lesions (Lesion Types IV, V, and VI). These components include smooth muscle cells, macrophages, lymphocytes, lipids, lipoproteins, fibrinogen in the Extracellular Matrix (EM), proteoglycans, collagen, elastin and calcium.

According to [64], [16], [41], VPs are associated with thin fibrous caps, LRNC, IPH, inflammation, and some reports of calcification. [88] examined the presence of a fibrous cap, focal calcification, necrotic core, media, surface thrombus, IPH, and intraplaque fatty deposition in carotid plaques. Necrotic granular lipid cores are typically enclosed in a tight fibrous cap around their periphery and are remarkably delicate and prone to rupture. Granular lipid cores and other liquid-phase lipid cores can escape through cracks or ruptures in the fibrous cap and enter the carotid lumen, where they can cause a life-threatening cerebrovascular embolism [57]. Therefore, unstable atherosclerotic plaques are characterised by inflammation, accumulation of an LRNC, intraplaque neovascularisation and IPH, a thin fibrous cap from extracellular matrix degradation and depletion of smooth muscle cells, and generally less calcification (Fig.8) [47], [48], [77]. There is conclusive evidence that IPH can increase the risk of cerebrovascular events by promoting plaque growth and instability [18]. It was found that the absolute volume of IPH and the lipid content of plaque were significantly related to the presence of ipsilateral cerebrovascular episodes. Regarding the risk factors for plaque rupture,

IPH is among the most serious, making its non-invasive diagnosis a crucial step toward accurate risk classification [38].

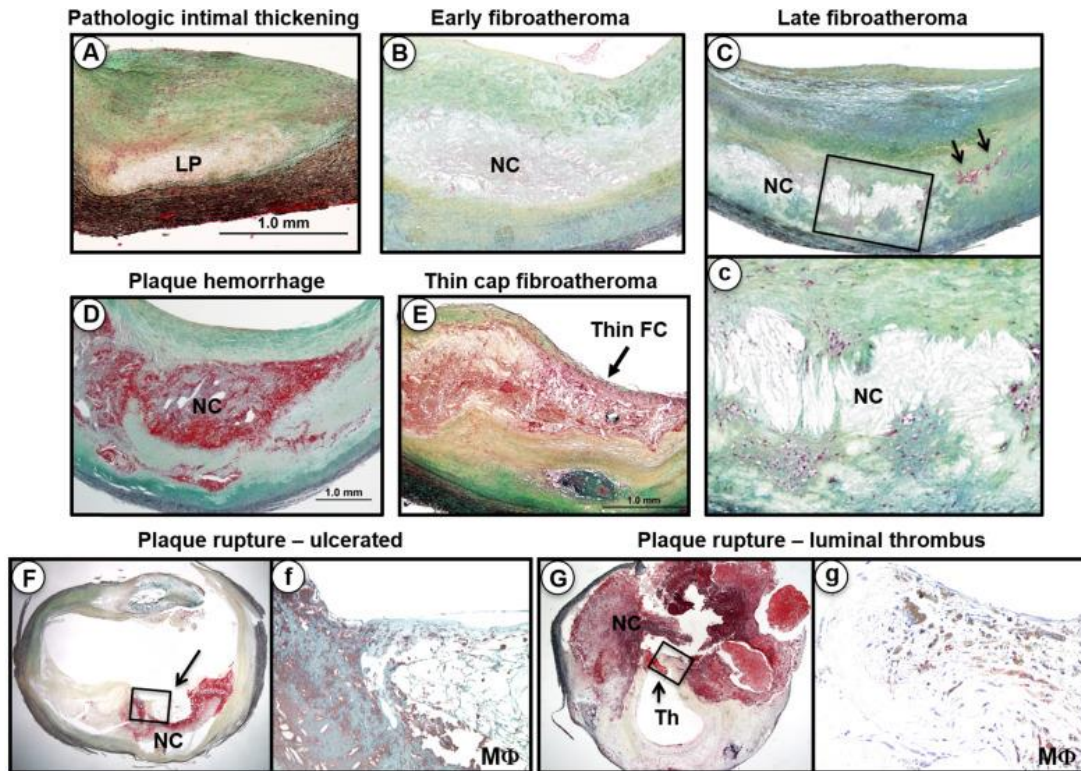


Figure 8. Carotid atherosclerotic plaque progression from pathologic intimal thickening with acellular lipid pools to plaque rupture. (A) Early lipid pool (LP) lesion. (B, C) Fibroatheromatous plaque with an early and late necrotic core (NC), respectively. The early NC in (B) shows macrophages and a proteoglycan-rich matrix (light blue-green), while the late core shows mainly cholesterol (as noted in the higher power “c”) with a few surrounding macrophages and a generalized absence of extracellular matrix. (D) IPH can lead to the rapid expansion of the necrotic core and lesion progression through erythrocyte-derived free cholesterol and secondary inflammation. (E) Vulnerable or thin-cap fibroatheroma, a precursor lesion to plaque rupture characterized by a relatively thin fibrous cap (Thin-FC). (F) “Ulcerated” and (G) “luminal thrombus” represent two different presentations of plaque rupture where invariably, the intraluminal thrombus for the latter is relatively small and absent for the ulcerated plaque. The ulcerated plaque is from a patient with symptomatic stroke; the site of ulceration (arrow) represents a portion of the plaque where the fibrous cap and necrotic core are likely embolized [42].

[89] defined plaque ulceration as a plaque surface irregularity, and the presence of a thrombus was noted. IPH was noted by looking for evidence of blood or hemosiderin within the plaque itself. The core was assessed and characterised into areas of lipid (cholesterol crystals or lipid-laden macrophage foam cells), necrotic debris, inflammation, and calcium (granular or plate-

like with or without ossification). The plaque cap was examined for intactness and whether this was a TCFA or not. Vulnerable morphologic plaque characteristics associated with a neurologic event were confirmed to include thin or fissured fibrous caps, surface irregularities, and/or ulcerations and the presence of LRNC, IPH, active inflammation, severe stenosis, or a combination of these findings. Moreover, the histologic features of plaques were established by [46], as minimum cap thickness, the prevalence of the rupture of fibrous cap and ulceration, necrotic core size, the number of inflammatory cells (including macrophages and lymphocytes), degree of IPH, and prevalence of mural thrombus. In a study by [57], the plaques were classified into two types: at-risk soft plaque, predominantly consisting of liquid components (lipid core and/or IPH with less than 70% fibrous tissue and/or calcification), and solid fibrous plaque predominantly consisting of fibrous tissue and/or calcification with less than 30% lipid core and/or IPH. In advanced atherosclerotic diseases, the secretion of vascular endothelial growth factor (VEGF) is increased along with undeveloped neoangiogenesis due to inflammation and oxidative stress. These neovessels are abnormal and defective because they lack smooth muscle cells and endothelial gap junctions, making them more likely to burst. IPH develops when one of these neovessels bursts [18].

In conclusion, histopathology is the gold standard for atherosclerotic plaque characterisation, but since it is performed after surgery, it has no practical purpose and should instead be utilized solely to ensure the accuracy of any newly developed techniques.

1.3. Synopsis of the advantages and disadvantages of each approach

Imaging techniques that are not invasive, including DUS, CTA and MRA, have the potential to differentiate morphological characteristics associated with unstable carotid lesions. Nevertheless, the majority of these imaging techniques have their drawbacks [17], [55], [63], [90], [48], which are indicated in Table 3 [63] and Table 4 [90].

Carotid atherosclerotic plaque diagnosis has moved from classic stenosis quantification to plaque characterisation. Identifying the plaque components enables a better pathophysiological understanding of the plaque and its prognosis. This facilitates patient risk stratification and endeavours the inquest of whether to operate on asymptomatic patients or not.

Table 3. Comparison of multi-modality imaging techniques for the assessment of arterial plaque [63]

Modality	Advantages	Disadvantages	Developing techniques
DUS	<ul style="list-style-type: none"> • Widely available • Non-invasive • Portable • Low cost • Identification of ulceration, IPH • 2D and 3D quantification 	<ul style="list-style-type: none"> • Operator dependent • Technical challenges: <ul style="list-style-type: none"> [1] Acoustic shadowing from calcification [2] Vessel tortuosity [3] The brain cannot be visualized 	<ul style="list-style-type: none"> • UEA • GSM analysis • 3D lumen assessment
CT	<ul style="list-style-type: none"> • Image from the aortic arch to distal cervical vessels • Identification of plaque ulceration, IPH • Identification and quantification of calcification • Quantification of plaque volume • Identification of previous cerebral infarct 	<ul style="list-style-type: none"> • Radiation exposure • Iodinated contrast exposure • Blooming artefact from calcification 	<ul style="list-style-type: none"> • 3D lumen geometry for shear stress
MRI	<ul style="list-style-type: none"> • Image from the aortic arch to distal cervical vessels • High soft tissue contrast • High resolution • High reproducibility • Identification of plaque ulceration, IPH 	<ul style="list-style-type: none"> • Low availability • High cost • Long procedure time • Multiple sequences and protocols • Not portable • Complex training • Safety requirements 	<ul style="list-style-type: none"> • 3D based techniques • Molecular MRI • 4D flow MRI
FDG PET	<ul style="list-style-type: none"> • Direct imaging of plaque inflammation 	<ul style="list-style-type: none"> • Lacks anatomic precision • Limited spatial resolution • Non-specific uptake by surrounding tissues. • Cost, lack of portability, complex training needs 	<ul style="list-style-type: none"> • Co-registration with CT and MRI • Novel molecular PET tracers

2D, two-dimensional; 3D, three-dimensional; UEA, ultrasound enhancing agent.

Table 4. Current evidence of the use of the imaging technique for the detection of features of vulnerability [90]

	DUS	PET	MRI	CT
Carotid plaque volume	±	±	++	++
Maximum wall thickness	++	-	++	+
Plaque inflammation	±	++	+	-
Neovascularization	+	±	+	+
Ulceration	+	-	++	++
LRNC	±	-	++	±
fibrous cap	±	-	++	-
Plaque calcification	±	-	+	++
IPH	±	-	++	+
Microembolism	++	-	-	-

Strong supporting evidence ++

Moderate supporting evidence +

Conflicting supporting evidence ±

Weak supporting evidence -

1.4 Conclusion

As a result, Prof. Fabien Koskas and Dr Jean-Michel Davaine (our team's vascular surgeons) addressed the need for a new non-invasive, safe technique to measure the composition of atheromatous plaques with Prof. Hamid Kokabi, Dr Frédérique Deshours and Prof. Georges Alquie (our team in the GeePs laboratory). The GeePs team then proposed employing their microwave sensor, which was in its early stages of design and fabrication, to be developed and dedicated for this purpose. The next chapter will discuss the current health applications of microwave imaging methods and how we adapted these technologies to create a better sensor and, eventually, a medical device.

Chapter II - Microwave Technology in Medicine: Emerging Applications and Advancements

Outstanding advances in imaging technology have allowed scientists and medical professionals worldwide to view the human body with greater detail and clarity. Significant breakthroughs in medical imaging technology have been made in the recent century.

Over the past few years, microwave medical applications have emerged as a distinct area of study due to the growing recognition of the pivotal role of non-invasive, non-toxic imaging techniques as a vital solution to a wide range of disorders. Microwave applications have been present in the medical field since at least the 1940s [91] when they were employed for therapeutic purposes. The use of non-ionising Electromagnetic (EM) waves at microwave frequencies for sensing and imaging in medical diagnosis began emerging around the eighties [92].

Today, Microwave Imaging (MWI) is used for much more than just straightforward organ imaging; it also provides targeted diagnostics for various diseases. Several potential uses have been explored, including examining the respiratory and cardiac cycle, imaging the brain for stroke and cerebral oedema, screening breast cancer, bone and heart imaging, and joint tissues analysis. MWI operates on the basis of the difference in electrical characteristics (relative permittivity and conductivity) of various tissues. The technology is still in its early stages of development, and further research is needed to determine its full potential and limitations. There are still unresolved questions at the experimental level, such as how to most effectively connect the microwave power to the biological tissues, the optimal frequency for high resolution, and the maximum depth to which the microwaves can penetrate [93]. However, MWI has the potential to revolutionise medical imaging and improve the accuracy, speed, and safety of medical diagnosis and treatment.

The following section starts with a look at the evolution of imaging technology from an EMs perspective and then presents comprehensive information on the cutting-edge MWI medical technologies currently in use and in development.

2.1. State-of-the-art of Radio Frequency (RF) applications in medicine

2.1.1. History

Medical imaging and diagnosis have come a long way since their inception. The earliest radiological technique dates to the 19th century when Wilhelm Roentgen discovered the X-rays and captured the first image of his wife's hand, showing its skeletal outline with a ring on one of her fingers. Several years after this discovery, during World War I, Marie Curie realised that the EM radiation of X-rays might help doctors identify bullets in troops' bodies as well as locate shattered bones. Since then, she has designed and built mobile X-ray units called "petits Curies" based on the same technique used in stationary X-ray machines, which she and her daughter Irène took to the front lines to treat wounded soldiers [94]. Since then, the medical field has shifted towards expanding the use of the entire spectrum of frequencies of EM waves.

EM waves travel through space in the form of oscillating electric and magnetic fields. These waves do not require a medium to propagate and can travel through a vacuum compared to acoustic waves, which are a form of mechanical energy that require a medium to propagate, such as air or water. EM waves include radio waves, microwaves, infrared radiation, visible light, ultraviolet radiation, X-rays, and gamma rays. The energy carried by EM waves is directly proportional to their frequency. Higher-frequency waves, such as X-rays and gamma rays, carry more energy than lower-frequency waves, such as radio waves (Fig.9).

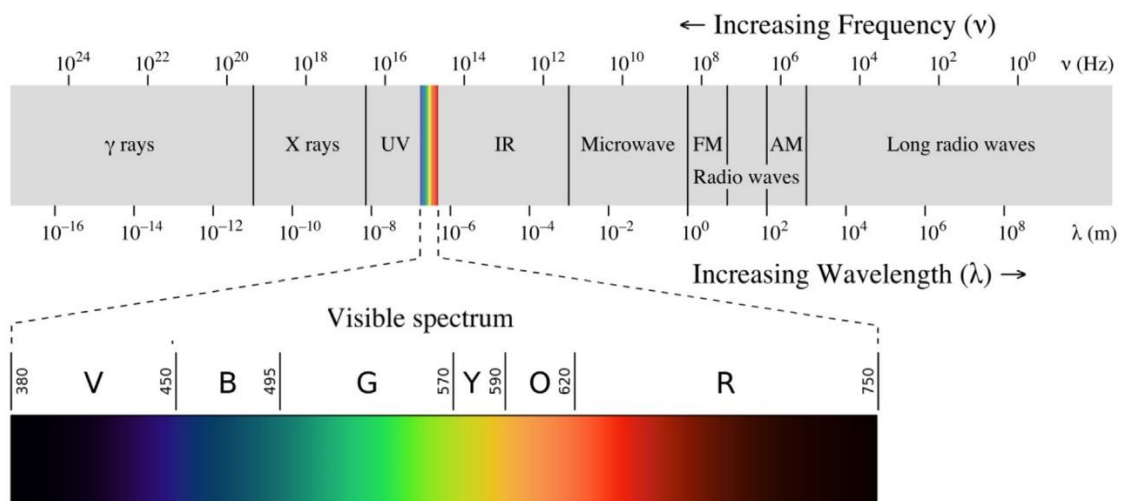


Figure 9. EM waves spectrum [95]

X-ray and CT are the primary EM imaging modalities used worldwide today. However, they utilize ionizing radiation with a frequency far higher than those used in the recently developed microwave devices for communications, which presently cover microwave and millimetre frequency bands. As mentioned in the previous chapter, EM waves with high frequencies, such as X-rays and gamma rays, can ionize atoms and molecules in living tissues, damaging DNA and other biological molecules. EM waves with lower frequencies, such as radio waves, can potentially be harmful if they are very intense or if the body is exposed to them for long periods. It is important to note that the level of harm caused by these waves depends on a number of factors, including the frequency, intensity, and duration of exposure [96].

In contrast, acoustic imaging in medical applications such as ultrasound is considered safe for the operator and the patient. However, excessive exposure to ultrasound can cause the heating of tissues, which can lead to damage or cell death. Additionally, there is some concern that exposure to high-intensity ultrasound can cause cavitation, which is the formation of tiny gas-filled bubbles in tissues, leading to tissue damage.

Conversely, in a procedure referred to as thermotherapy or hyperthermia, the heating effects of EM and acoustic waves can be employed to cure disorders. In thermotherapy, heat is used to destroy or damage cancer cells or other abnormal tissues. EM waves, such as radiofrequency or microwave energy, can be used to generate heat deep within the body, and this heat can be used to eradicate cancer cells or other abnormal tissues. This technique is called radiofrequency ablation or microwave ablation, and it is commonly used to treat tumours in the liver, kidney, and other organs. Acoustic waves, such as High-Intensity Focused Ultrasound (HIFU), can also be used to generate heat within the body to treat cancer and other diseases. HIFU uses a focused beam of ultrasound energy to generate heat at a specific location within the body [97].

Furthermore, microwaves and acoustic imaging can be combined using a technique called Thermoacoustic Imaging (TAI); this application is known as microwave-induced thermoacoustic imaging. TAI is a non-invasive imaging technique that combines the principles of thermal and acoustic imaging to produce high-resolution, three-dimensional images of biological tissues. The technique relies on the conversion of absorbed EM radiation into thermal energy, which in turn generates acoustic waves that can be detected by ultrasound transducers and used to reconstruct an image of the tissue structure (Fig.10). Microwave-induced TAI is a

unique non-invasive imaging modality that reconstructs the image to reflect the dielectric characteristics of biological tissues by receiving ultrasonic signals generated by the absorption of microwaves in various biological tissues. It has the advantages of microwave imaging's high contrast and ultrasound imaging's high resolution [98]–[100].

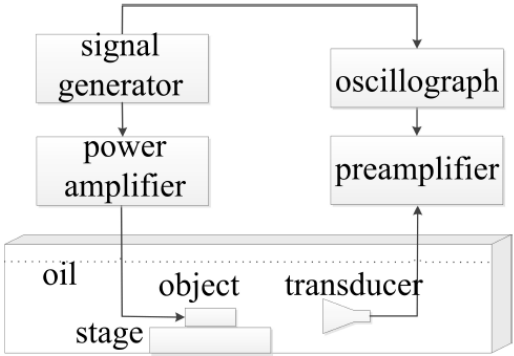


Figure 10. Schematic view of the TAI system [98].

The basic principle of TAI is based on the photoacoustic effect, which is the generation of acoustic waves due to the absorption of pulsed laser light by tissue. In TAI, a pulsed laser beam is used to generate localized heating of the tissue, resulting in a slight temperature increase that generates an acoustic wave. This acoustic wave is detected by an array of ultrasound transducer placed outside the tissue, which can be used to reconstruct an image of the tissue structure [101] (Fig.11).

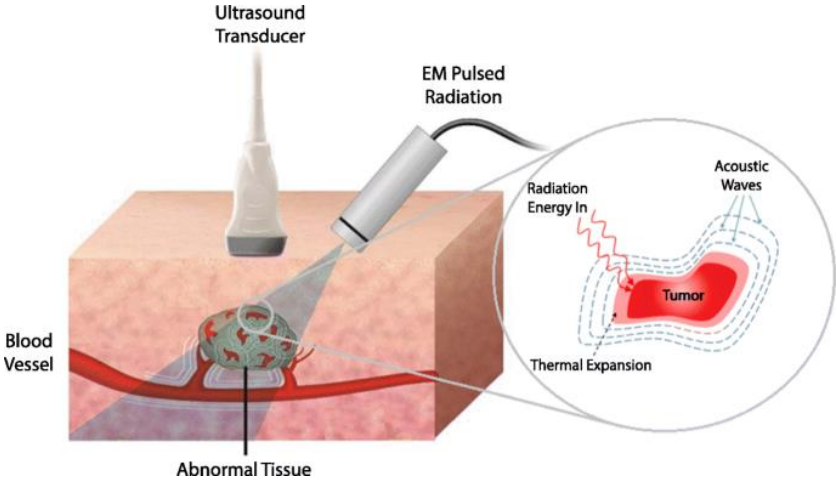


Figure 11. Breast cancer diagnosis with microwave-induced TAI [101]

The methods for determining a sample's physical properties and composition are not limited to those outlined in Chapters 1 and above. In the next paragraph, some examples are provided of diverse approaches before presenting a detailed literature review on MWI.

For example, Mass Spectrometry Imaging (MSI) is a powerful analytical technique that combines the spatial resolution of microscopy with the molecular specificity of mass spectrometry. MSI allows for the visualization and identification of molecules such as proteins, lipids, and metabolites within a tissue sample. This technique has become increasingly popular in biomedical research due to its ability to provide detailed information on the molecular composition and distribution of biological tissues. MSI uses a laser or other ionization source to vaporize molecules from the surface of a tissue sample [102].

Optical Coherence Tomography (OCT) is a non-invasive imaging technique that uses light to create high-resolution, cross-sectional images of tissues within the body. The basic principle of OCT is similar to ultrasound, but instead of using sound waves, it uses light waves to create an image. A beam of light is directed into the tissue, and the light that is reflected back is measured and analysed. The time delay between the reflected light waves is used to create an image of the tissue structure [103]. OCT can produce images with a resolution of a few microns, which is much higher than other imaging techniques like MRI or CT. This allows doctors to see detailed structures within the tissue, such as the layers of the retina.

Photoacoustic Tomography (PAT) is another non-invasive imaging technique that combines the benefits of optical and acoustic imaging to produce high-resolution, three-dimensional images of biological tissues. The basic principle is similar to TAI, which uses electromagnetic radiation in RF or microwave bands, while PAT employs visible or Near-Infrared (NIR) light, i.e. PAT is based on the photoacoustic effect [104]. When a short laser pulse is absorbed by a tissue, it generates a slight temperature rise and induces a brief but measurable acoustic pressure wave that propagates through the tissue. This pressure wave is detected by an array of ultrasound transducers placed outside the tissue, which can be used to reconstruct an image of the tissue structure [105].

Rutherford Backscattering Spectrometry (RBS) is a non-destructive analytical technique used to determine the elemental composition and depth profile of materials. It is based on the principles of elastic scattering, where incident particles collide with the nuclei of the atoms in

a material, and some of the particles are scattered backwards at high angles. In RBS, a beam of high-energy particles, typically helium ions (alpha particles), is directed at a sample. As the particles pass through the sample, some of them interact with the atoms in the material, causing them to scatter in different directions. The backscattered particles, which are reflected back towards the detector at high angles, carry information about the atomic structure of the material. By measuring the energy and angle of the backscattered particles, RBS can determine the elemental composition of the sample and the depth profile of the elements within it [106], [107]. These systems represent only a few of the various methods used to investigate the material's physicochemical properties. Nonetheless, the content of this thesis is narrowed to our area of interest, i.e. RF and microwave imaging.

2.1.2. Overview of the Microwave systems

In recent years, there has been a trend towards minimally invasive procedures, and therapies in healthcare, driven by advancements in technology and an increasing focus on patient comfort and safety. Monitoring vital parameters or the progression of certain illnesses might be examined regularly if appropriate equipment were introduced or applied and could, in particular, replace longstanding invasive approaches. Some medical diagnostic applications may benefit from suitable miniaturised MWI devices fabricated at the Industrial, Scientific, and Medical (ISM) radio frequency band. These instruments would allow researchers to determine the dielectric properties of biological tissues, representing their proper composition in terms of cells and organic materials.

The ISM radio frequency band is a range of radio frequencies set aside by international agreements for the exclusive use of RF energy for industrial, scientific, and medical devices without requiring individual licenses. The ISM band is used for a variety of applications, including medical equipment, scientific instruments, industrial equipment, and household appliances such as microwave ovens. The ISM band is divided into several frequency ranges [108]. The European Telecommunications Standards Institute (ETSI) regulates the ISM band in Europe, and medical device frequencies generally range around 13.56 MHz, 433 MHz, 868 MHz, 2.4 GHz, and a few other frequencies. These frequencies are reserved for medical

purposes because they provide low-power and interference-free transmission possibilities. The range, reliability, and accessibility of the ISM band have made it an essential tool for many industries, including healthcare, telecommunications, and consumer electronics.

Almost 50 years have gone into developing MWI methods to be used in the medical field [109], [110]. Recently, they have attracted particular attention for therapeutic and diagnostic purposes [111], [112]. This attention is attributed to several reasons, and one of the main ones is the potentially low cost of these techniques [110], [113]–[116]. In developing as well as emerging countries, acquiring accessible, low-cost tools for medical diagnosis is a priority at the moment [109]. In addition, another significant strength of MWI for health purposes is the benefit of being non-ionising, i.e. risk-free for the patient and the operator producing no adverse effects as they are operated within the ISM band. Furthermore, they are typically non-invasive and portable [109], [113]–[117], [118]. Therefore, research is ongoing into merging MWI diagnostic and therapeutic techniques with existing imaging modalities, as they have the potential to be helpful imaging tools for a variety of medical applications. Hence, innovative MWI medical devices are being developed ceaselessly in laboratories worldwide [110], [113], [115].

The use of EM energy in the microwave frequency band is particularly interesting due to the fact that it satisfies the competing needs for resolution and penetration depth [119].

MWI systems typically consist of a source of radiation to "illuminate" the target and a receiver to gather the field scattered by the target. As microwaves can travel through dielectric materials, the scattered field data can reveal the structure of the tested body from the inside out [112]. Various techniques can be used to either map the spatial distribution of the dielectric properties of the observed item (tomography) or to detect and pinpoint any aberrant tissue within the imaged object (radar-based imaging) [120].

MWI can be conducted with a single sensor or several sensors, depending on the imaging system and application. In an MWI with a single sensor, a single antenna or sensor is utilized to send and receive microwave signals following a reflection or scattering by tissues. In such a setting, neither 2D nor 3D images are created. Single-sensor systems are straightforward and inexpensive, but their sensitivity may be inferior to multi-sensor systems. Examples include the detection of a heartbeat or changes in the microwave signal generated by cerebral oedema.

Several antennas or sensors are utilized in a multi-sensor MWI system to broadcast and receive microwave signals. The antennas are positioned around the item being scanned, and the reflected signals are merged to provide and treat a 2D or 3D map or image with a high resolution [93]. Multi-sensor systems can give higher imaging resolution and sensitivity than single-sensor systems, but they may be more complex and often expensive to implement. In addition, there are hybrid MWI systems that combine single-sensor and multiple-sensor approaches. For instance, a single sensor may provide an initial image, which would then be modified and enhanced using data from several sensors [95]. MWI system's hardware typically consists of a microwave signal transmitter and a receiver like a Vector Network Analyzer (VNA), an antenna array, and an RF switch that can shift between multiple antennas [93].

MWI has potential applications in diagnosing, monitoring, and treating various diseases. The following paragraph provides examples of current developments in each field.

- *Diagnosis:*

Via the measurement of the electrical properties of tissues, it is possible to detect diseases such as cancer or inflammation or create 2D or 3D images of electrical impedance distribution in a body. In recent years, breast cancer screening using MWI has been one of the most prevalent themes studied in this field.

This implementation has advanced to the stage of preliminary clinical testing, with promising findings thus far [109], [113], [121]. Both tomographic and radar techniques have been employed in imaging breast cancer (Fig.12). The difference in dielectric properties is the basis for the observed contrast [122]. The predominant adipose tissue has significantly lower dielectric characteristics than the high water content tumours. Tumours as small as 1 cm in diameter can be consistently detected using tomographic techniques [123]. Recently developed methods for tracking the efficacy of chemotherapy for breast cancer include measuring the changes in the dielectric properties in the tumour before it shrinks. Differences in the dielectric properties before and after shrinkage were documented, implying that these MWI devices are sensitive enough to measure physiological changes caused by treatment [123].

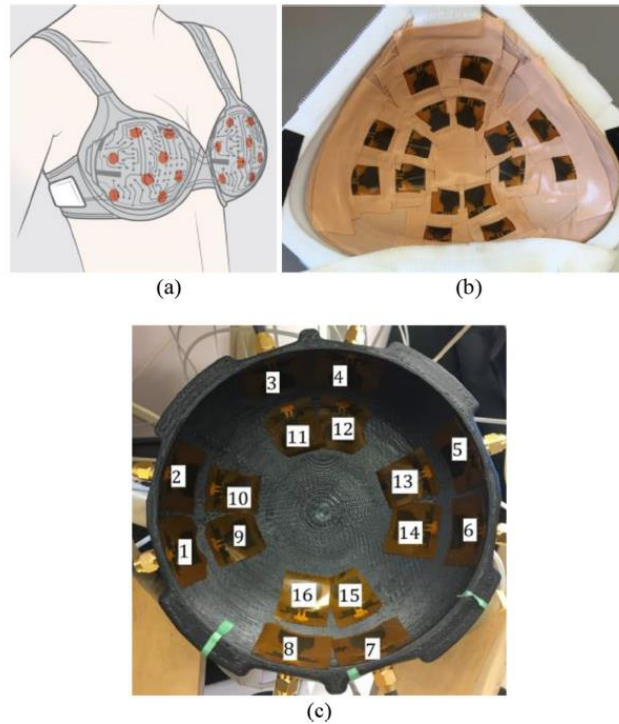


Figure 12. (a) Envisioned wearable bra microwave radar. (b) Antenna arrangement in prosthetic bra for volunteer testing. (c) Current antenna arrangement in the 3D-printed hemisphere for phantom testing [109].

In the end, the clinical effectiveness of such approaches will depend not only on the magnitude of malignant-to-normal and malignant-to-benign dielectric contrasts but also on the diversity of normal tissue properties within and across individuals [119].

Like breast cancer or recognising the presence of oedema in the recovery process after surgery, several MWI techniques have lately translated into a practical clinical application [123].

Additionally, some researchers have found a new way to diagnose Alzheimer's disease by comparing the dielectric characteristics of a healthy brain with a brain sample from a patient with severe Alzheimer's disease [124]. Another remarkable illustration of MWI is the recently invented microwave scanner, which uses MWI to detect and distinguish ischemic strokes from intracranial bleeding strokes [125]. [126] conducted the first clinical trial to investigate MWI's ability to detect traumatic intracranial lesions - chronic subdural haematomas. All haematomas were found at a 25% false positive rate [126]. Further, a prototype microwave helmet to diagnose stroke was developed with the goal of identifying patients with haemorrhagic stroke as opposed to patients with blood clots (Fig.13) [127], [128]. The patient wears a helmet with

ten antennas inside it while being examined. Diagnosing a stroke with a microwave system requires taking readings and analysing signals travelling through the brain. Distributing the antennas across the scalp improves detection sensitivity [109].

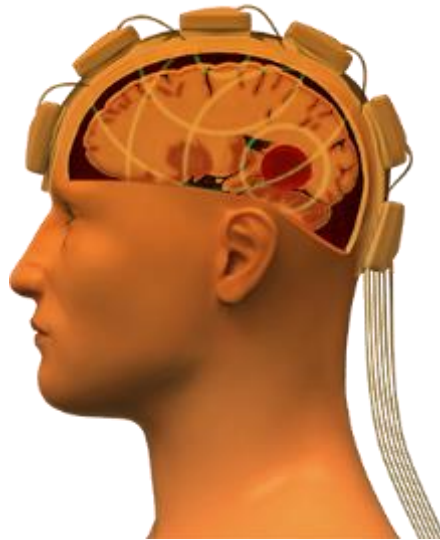


Figure 13. Microwave helmet to diagnose stroke.

The first clinical trials utilizing MWI were undertaken in dermatology, particularly dermatology, for melanoma detection, as the skin is the most common and convenient biological tissue to investigate with microwaves, according to [129].

In the cardiac field, a technique by [113] has been demonstrated to detect as little as 4 mL of water in the lungs, corresponding to the beginning stages of Coronary Heart Failure (CHF). Due to its detection sensitivity, low cost, mobility, and rapid detection time, the current system has the potential to be an effective diagnostic tool, particularly in emergency units, general practitioner clinics, and rural locations [113].

Furthermore, damage to surrounding soft tissues caused by a bone fracture can be imaged by an MWI. X-rays are unable to identify soft tissue injuries. This method may have a better chance of success in the clinic if it is used for monitoring and healing of a lesion [93].

Myocardial infarction is one of the pathological disorders that could potentially be detected with MWI of the heart since the electrical characteristics of myocardial tissue are highly dependent on coronary blood flow. Moreover, because of the millisecond temporal resolution, it can be used to capture images of a beating heart in real time, which can then be analysed to

extract individual heartbeats. The field of cardiac MWI, however, is still in its early stages and fraught with limitations [93].

Prior research using microwaves on carotid plaques primarily involved microwave radiometry. The principle is to detect temperature changes in the arterial wall accurately. These techniques indirectly measure inflamed carotid plaques [130], not to be confused with research that uses infrared (IR) thermography to detect skin temperature as a CAS indicator [131].

Current studies focus primarily on brain imaging and breast cancer [114], [124], [132], [133]. Nevertheless, novel approaches are developed every day, like the correlation between permittivity changes and the severity and depth of skin burn [134], the use of sweat ducts in the skin as low-quality coefficient antennas [135], muscle atrophy diagnosis [136], [137]. In-vivo evaluation of hip fracture healing [138], examining intracranial pressure [139], measuring fluid volume changes in the heart [140], and measuring limb haemodynamic [141] have been accomplished by employing microwave sensors in addition to different technologies proposed beyond this.

- *Monitoring:*

[123] have suggested that since bone physiology alters significantly with age and disease, it stands to reason that dielectric property monitoring would find beneficial uses in bone imaging [123]. Bone's organic matrix, water, and lipids are all predicted to impact the bone's dielectric properties and mineralisation [142]. Recently, the dielectric characteristics of calcaneus bone have been measured using MWI. It has been suggested that osteoporosis can be tracked by measuring the bones' dielectric characteristics. In a study by [142], dielectric properties of bones were evaluated using the open-ended coaxial probe method. These first results demonstrated a statistically significant distinction in the dielectric characteristics of osteoporotic and osteoarthritic bone samples. These results lay the groundwork for creating a bone imaging device based on microwave frequencies to diagnose and follow osteoporosis [114], [142].

Another demanding medical issue that has attracted much attention in the MWI field is how to accurately measure glucose levels in diabetics' blood [143], [144], [145]. As an alternative to test strips used today that need a drop of blood each time, impedance spectroscopy can be utilised because it provides a contactless non-invasive method of gauging the blood's electrical

properties. It is well established that variations in the electrical characteristics of erythrocyte membranes caused by fluctuations in blood glucose levels lead to an electrolyte imbalance in the skin and subcutaneous tissue (Fig.14) [146], [147]. However, in spite of the fact that teams of researchers from all over the world are working tirelessly to develop this microwave glucose sensor, no validated, certified sensor has yet been made available to the public.

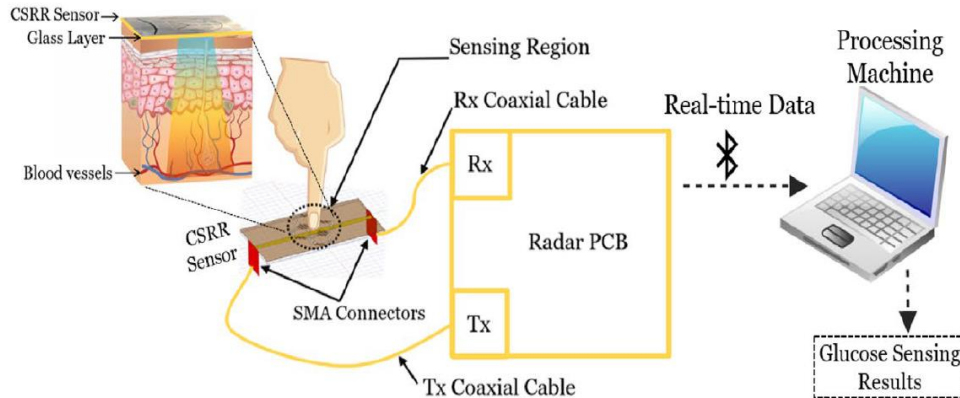


Figure 14. Illustration of the portable radar-driven sensor for measuring the glucose level non-invasively from the fingertip [146].

Today, microwave medical devices can monitor vital signs [148]. Monitoring heart rate is an example of a common (and popular) wearable biotelemetry technology. Monitoring a patient's heart rate regularly has been shown to lower the chance of a cardiac accident and allow for prompt medical attention to be given to those suffering from cardiovascular disorders [149]. In addition to these cutting-edge methods, numerous systems using miniature sensors to monitor the body's heart rate, temperature, pH, pressure, blood flow, and respiration rates have been created for wear or implantation. They can be worn or implanted thanks to their malleability, pliability, and biocompatibility [148].

Additionally, monitoring the state of a thermal trauma wound via MWI is being thoroughly researched [129]. [150], [151] developed a chip based on microwave sensor technology to monitor arterial plaque development in real time. The catheter's sensor is composed of an oscillator operating at 27 GHz, coupled to a short microstrip line section. The sensor makes it possible to accurately distinguish between "hard" and "soft" plaques. However, increased detection frequencies lead to additional power release and tissue heating. There is no way yet to

differentiate between fibrous, fibro-fatty, and dense calcium areas. Furthermore, the absorption coefficient and permittivity of blood are as well critical issues in addition to the influence of blood turbulence which is still vague. These problems have yet to be solved before this sensor can be used on patients.

Currently, to my knowledge, none of the mentioned above MWI systems for diagnoses and monitoring has been officially clinically used despite encouraging preliminary results and evidence of the link between dielectric properties and physiological changes.

- *Therapy:*

MWI could also find a niche in reconstructive plastic surgery and the treatment of burn scars at various stages of development [129]. Other areas of study include the use of microwave heating to boost the efficacy of gene therapies and the development of heat-sensitive micro-carriers of pharmaceuticals or radiation [liposomes] that can be activated to release their content in malignant tumours [110]. Microwave hyperthermia treats breast cancer, and microwave ablation treats liver, lung, kidney, and adrenal tumours [142]. Tumours are heated at 40-44 °C using microwave EM radiation [125]. Hyperthermia can be produced noninvasively by microwaves in many significant cancer sites, including cutaneous and subcutaneous sites and locations accessible through natural apertures in the body. As they stand now, hyperthermia devices are excellent for treating small, superficial tumours with optimal thermal doses, but they are not a good fit for treating large cutaneous or subcutaneous lesions [110]. Diathermy is the use of high-frequency electrical currents to cut or destroy tissue. The microwave heating field is vast; however, further exploration of this topic is outside the scope of this thesis.

Figure 15 highlights the most widely researched concepts for medical MWI systems. MWI depend on the material's dielectric characteristics being well specified in the microwave frequency range. Consequently, accurate dielectric characterisation of biological tissues in the microwave, or more precisely in the gigahertz (GHz) frequency range, would be extremely useful for medical applications [125]. As cited previously, the reflection and transmission of EM waves in biological tissues are mainly determined by the tissue's dielectric characteristics, specifically their relative permittivity and conductivity [142].

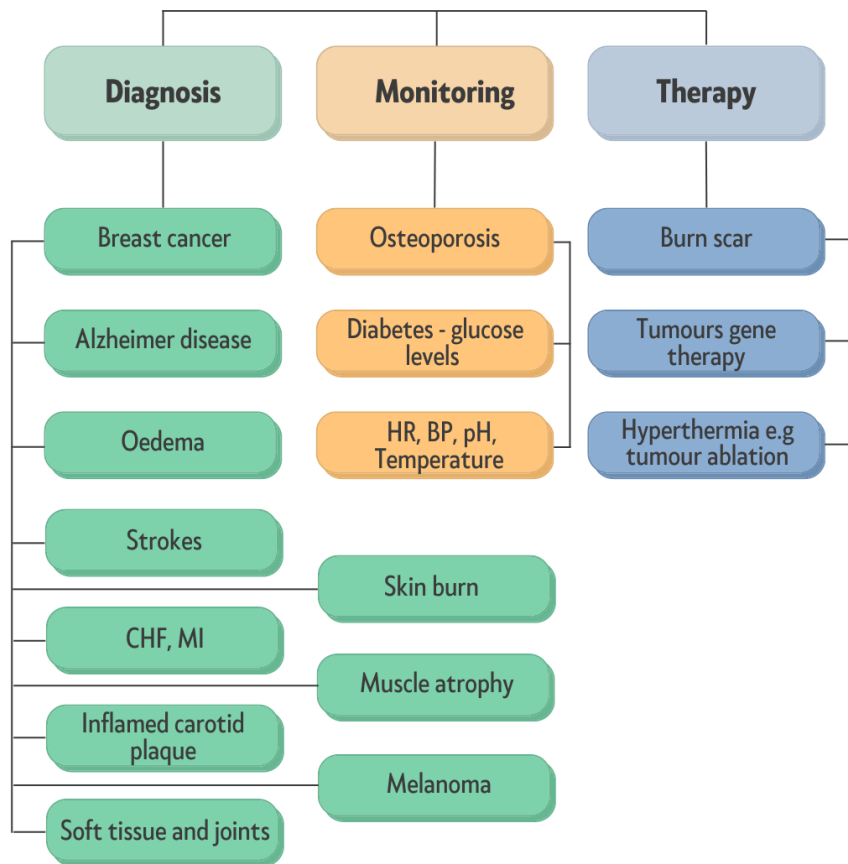


Figure 15. A summary of some of the microwave approaches being developed for medical applications.

Relative permittivity is a complex variable that characterises dielectric polarisation (i.e. a material's ability to store electric energy) and losses in a material exposed to an electric or electromagnetic field [125]. Any MWI system's end goal is to replace more expensive sensing and imaging modalities in a clinical context at a lower cost to the patient. This goal can only be attained by pushing the MWI system from the realm of theory and simulation into the context of practical, clinically relevant prototypes. Despite this, there are several technical issues and unanswered questions that must be resolved before clinical trials can begin, which shape the future of MWI research. A few of them are covered here.

2.2. Biological tissues dielectric model

2.2.1. Debye model and Cole-Cole equation

When an electric field \mathbf{E} is applied to matter, the constituents (molecules, ions...) are polarised, thus giving what is called the polarisation \mathbf{P} ; the measure of the polarisation \mathbf{P} of the material is related to the electric field and given in a first linear approach by

$$\mathbf{P} = \varepsilon_0 \chi \mathbf{E} \quad (1)$$

where χ is defined as the electric susceptibility.

The electric displacement field \mathbf{D} inside the medium resulting from the applied electric field \mathbf{E} is then:

$$\mathbf{D} = \varepsilon_0 (\mathbf{E} + \mathbf{P}) = \varepsilon_0 (1 + \chi) \mathbf{E} = \varepsilon \mathbf{E} = \varepsilon_0 \varepsilon_r \mathbf{E} \quad (2)$$

Where ε_0 is the vacuum permittivity, ε the dielectric permittivity, and $\varepsilon_r (= \varepsilon/\varepsilon_0)$ is the relative dielectric permittivity of the medium.

Generally, in EM, microwave radiation propagates inside a dielectric material following Maxwell's equations. The wavelengths of the radiation in the frequency range 1-100 GHz vary from 30 cm to 3 mm, which are substantially larger than the size of atomic or molecule structures. On the other hand, the wavelengths are comparable to the size of numerous objects, such as biological entities. Furthermore, the quantum energies at these frequencies are so weak (4×10^{-4} eV at 100 GHz) that they cannot modify intermolecular interactions. Fundamentally, EM radiation with frequencies in the microwave range (up to 100 GHz) has very weak quantum energies, and as a result, they do not have enough energy to modify intermolecular interactions. This is because the energy of the radiation is proportional to its frequency, and at these frequencies, the energy is not high enough to cause changes in the chemical bonds between molecules.

However, it is worth noting that while the quantum energies at these frequencies may not be strong enough to modify intermolecular interactions, they can still penetrate biological tissues and interact with the electrical properties of the tissue, such as the dielectric constant and conductivity. This information can be used to perform medical diagnostic tests, such as MWI and impedance spectroscopy. As a result, microwave radiation is a non-invasive and safe

technique for the human body because it does not modify the biological composition on any scale and does not require an incision or injection for the patient [136].

During the propagation inside the dielectric material, the oscillating electric field of the EM wave interacts with the electric dipoles. As in analogy with the static case, the behaviour of the material under the EM excitation can be described by a complex relative permittivity ϵ_r :

$$\epsilon_r = \epsilon_r' - j \epsilon_r'' \quad (3)$$

in the case of linear, homogeneous, and isotropic materials.

The real part of this quantity corresponds to the electrical energy stored inside the material, and the imaginary part to the energy dissipated inside due to dipole relaxation mechanisms and eventually to conduction phenomena. It is also usual to compare real and imaginary parts by introducing the quantity $\tan \delta$ as:

$$\tan \delta = \epsilon_r'' / \epsilon_r' \quad (4)$$

where δ is called the loss angle.

Thus, the relative dielectric constant can be written as:

$$\epsilon_r = \epsilon_r' (1 - j \tan \delta) \quad (5)$$

The real part ϵ_r' , related to the component of the displacement electric field \mathbf{D} in phase with the electric field, is correlated to the electric energy stored in the material, and the imaginary part ϵ_r'' , in quadrature with the E-field, corresponds to the dissipated energy or losses in the material. Many studies have been proposed to describe the frequency behaviour of several materials. Biological tissues like liquids can be described by the Debye model or Cole-Cole equation, the latter being often preferred in many cases because it represents very well the relaxation mechanisms occurring in polar dielectrics.

Following the Debye model, the dipole orientation in an electric field can be compared to a first-order mechanical system giving rise to a relaxation mechanism characterised by a time constant τ . Excited by a harmonic electric field:

$$\mathbf{E}(t) = \mathbf{E}_0 e^{j\omega t} \quad (6)$$

This relaxation model leads to defining the complex dielectric permittivity at the frequency f , (with $\omega=2\pi f$):

$$\varepsilon_r(\omega) = \varepsilon_\infty + \frac{\varepsilon_s - \varepsilon_\infty}{1 + j\omega\tau} \quad (7)$$

Which was derived in its simplest form by the Debye model for polar dielectrics. In this equation, $\varepsilon_r(\omega)$ is the complex dielectric permittivity, ε_s and ε_∞ are the "static" and "high frequency" dielectric permittivity's, the last one being the value of the permittivity measured for $\omega\tau > 1$. By calculating the real and imaginary parts of the complex permittivity, we obtain:

$$\varepsilon_r' = \varepsilon_\infty + \frac{\varepsilon_s - \varepsilon_\infty}{1 + \omega^2\tau^2} \quad (8)$$

And

$$\varepsilon_r'' = \frac{\varepsilon_s - \varepsilon_\infty}{1 + \omega^2\tau^2} \quad (9)$$

i) Several adjustments must be involved in order to overcome simplified assumptions of the Debye model: If all the dipoles existing in the material have different relaxation times τ_n , the resulting complex permittivity can be expressed as the sum of the individual contribution of a kind of dipoles and then

$$\varepsilon_r(\omega) = \varepsilon_\infty + \sum_n \frac{\varepsilon_n}{1 + j\omega\tau_n} \quad (10)$$

with the condition

$$\varepsilon_s = \varepsilon_\infty + \sum_n \varepsilon_n \quad (11)$$

ii) If the material presents some conductivity σ , it contributes to the electrical losses. The total current density results from the conduction current density $\mathbf{J}_c = \sigma \mathbf{E}$, and the displacement current density $\mathbf{J}_D = \frac{\partial \mathbf{D}}{\partial t} = j\omega\varepsilon_0 \varepsilon_r \mathbf{E}$, so that it defines the total relative permittivity as:

$$\varepsilon_{tot}(\omega) = \varepsilon_r(\omega) - j \frac{\sigma}{\omega\varepsilon_0} = \varepsilon_r'(\omega) - j \left[\varepsilon_r''(\omega) + \frac{\sigma}{\omega\varepsilon_0} \right] \quad (12)$$

If the conductivity σ is independent of the frequency, the conductivity losses increase towards low frequencies.

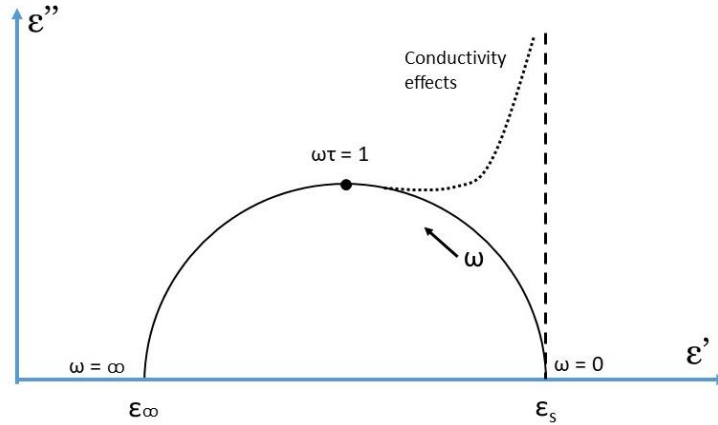


Figure 16. Cole-Cole diagram of a material with conductivity

iii) In some cases, it is necessary to introduce another parameter β to consider the fact that the measured diagram is flattened. A general relation proposed by Cole replaces in the denominator of ϵ_r the term $(j\omega\tau)$ by $(j\omega\tau)^{1-\beta}$. When $\beta = 0$, the equation of ϵ_r corresponds to the Debye model (Fig.16).

In the field of dielectric spectroscopy, the Cole-Cole equation is extensively used to characterise materials and biological tissues, taking into consideration the effects of dispersion and relaxation processes in the material. Often in materials where the main contribution to the losses is related to conductivity phenomena (ionic, for example), the imaginary part of the permittivity is expressed as an equivalent conductivity σ_c defined as:

$$\epsilon'' = \frac{\sigma_c}{\omega \epsilon_0} \quad (13)$$

And

$$tg \delta = \frac{\sigma_c}{\omega \epsilon_0 \epsilon'} \quad (14)$$

2.2.2. Microwave interaction with heterogeneous biological tissues

Several dielectric mechanisms or polarization effects may contribute to the permittivity of a material. A dielectric substance has a charge carrier configuration that an electric field can

move. To compensate for the electric field, the positive and negative charges become polarized and move in opposite directions [152]. Tissue dielectric characteristics are primarily the result of three relaxation processes: Dipolar Orientation, Interfacial Polarization, and Ionic Diffusion (Fig.17).

- 1) Interfacial Relaxation: If a material is electrically heterogeneous, charges develop at the material's interfaces due to boundary circumstances. Colloids and emulsions often have dielectric properties that are dominated by interfacial effects.
- 2) Dipolar Orientation: Water is the predominant component in most tissues, and in numerous ways, the dielectric properties of tissues mirror those of water. At RF, the conductivity of tissue is comparable to that of its intracellular and extracellular fluids. The dielectric dispersion at microwave frequencies results from the dipolar relaxation of the bulk tissue water. At microwave frequencies, dipolar relaxation of water is the primary action in tissues.
- 3) Ionic Diffusion: Counterion phenomena result from ionic diffusion in the electrical double layers close to charged surfaces. Counterion polarization effects have been seen in numerous systems with charged surfaces, including emulsions, spheres, microorganisms, and long-chain macromolecular polyions, such as DNA [153].

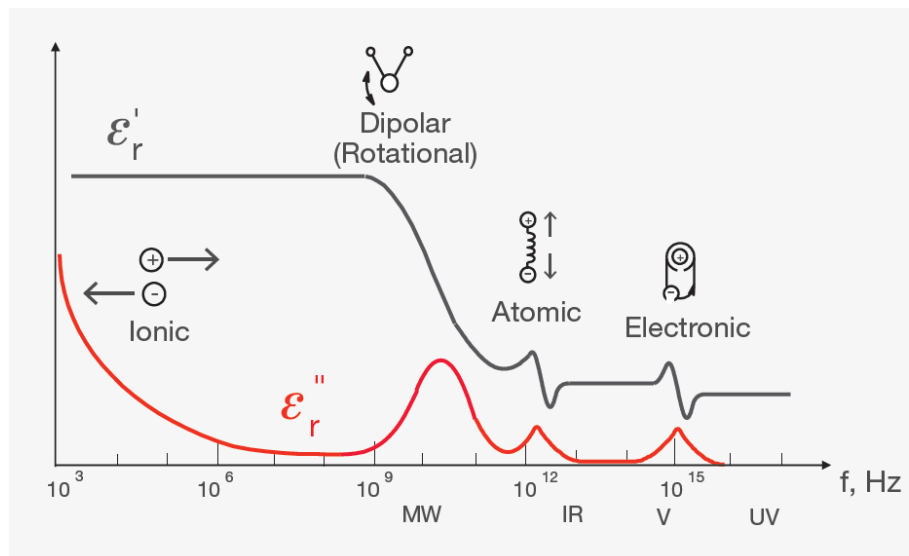


Figure 17. The frequency range of dielectric mechanisms contributing to dielectric permittivity [152].

The human body is very heterogeneous, and propagating microwaves through inhomogeneous media inevitably results in scattering, necessitating the development of computationally demanding methods to account for this phenomenon. Only in the past several years has the necessary computer capacity become widely available, allowing for the production of results with clinical relevance. [109].

The EM field distribution is complex because of the heterogeneous nature of biological tissues; for example, the dielectric properties of each tissue and the existence of various interfaces (air/tissue and tissue/tissue) all play a role. Furthermore, the relative permittivity, conductivity, and frequency used on different tissues impact the amount of EM wave energy reflected and transmitted via surfaces between these tissues [148].

These propagation effects inside the heterogeneous biological tissues are complicated because the tissues are malleable, and the interfaces are relatively ill-defined. For example, the skin consists of the epidermis and the dermis, the last one making the transition with a fatty layer including blood vessels. Moreover, many tissues irrigated by water or blood present high losses; these losses contribute to more or less strong attenuation of the EM wave inside these layers, mainly at high frequencies.

Therefore, a suitable frequency range for investigating biological tissues corresponds to a microwave band extending from 1 GHz to 8 - 10 GHz. This thesis chose the ISM band around 2.4 GHz, where the losses are relatively moderated.

2.2.3. Permittivity profile and dielectric properties of biological tissues from current databases

Since the pioneering work of Schwan and Foster four decades ago, dielectric spectroscopy of living tissue has been a vibrant area of study due to its wide range of potential applications [122], [154]. Numerous studies have described dielectric characteristics of diverse animal and human tissue across a broad frequency range of 10 Hz – 100 GHz. In 1996, *Gabriel et al.* conducted one of the most exhaustive analyses to date, reporting the dielectric properties of a wide variety of biological tissues across a wide frequency range (from 10 Hz to 20 GHz), including freshly excised bovine and porcine tissues and human autopsy materials [154].

High permittivity is characteristic of tissues rich in polar molecules, especially water, while low permittivity is typical of tissues rich in nonpolar elements, such as adipose tissue. These features can be highly informative when diagnosing pathologies [122]. Tissue characteristics must be understood first for diagnostic imaging to establish if a contrast exists between the background tissue and the tissue of interest [155].

MWI uses the natural dielectric difference between healthy and abnormal tissues at the anatomical site of interest. While there are challenges associated with low-frequency devices, there is still plenty of room for innovation and development in this area. With continued research and development, we can overcome these challenges and create safe, effective, and innovative low-frequency devices for various applications.

Table 5. The permittivity and conductivity of several biological tissues at 2.2 GHz *Blue* [156], *yellow* [157]

Tissue	Permittivity		Elec. Cond.(S/m)		Loss tangent	Penetration depth (mm)
Blood	58.7	58.7	2.34	2.34	0.32	17.60
Blood Vessel	-	42.83	-	1.28	0.24	27.20
Bone (Cancellous)	18.8	18.8	0.72	0.71	0.31	32.44
Fat (Not Infiltrated)	5.31	5.3	0.09	0.09	0.14	130.55
Muscle	53	53	1.58	1.57	0.24	24.72
Skin (dry)	38.3	38.3	1.35	1.35	0.28	24.57
Skin (wet)	43.2	43.2	1.45	1.44	0.27	24.40
SAT (Subcutaneous Fat)	10.9	-	0.23	-	-	-

The IT'IS Foundation database [156] and the Italian National Research Council database [157] are two examples of extensive online databases containing information on biological tissues' dielectric characteristics (Table 5). The parametric models created by *Gabriel et al.* [12] form the basis for both databases. There have been improvements in measurement procedures since the oeuvre of *Gabriel et al.*, but their findings are still used as the gold standard for dielectric characteristics of human tissues [158]. Table 5 covers the dielectric constant, the electrical conductivity and the loss tangent of a few biological tissues used as a reference in this research,

all at our chosen frequency of 2.2 GHz. The last column gives calculated penetration depth values, representing the damping of a plane wave propagating inside a homogeneous medium with the given complex dielectric permittivity. From Maxwell equations, the attenuation of the plane wave, which propagates from the surface inside the medium in the direction $r > 0$, is given by the exponential term $\exp(-\alpha r)$, where α is the attenuation constant. The penetration depth is defined as

$$\delta = \frac{1}{\alpha} = \frac{1}{\omega} \sqrt{\frac{2}{\varepsilon_0 \varepsilon' \mu}} \left\{ \sqrt{\left[1 + \left(\frac{\varepsilon''}{\varepsilon'} \right)^2 \right]} - 1 \right\}^{-1/2} \quad (15)$$

with $\varepsilon'' = \sigma / \omega \varepsilon_0$

This length, expressed in meters (mm in Table 5), is a mean to compare the tissues from the microwave absorption point of view at a given frequency. As shown in Table 5, muscle and skin (dry or wet) have approximately the same value of the penetration depth, although they have different permittivity values.

As formerly indicated, [159] transcribed dielectric data that is widely used in EM modelling and assessment of Specific Absorption Rate (SAR). This is generally consistent with data reported in other studies [119], [160]–[165]. Researchers believe that data from animal studies can be generalised and used for human tissue modelling [154]. This was derived from studying the differences in the dielectric properties of skeletal muscle, brain cortex, spleen, and liver tissue of different species between 0.1 and 10 GHz [166]. It was reported that there was a relatively minimal variation between the identical tissues of different species (within the system's uncertainty). Subsequently, many different types of malignant tissue have had their dielectric characteristics defined, joining those of healthy biological tissue [119], [154], [167]–[171]. As a result, most current research [154], [155], [172] has concentrated on characterising the error caused by dielectric measurements and the features of tissues that affect the dielectric. Experimental data on the permittivity of tissues can be fitted using a Cole-Cole model whose parameters are adjusted to the behaviour throughout a broad frequency range (the frequency range stated here is between 1 and 10 GHz). The curve in Figure 18 [173] shows that in the range of 1-10 GHz, the permittivity is relatively constant, and the conductivity is reasonably

moderate. Therefore, this validates the choice of this frequency range for experimentation on in-vivo biological tissue.

Moreover, fat and bone marrow contain an insignificant amount of water, so they have the lowest relative permittivity ≈ 5 . However, between 1 and 10 GHz, there is a slight discernible variation in fat and bone marrow permittivity's. The relative permittivity of the cortical and cancellous bones is 12 and 18, respectively, at a frequency of 2.45 GHz. In contrast, blood and muscle have a greater relative permittivity at roughly 52 and 58 because of their high-water content. Therefore, there is a substantial shift between 1 and 10 GHz [173] in the frequency dependence of the relative permittivity of highly hydrated tissues. Typically, fat or protein (both of which have low permittivity and low loss) and water (which have high permittivity with higher loss) are thought to be the primary determinants of the dielectric behaviour of soft tissues at microwave frequencies. At these frequencies, pure lipids and proteins have relative permittivity's little over two and loss factors of 0.1 [174].

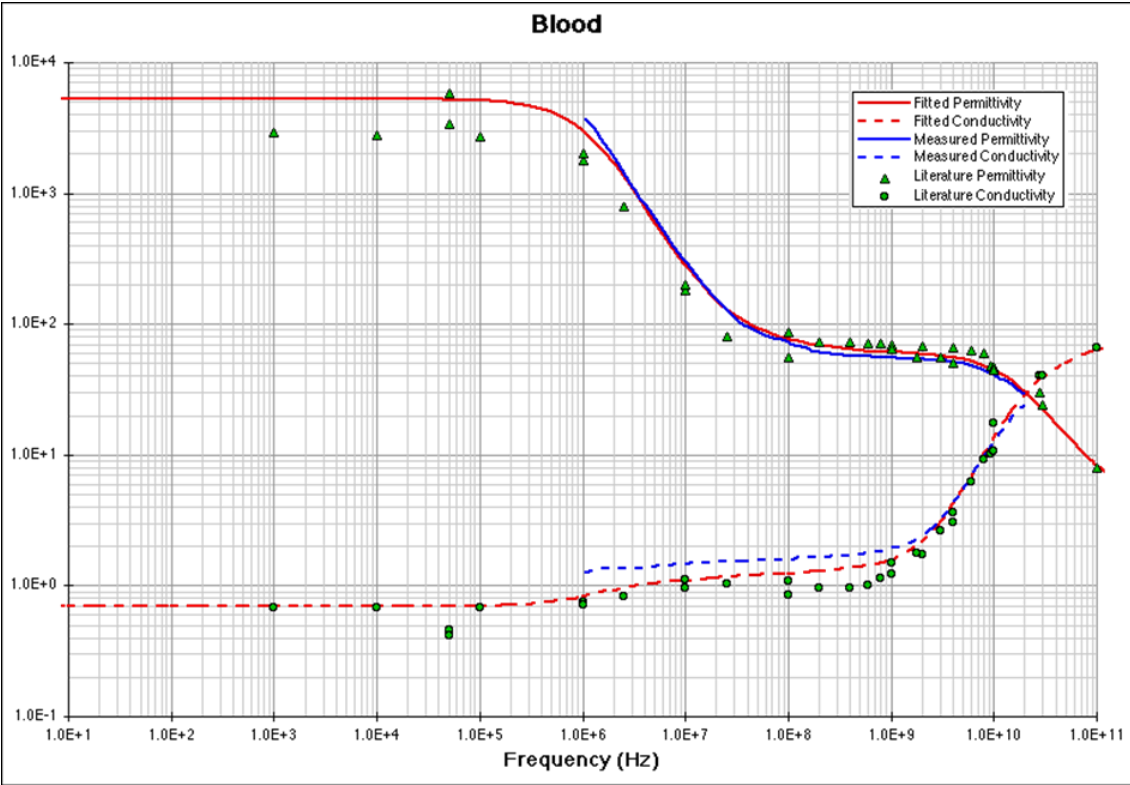


Figure 18. Permittivity and conductivity of blood: prediction of the model (black filled and dotted curves), experimental data at 37C (grey filled and dotted curves) and data from the literature (triangles and circles) [157]

Conversely, tissues of the same water content revealed various values for the dielectric characteristics. Thus, it takes more than just the percentage of water in the tissue to explain the reliance of the dielectric qualities upon water content. It was suggested that future research should take into account the ratio of free to bound water [175]. Furthermore, it was reported that it is crucial to consider whether the dielectric property data used in an investigation comes from ex-vivo biological tissues or in-vivo studies, as the properties can change after excision due to water loss and temperature change. In ex-vivo measures, blood flow is not considered [176]. Most of what is identified about the dielectric characterisation of tissues comes from measurements taken on samples surgically removed from a donor, with the duration between measurement and tissue death ranging from 5 minutes to 5 hours. These readings reveal dielectric information about tissue in a non-physiological state [154]. Therefore, parameters like blood perfusion, temperature, tissue dehydration, and ischemia effects are not accounted for in the data from ex-vivo studies [177]. The bio-physiological impact of death on the tissue and other factors affecting the physiological state of the tissue during and after excisions, such as tissue dryness, temperature fluctuations, or any physical damage to the sample, can affect the dielectric measurements [154]. Dielectric parameter changes as a function of post-mortem time have been seen in bovine brain tissue [109], and it was established that the oxygenation level and blood flow have a significant impact on the dielectric characteristics.

Consequently, the extent to which in-vivo properties diverge from those of ex-vivo tissues is highly debated [165], [177] [178], and numerous researchers asserted these differences. When [178] measured the relative permittivity and conductivity of ex-vivo breast tissues from 100 Hz to 8.5 GHz, they found that these parameters were lower than those in-vivo. Ex-vivo and in-vivo dielectric properties of selected tissues, from bovine, ovine, porcine, rat, dog, cat, and frog, vary greatly, with variations of up to 25% for permittivity and 30% for conductivity, according to research presented at the 2017 International Conference on Electromagnetics in Advanced Applications [172]. According to this study, all tissues, especially the kidney, spleen, and brain, showed greater than 10% variance in dielectric properties between species. Particularly for the spleen and the kidney, there is a fair amount of conductivity variance. In every instance, the variation exceeds the claimed uncertainty of the measurement system, which may result from the natural heterogeneity of each tissue or variation between species. In addition, the published

data may not reflect the actual in-vivo dielectric characteristics of biological tissue, even at a single frequency point [172].

2.3 Conclusion

Microwave sensors use EM radiation to detect and measure various properties of objects or materials. The theory behind a microwave sensor involves the transmission and reception of microwave signals, which are then analyzed to extract information about the object being measured. Developing a microwave sensor typically involves designing the transceiver system, selecting the appropriate frequency range, and optimizing the signal processing algorithms. Overall, transitioning from microwave sensor theory to measurements and testing requires careful consideration of the technical details and expertise in microwave engineering and measurement science. The possibilities and potentials of the MWI field are vast, as has been explained; nevertheless, these limitations must be addressed and handled first from the existing database of dielectric values and currently available sensors. The biosensor, discussed at length in the following chapter, was designed with the abovementioned considerations in mind from the start to where it is today for carotid plaque characterisation in the neck in vivo.

Chapter III - Implementation and Development of the Miniaturised Microwave Sensor Forethought for Diagnostic Purposes

The resonant technique is a widely used method in microwave sensing, which involves measuring the resonant frequency of a resonant structure in response to changes in the environment or the material being measured. This technique is commonly used in the design of various types of microwave sensors. A Complementary Split-Ring Resonator (CSRR) sensor was adopted in this specific application. Those techniques and theories are detailed in this chapter, along with the EM modelisation and simulation used to refine the biosensor.

3.1. Microwave measurement instrumentation

Research domains like material science, microwave circuit design, absorber development, and biological research have all realized the growing necessity of measuring the dielectric properties of materials at RF. Various techniques are available for gauging such subtle qualities, including those operating in the time domain, the frequency domain, with a single or dual port, and a few others. Each technique has its own set of limitations, such as a maximum frequency range, permitted materials, or operational domain. The complex dielectric parameters may be calculated from measurements of the reflection and transmission coefficients made with a Vector Network Analyser (VNA) (Fig.19), thanks to appropriate software development.

The dielectric characteristics of biological tissues can be measured using several techniques, including open-ended coaxial probe, transmission/reflection line method, free-space method and resonant cavity method. Among these techniques, open-ended and resonant approaches are the most widely employed [173].



Figure 19. Different existing types and models of the VNA [179]

S-parameters are a set of complex parameters of the microwave device that describe its behaviour as a function of frequency [180]. The full set of S-parameters of a two-port network includes the following:

S_{11} : Reflection coefficient at port 1

S_{21} : Transmission coefficient from port 1 to port 2

S_{12} : Transmission coefficient from port 2 to port 1

S_{22} : Reflection coefficient at port 2

Each S-parameter describes the ratio of the transmitted/reflected wave to the incident wave at a particular port and is a complex number, with the magnitude representing the power level and the argument representing the phase shift between the incident and the transmitted or reflected signals (Fig.20). S_{21} measures the power transfer from the input port to the output port of a two-port network generally, expressed in dB [152], [181]. It describes how much power is transmitted through the network and is an essential parameter for determining the gain of an amplifier or the insertion loss of a filter. In practice, in a ring resonator for example, the resonant frequency and amplitude are recorded as they are essential characteristics of a resonant device and can be determined from the S_{21} parameter versus frequency plot. The resonant frequency is the frequency at which the magnitude of S_{21} is at its maximum or minimum, and the amplitude is the magnitude of S_{21} at the resonant frequency.

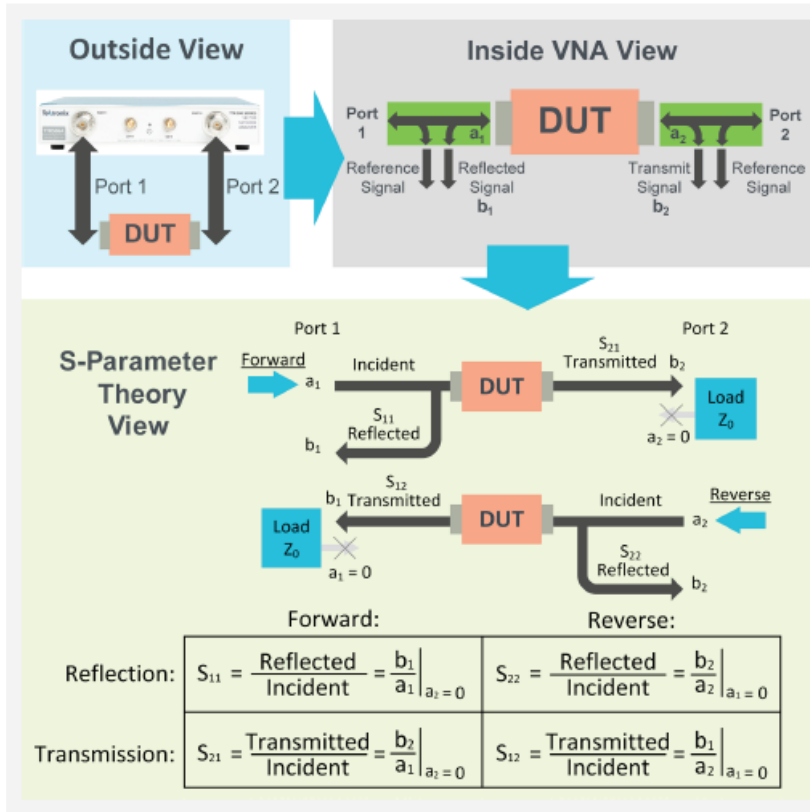


Figure 20. S-parameter theory [181]

3.2. Microwave Systems for dielectric constant measurement

1) Open-ended coaxial probe

It consists of a coaxial cable with its outer conductor removed at one end, exposing the inner conductor. The probe is pressed against a semi-solid or, more often, immersed in liquids. In this approach, microwaves are transmitted through the exposed inner conductor and interact with the material, producing a reflection that can be measured to determine the material's properties (Fig.21).

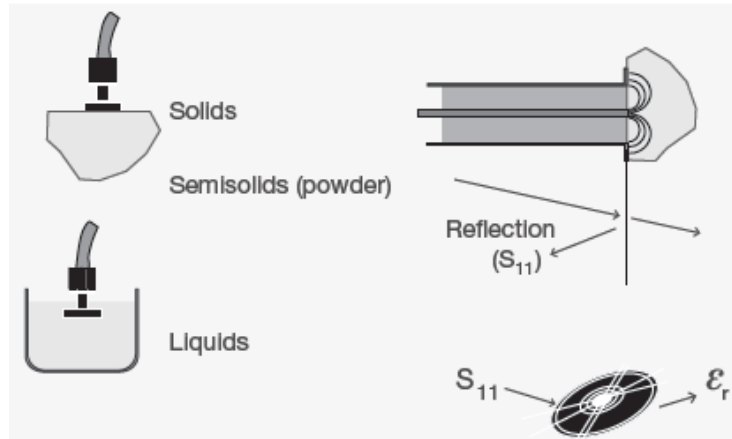


Figure 21. Coaxial probe method [152]

The open-ended coaxial probe is commonly used in the design and testing of microwave circuits, as well as in material characterization for industries such as telecommunications, aerospace, and agriculture. It is a widely spread technique as it does not need sample machining and sample preparation is simple. In addition, following the calibration step, the dielectric characteristics of many samples can be tested routinely in a short period. It is also easy to use, relatively low-cost and allows for non-destructive testing of materials.

However, in this technique, the only accessible measurement is the reflection, which is affected by air gaps for specimen measurement. Measurement accuracy can be affected by the probe dimensions and the surface conditions of the semi-solid material being tested, and the probe can only measure properties at the material's surface, not deeper within the material. Additionally, it requires calibration and careful handling to ensure accurate and consistent results [158], [182], [183], [184]. According to [158], [182], [183], this approach is the most appropriate for dielectric measurements of soft tissues in the microwave frequency range due to its capacity to evaluate tissues in a non-destructive manner with minimal sample manipulation, and it can easily be inserted within a regulated temperature setting and cover an extensive frequency range.

2) Transmission/Reflection line method

Placing a sample in a waveguide or coaxial line section and analysing the two ports' complicated scattering parameters using a VNA constitutes a Transmission/Reflection line measurement. Before taking the measurement, calibration must be accomplished. In many instances, the

procedure necessitates sample preparation, such as machining, to ensure that the sample fits appropriately within the waveguide or coaxial line. In the calibration step, various terminations are used to induce distinct resonant behaviour in the transmission line [185]. A maximum electric field is necessary for accurate dielectric measurements, achieved with open-circuited or other capacitive termination (Fig.22). The measurement method enables the permittivity and permeability of the dielectric material to be determined. Typically, coaxial lines and waveguides evaluate samples with moderate to high loss. Nevertheless, the air-gap effects restrict measurement precision, and when the sample length is the multiple of one-half wavelength in the material, the accuracy is low.

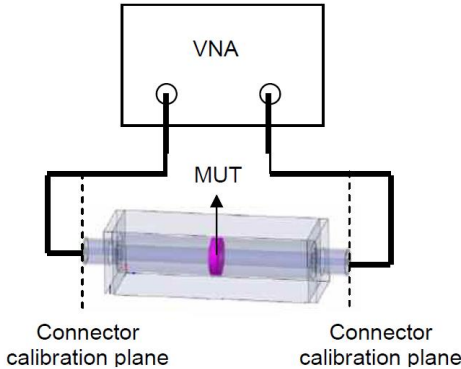


Figure 22. Transmission line method [180]

3) Free Space method

The free space method permits MUT measurements to be conducted in high temperatures or adverse situations and often operates at broadband frequencies. Typically, it employs two antennas located opposite one another and connected to a VNA (Fig.23) [185].

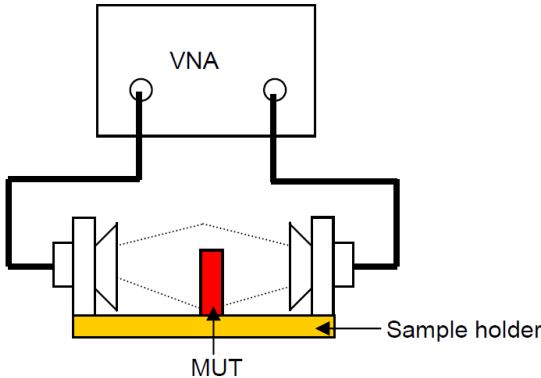


Figure 23. Free space method [180]

This method can be attractive as it allows high-frequency, non-destructive measurements. Moreover, it can measure MUT in a hostile environment, and the magnetic and electric properties can be studied. Nevertheless, the MUT must be large, flat, and have multiple reflections between the antenna and the sample's surface, in addition to the effects of diffraction at the edge of the sample.

4) Resonant (cavity) method

The most reliable methods for determining permittivity are resonant measurements. However, the approach has restrictions regarding the frequencies and loss characteristics of the materials that may be measured. Resonant method types include cavity resonators, antennas, split cylinder resonators, Fabry-Perot resonators and several others.

There are several forms of resonant measurements. Permittivity measurements and medium-to-high loss material measurements are compatible with perturbation methods. The low-loss measurement method conversely measures materials with low loss utilizing larger samples [185]. With resonance characteristics in a cavity dependent on the MUT, its quality factor and resonant frequency can be monitored to identify the dielectric properties. The dielectric characteristics of an empty cavity can be determined by measuring its resonant frequency and quality factor. The second step is to repeat the measurement once the cavity has been filled with MUT. The material's permittivity can then be calculated using frequency, volume, and Q-factor. The resonant method is powerful because it can measure extremely small MUT and use an approximate expression for sample and cavity fields.

Many kinds of cavities have been proposed (rectangular, circular etc), but in all cases, they need a small piece of the studied sample because the principle is to create a minor perturbation of the device's resonant frequency. Moreover, it needs VNA with high-frequency resolution and is limited to a narrow frequency band (Fig.24).

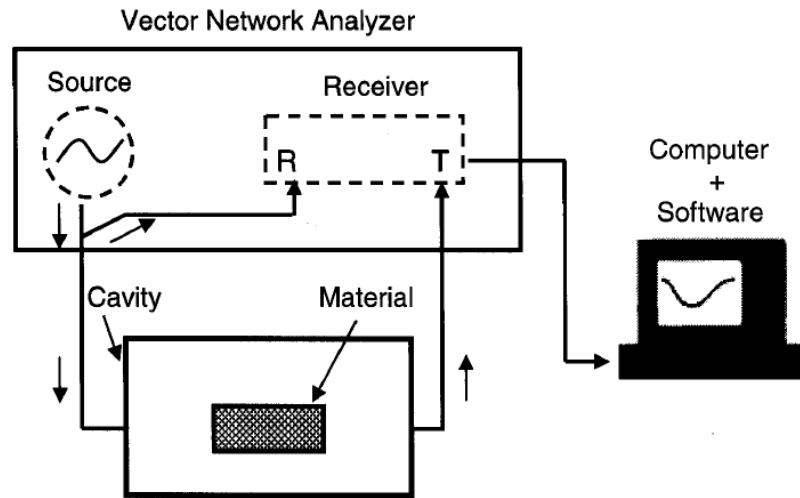


Figure 24. Resonant cavity measurement [186]

This thesis will cover this technique in-depth as it was the chosen method. Therefore, it will be described in greater depth than the other techniques in the next section. Figure 25 synthesizes the techniques for constant dielectric measurements. Only one of them, the resonant cavity, is a resonant system; the other three are all propagation systems.

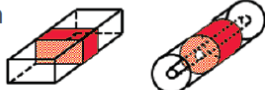
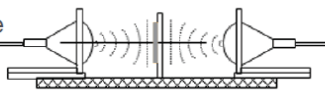
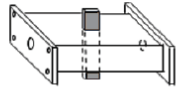
Coaxial Probe ϵ_r		Broadband, convenient, non-destructive; Best for lossy MUTs; liquids and semi-solids
Transmission Line ϵ_r and μ_r		Broadband Best for lossy to low loss MUTs; machineable solids
Free Space ϵ_r and μ_r		Broadband; Non-contacting Best for flats sheets, powders, high temperatures
Resonant cavity ϵ_r		Single frequency; Accurate Best for low loss MUTs; small samples

Figure 25. Comparison between the measurement methods [152].

3.3. Sensor design and fabrication process

Several criteria have been considered to be able to investigate biological tissues in-vivo in the medical environment. First, a planar sensor was proposed (patch antenna, planar resonator) that can be applied directly on the human body, and its frequency response would be modified by contact with the tissue; this device is non-invasive and non-destructive. Secondly, the resonant technique was chosen due to its sensitivity related to the resonant frequency shift as a result of adding the dielectric material, i.e. it presents good precision in a narrow frequency band. In addition, classical half-wave ring resonators have been widely used to characterise solid dielectrics; nevertheless, the cavity dimensions in the microwave range of 2 GHz are relatively important ($\lambda/2 = 7.5$ cm) in free space.

All the above are further clarified in the following section.

3.3.1 Resonant technique with planar sensor

The first resonator design studied was a simple ring resonator [115], exhibiting good performances but requiring a wide tissue surface. Later, another sensor design [187], [188], based on a metamaterial structure, consisted of a CSRR engraved in the ground plane and fed with a microstrip line. One of the main interests was reducing the surface in contact with the tissue since the dimensions are in the range of $\lambda/10$, λ being the free space wavelength in vacuum at the operating frequency of the resonator ($\lambda = 12.5$ cm). Several dielectric substrates with different heights have been tested for better performance to reduce the size. Since the last two decades, these kinds of resonators have been used extensively to determine the dielectric permittivity of liquids and low losses dielectric materials, but fewer experiments are related to biological tissues, which often exhibit high losses.

Split Ring Resonators (SRR) and their complementary (CSRR) have been widely introduced to produce compact filters (Fig. 26). From an EM point of view, these two structures are somewhat equivalent, with metal strips replacing dielectric slots. These structures have been studied in reference [189]. The CSRR here is designed in a metallic plane covering a dielectric substrate. It consists of two concentric metallic rings, each interrupted by one slot connected to the

metallic plane. Due to its weak dimensions, this structure can be considered quasi-localised at the resonant frequency. The dimensions of the spacing and width of the rings and slots can be adjusted to the chosen resonance frequency for a given thickness and dielectric permittivity of the substrate under the metallic plane. A transmission line must feed this resonator, and due to the geometry, a single microstrip line engraved on the other side of the dielectric substrate allows for obtaining a band-stop filter.

Several shapes have been designed (circle, rectangular, hexagonal) with no relatively significant improvements in the characterisation of tissues under test. The circular shape was chosen.

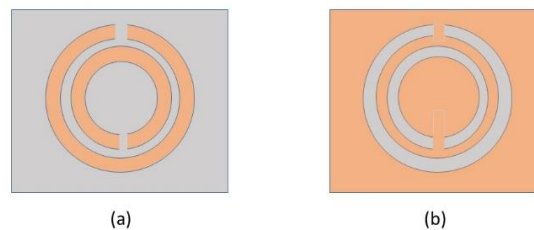


Figure 26. Design of structures (a) SRR (b) CSRR

3.3.2 Sensor design

The sensor of a circular shape with a microstrip feeding line was fabricated on a commercial FR4 substrate with $\epsilon_r = 4.6$, $\tan \delta = 0.02$ at 1 MHz and a thickness of 0.73 mm; the metallisation thickness is $t = 35\mu\text{m}$. Dimensions of the resonator were optimised with EM software (Ansys-HFSS), and as mentioned previously, the resonant frequency was chosen to be around 2.2 - 2.4 GHz. The dimensions of the circular CSRR are given in Figure 27.

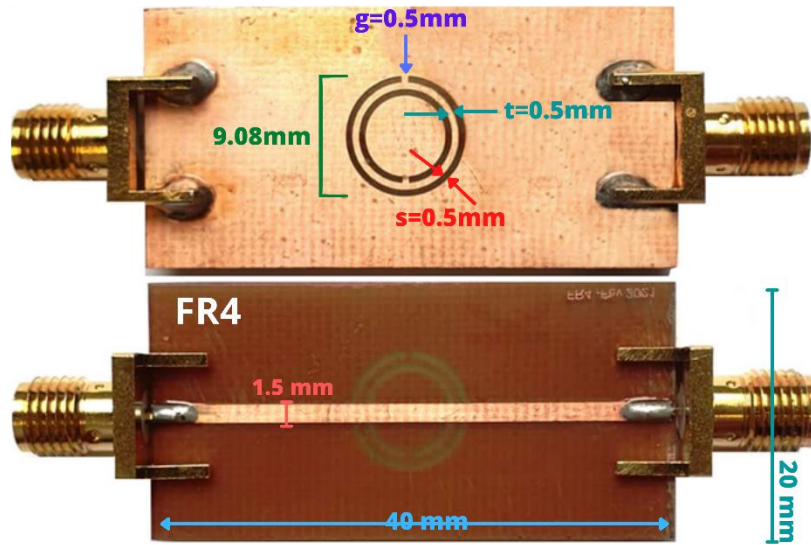


Figure 27. CSRR dimensions

As expected in this frequency range, the resonator's size is significantly tiny ($\sim 1 \text{ cm}^2$) compared to conventional ones. Another reason to choose the CSRR structure for our experiments is due to the geometry of the feed line; the microstrip structure enables the excitation of the CSRR with an electric field perpendicular to the ground plane where the CSRR is engraved. Then the CSRR is coupled capacitively to the optimal feed line for the geometry (the electric field is parallel to the CSRR axis) [190]. As a result, the dielectric sample (called the “superstrate” in this instance) is applied on the free surface of the resonator in near-field conditions and modifies the resonance condition. Depending on the substrate's thickness and primarily losses, the empty quality coefficient is relatively high, around 80 to 100.

The resonant frequency of the unloaded resonator (without sample), simulated using HFSS, was almost the same as the one measured $f_0 \approx 2.27 \text{ GHz}$, with a minimum value of -23.3 dB ; the Q-factor measured value is approximately about 50 (Fig.28).

LPKF ProtoLaser S4 laser system with LPKF Circuit-Pro software was used to fabricate the CSRR sensor. Complex RF and microwave Printed Circuit Boards (PCBs) and digital and analogue circuits can be quickly and easily prototyped with this system. It can produce precise shapes in a wide variety of substrates, including copper-clad FR4, aluminium-coated PET films, ceramics, Duroid, and PTFE. The precision of the engraving is roughly $\pm 30 \mu\text{m}$, which often contributes to a 70 to 100 MHz resonant frequency shift between measurements and

simulations. These uncertainties in the geometrical characteristics of the structure are addressed in the EM simulation's part to obtain fine modelling of the sensor.

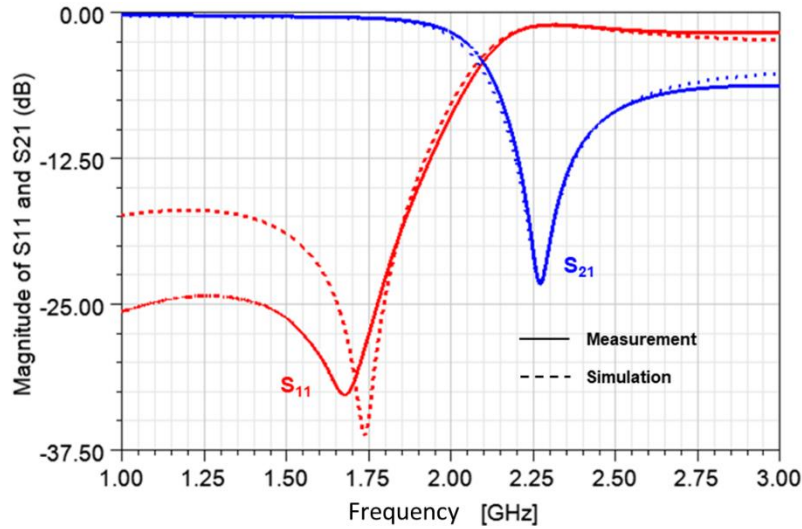


Figure 28. $|S_{11}|$ and $|S_{21}|$ of the retro simulation of the resonator vs real measurements

Due to the presence of the two SMA connectors, it was necessary to extend the microstrip line on the substrate, which has a dimension of 40 x 20 mm; this microstrip structure is matched to 50 Ω , allowing S-parameter measurements with a VNA ZNB20 from Rohde & Schwarz ([Appendix 1](#)).

Calibration of the VNA is a critical part of operating it. Various calibration algorithms exist. This study conducted the reflection and transmission (TOSM calibration) using an 85025 D kit for 3.5 mm diameter cables. Since the model chosen had a resonant frequency of around 2.4 GHz, the frequency range chosen in the VNA was 1 to 4 GHz. The resonator was then connected via the coaxial cables to the VNA, and the complete set of scattering parameters (S-parameters) was recorded.

3.4. Equivalent electrical model of CSRR

The equivalent electrical model of this resonator (Fig.29) was proposed in several publications; the most representative used here was proposed by [189]. This quasi-static model can be separated into two parts. The first one corresponds to the coupling between the microstrip

feeding line and the resonators; classical models give the values of inductance and capacitance by unit length, and the T-schema (in the symmetry plane of the CSRR) was derived by adjusting the coupling length. The second part corresponds to the resonator represented by a parallel tank (L_R , C_R , R_R) that stores EM energy. The elements are related to the coplanar structure of the resonator, the upper surface corresponding to the substrate, and the lower one to the vacuum. Adjustments of the equivalent circuit values with the S-parameter measurements are obtained by simulations with PathWave Advanced Design System (ADS) software after de-embedding the access lines.

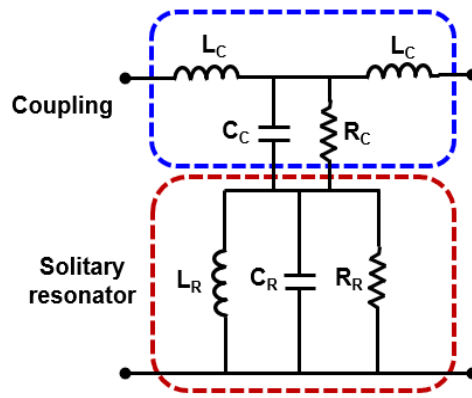


Figure 29. Equivalent electrical schema of the resonator

The resonant frequency, corresponding to the minimum of the transmission coefficient S_{21} , is given by the equation:

$$f_0 = \frac{1}{2\pi\sqrt{L_R(C_R + C_C)}} \quad (16)$$

It occurs when the magnetic energy in the inductive L_R is equivalent to the electric energy stored in the C_C and C_R capacitors [190].

Table 6. Extracted parameters of the equivalent electrical model of the resonator empty

Coupling elements		CSRR alone	
L_C (nH)	2.6	L_R (nH)	2.7
C_C (pF)	0.96	C_R (pF)	0.87
R_C (k Ω)	5	R_R (k Ω)	4

Using characteristic frequencies obtained on the S-parameters and the Z_{11} input impedance, the resonator elements' values in the absence of a sample were derived. The principle of extraction was outlined in detail by our team in [191]. The extracted values of the equivalent circuit obtained after EM simulations and optimisations with ADS are given in (Table.6). ADS modelling, and HFSS simulation results were compared with the experimental observations (Fig.30).

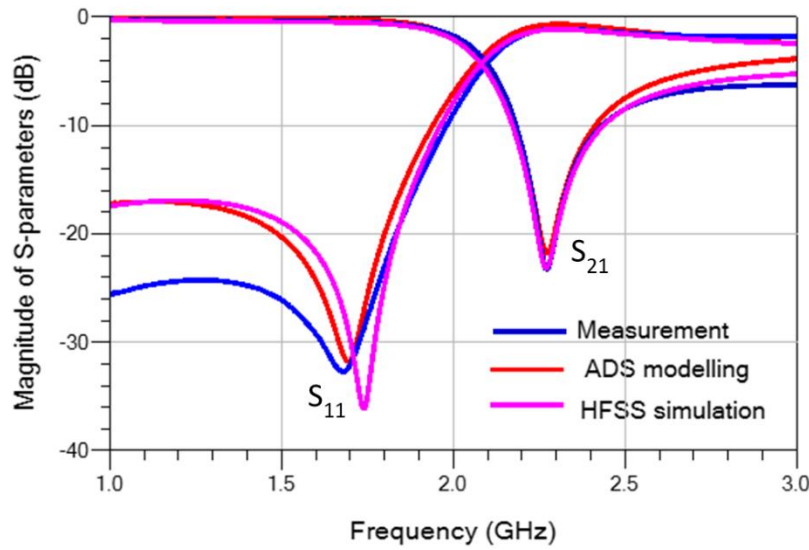


Figure 30. Graph comparing the modelling on ADS with the simulation on HFSS and the experimental measurements.

3.5. Adaptation of the sensor for biological tissue measurement

The preceding resonator structure can be used to characterise solid dielectric samples by putting them on the lower free surface of the CSRR. Consequently, this procedure mainly increases the capacitance C_R of the CSRR resonator itself and thus decreases the structure's resonance frequency.

Since excised biological tissues are mostly wet, water content is inherent to their structure and often stored in a liquid solution. A glass blade of 120 μm thickness was added to avoid short-circuiting between the rings due to the humidity. This dielectric blade ($\epsilon_{rv} \sim 7$, $\tan \delta = 0.02$), placed on the lower surface, reduced about 110 MHz the sensor's resonant frequency and was taken into account in EM and electrical simulations (Fig.31).

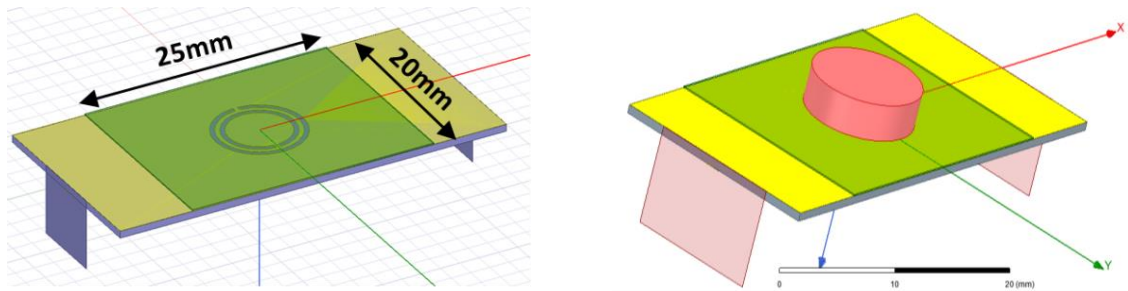


Figure 31. Design of the structure with glass slab for EM simulations with HFSS:
 (left) with glass blade; (right) with sample on glass blade

In order to obtain better reliability of the experimental results, the support of the resonant structure (with SMA connectors and glass blade) was installed in a Plexiglas framework explicitly built for this resonator, with the size and shape adjusted to assure its stability. The Plexiglas structure consisted of a base and a top part, maintaining the cable links with the VNA. Another frequency shift by ≈ 12 MHz was introduced. Therefore, with the glass layer and the Plexiglas structure, the f_R measured is 2.117 GHz, $|S_{21}| = -21.5$ dB, to be compared to f_R simulated = 2.118 GHz, $|S_{21}| = -21.6$ dB (Fig.32).

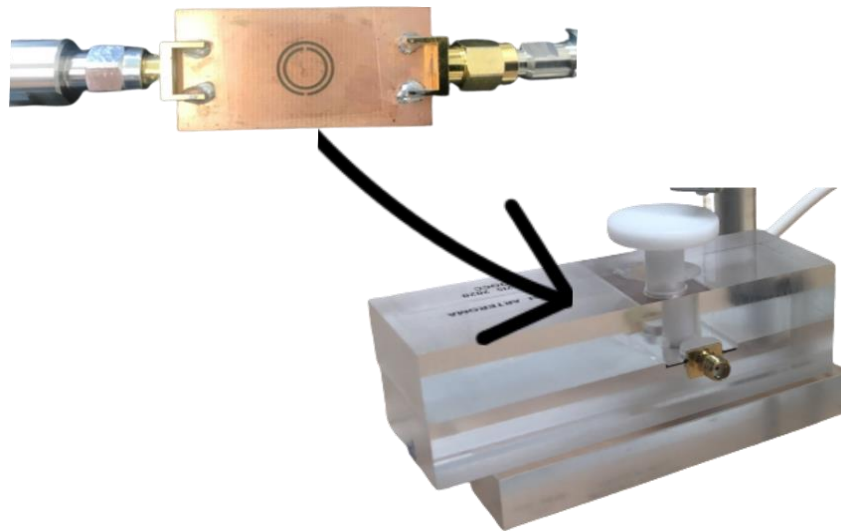


Figure 32. The CSRR covered with the glass blade and inserted inside the plexiglass structure.

A global downshift $\Delta f \approx 120$ MHz must be considered to compare simulation results with real measurements. Therefore, the effect of the glass blade, in addition to the plexiglass support, are considered together in the simulation by adding an equivalent layer $\epsilon_r = 7$, $\text{tg } \delta = 0.02$.

Comparing the simulated parameters in Table 6 and Table 7, it is observed that the coupling elements of the equivalent circuits have sensibly the same value and, similarly, the inductance of the CSRR. This supports the fact that introducing a dielectric blade (glass) on the CSRR surface changes only its capacitance C_R . When measurements were done with this test cell, the frequency $f_R = 2.117$ GHz with parameters given in Table.7 were taken as the reference frequency in unloaded conditions, i.e., in the absence of a dielectric sample.

Table 7. Equivalent electrical parameters of the resonator with glass slab and Plexiglas mount.

	Coupling elements		CSRR + glass+ Plexiglas Structure		
	Model	Optimised		Model	Optimised
L_C (nH)	2.1	2.1	L_R (nH)	2.5	2.48
C_C (pF)	0.86	0.86	C_R (pF)	1.38	1.39
R_C (k Ω)	4.4	5	R_R (k Ω)	3	4

3.6. Calibration of the sensor with ideal samples

As mentioned previously, the frequency f_R corresponding to the minimum of $|S_{21}|$ matches the resonance of the inductance of the resonator in parallel with the capacitances C_R and C_C in the equivalent circuit; this frequency is given by equation (16) with the parameters of the circuit in Table 7. In the presence of the superstrate, the capacitance C_R is increased, which lowers this resonance frequency; this frequency, denoted $f_{R(\epsilon_{rs})}$, is dependent on the value of the superstrate's dielectric constant ϵ_{rs} . Thus, the frequency shift $\Delta f = (f_{R(\epsilon_{rs})} - f_R)$, where f_R is the value of the resonance frequency in the absence of the studied dielectric sample.

In order to calibrate the frequency shift of the resonator in the presence of the MUT, EM simulations (HFSS and CST) can be done by charging the resonator on the downside of the CSRR, as shown in Figure 31.

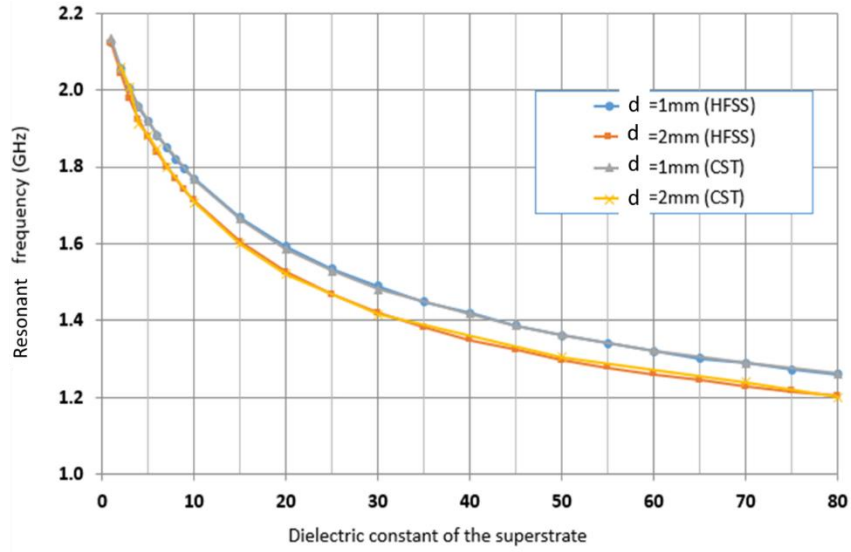


Figure 33. Simulation of superstrates of two different thicknesses using HFSS and CST

The typical range of ϵ_{rs} for biological tissues extends from 1 to 60. Two thicknesses of the superstrates (1 & 2 mm) were first analysed and compared using HFSS and CST (Fig.33). The value of $|S_{21}|$ at resonance depends on sample losses as the resonator's Q-factor since the superstrate's losses lower the resistance R_R and contribute to widening the resonance hollow.

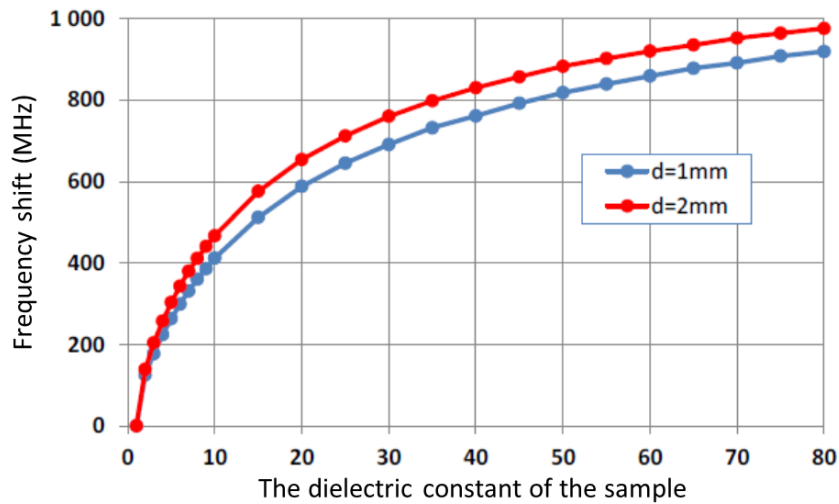


Figure 34. Δf_r as a function of the ϵ_{rs}

Figure 34 represents the simulation of the relative frequency shift Δf_r as a function of the dielectric permittivity (ϵ_{rs}) for two superstrates' thicknesses showing that as the dielectric constant increases, the Δf_r increases.

Moreover, Figure 35 shows that the Δf_r increases with the thickness of the superstrate; however, a saturation effect can be observed in the thicker samples.

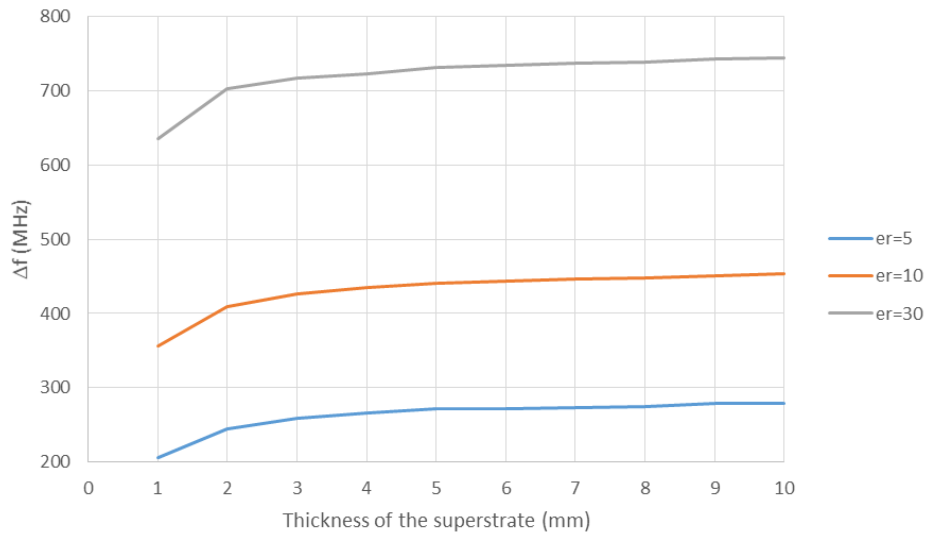


Figure 35. Saturation effect observed as the thickness increases

3.7 Conclusion

In conclusion, this chapter has presented a broad overview of the theories and computations related to the biosensor used in this thesis. The knowledge and understanding gained from this chapter form the foundation for the bench testing of the carotid plaques using this biosensor, which will be explored in detail next. In addition, medical imaging and histological analysis used are thoroughly explained in the next chapter.

Chapter IV - Exploring Atherosclerotic Carotid Plaques Through Multiple Modalities: Medical Imaging, Histology, and Microwave Biosensor

This study aimed to investigate the characteristics of carotid artery lesions, focusing on identifying vulnerable plaques. To achieve this, a multi-modal imaging approach was employed, which included preoperative ultrasound and CT scans, postoperative examination with the microwave sensor, and histopathological examination as the gold standard for plaque classification. In addition, surgeons answered a visual intraoperative scoring questionnaire to evaluate the plaques. The information presented in this chapter will provide a clear understanding of the procedures used and how the data were collected and analysed, which is crucial for interpreting and validating the study's findings.

4.1. Study design

The medical part of this thesis took place in the “*Service de chirurgie vasculaire et endovasculaire - Centre aortique tertiaire de La Pitié Salpêtrière*”.

Between January 2020 and October 2022, fifty carotid arteries from forty-nine patients (14 females, mean age 73 ± 9 years) were included. Indications for CEA followed cerebrovascular disease recommendations [47]. Every patient underwent preoperative DUS imaging and CTA. Prior carotid artery surgery, endovascular operation on the same side, or prior cervical radiation were exclusion factors. Lesions were considered symptomatic if the patient had a TIA or stroke ipsilateral to the carotid lesion being studied within the previous two months. Silent infarcts and lacunar symptomatology, diagnosed by a neurologist based on clinical and brain CT scan and/or MRI located ipsilateral to the stenosis, were also considered symptomatic.

The institutional review board at “*Hôpitaux Universitaires Pitié Salpêtrière - Charles Foix*” approved the study, and patient consent was waived, given the nature of the study. Patient demographics, comorbidities including age, sex, obesity (defined as body mass index ≥ 30 kg/m²), smoking status, hypertension, diabetes mellitus, coronary artery disease

(CAD) and lower extremity peripheral arterial disease (PAD) were recorded at the time of enrolment. The use of antiplatelet agents, oral anticoagulant therapy (OAT), statins and antihypertensive drugs (angiotensin-converting enzyme inhibitors [ACE-I]/angiotensin receptor blockers [ARBs], β -blockers [BB]) administration was documented.

In the case of asymptomatic carotid stenosis, the interval between the first surgical consultation and the operation was shorter than six weeks. In contrast, in the case of symptomatic carotid stenosis, this delay did not exceed two weeks (typically less than a week).

4.2. CT

Patients who were selected for the CEA had a Multidetector CT (MDCT) scan with 64 detector rows or more acquired in the two months before surgery, extending from the aortic arch to the cranioencephalic region. All patients underwent an unenhanced test followed by a contrast-enhanced examination. They were injected with 50–100 mL of contrast medium at a rate of 3–5 mL/s. Among the technological aspects of CT were the following: Matrix size: 512x512; slice thickness: 0.6mm; interval: 0.6mm with a soft filter kernel. A senior radiologist* with 10 years of experience in cardiovascular imaging reviewed independently and blindly to the symptoms both carotid arteries of each patient using a dedicated vascular software (Terarecon, USA). For carotid arteries, luminal stenosis (in % of diameter and surface), visual (calcified, non-calcified, mixed) and quantitative assessment of the plaque with the different plaque components regarding HU values as described above were noted.

Images of the ICA in axial view, as well as 2 cm above and below the bifurcation, were utilised (Fig.36). External carotid artery analysis was not performed. The extracted images were analyzed using the MIMOSA program in DICOM format. Using this program, it is feasible to highlight particular regions of interest that define the borders of the carotid plaque in successive axial images and to determine the total number of voxels and the number of voxels in distinct attenuation value ranges inside these regions of interest. The severity of stenosis in the carotid artery was measured using the NASCET system. The existence of plaque ulceration was noted according to its width (at least 5 mm). The software Terarecon was used to perform the quantitative analysis of the plaque. Lumen volume, plaque volume, and total volume (plaque

volume plus lumen volume) were semi-automatically quantified in cm^3 in all carotid arteries scanned. Then, the HU thresholds were used [192] to distinguish between the fibro-fatty ($60 < \text{HU}$), fibrotic ($=60\text{-}130\text{HU}$), and calcified ($>130\text{HU}$) regions of the plaque in order to compute each volume in cm^3 (Fig.37).

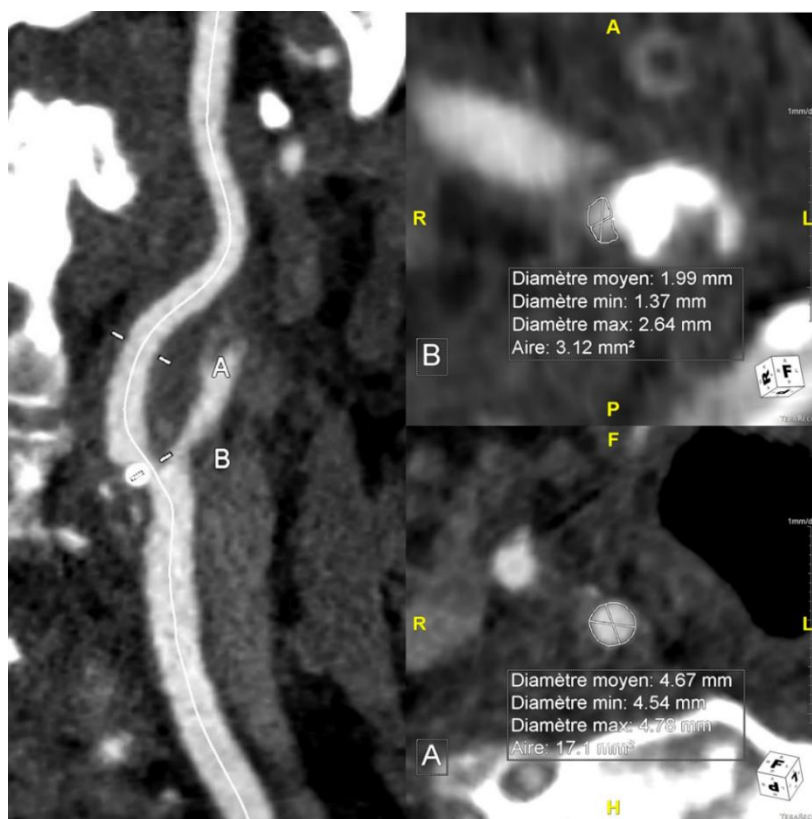


Figure 36. Carotid artery stenosis quantification using the NASCET methodology (72% stenosis noticed here)

In order to standardize the volumes, the relative proportion of each plaque component was measured as the percentage of the plaque volume. In addition, to calculate the PVFA, two ROIs of $2,5 \text{ cm}^2$ were manually traced for each patient in the perivascular fat in the axial plane at the site of maximal stenosis or minimal diameter of the carotid bulb when no significant stenosis was described (Fig.38).

**Dr Etienne Charpentier, Unité d'Imagerie Cardiovasculaire et Thoracique (ICT), Hôpital de la Pitié Salpêtrière - Paris.*

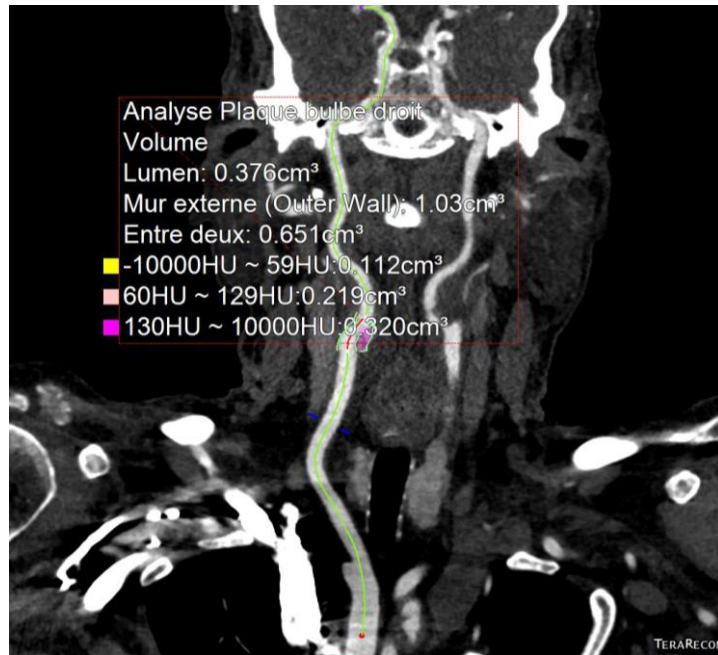


Figure 37. Plaque characterization with Terarecon software in a 85-year-old patient. After the segmentation of the right carotid artery plaque, the software calculated the three different components using HU threshold: fibrofatty (<60HU), fibrotic (60-130 HU).

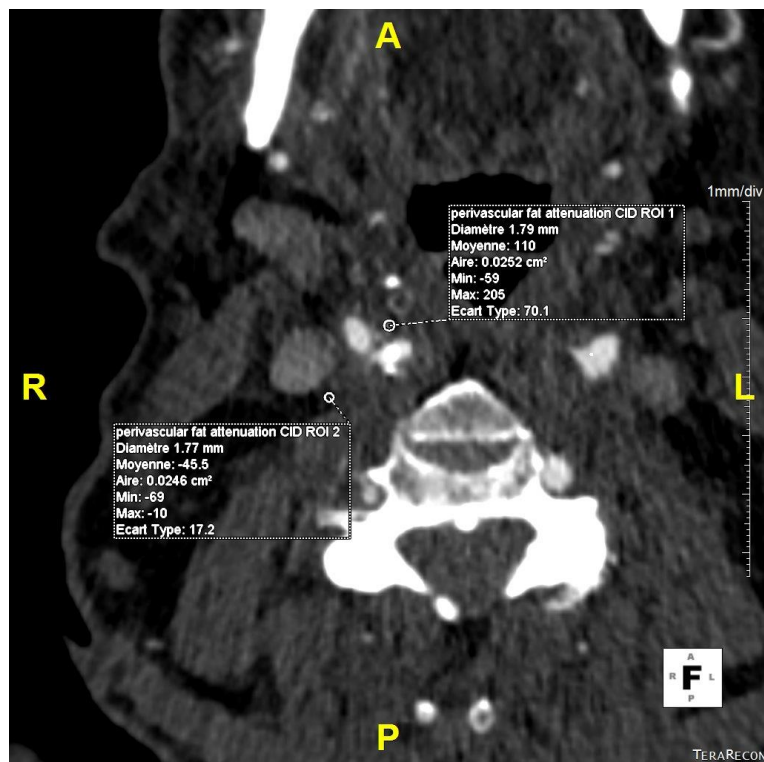


Figure 38. PVFA measurement with two ROIs placed on an axial plane at the level of maximal stenosis in an 85 years old patient.

4.3. DUS

Before surgery, patients had a Doppler Ultrasound performed by myself, a certified sonographer. Two ultrasound machines were used. The patients were examined with an L12-5 Linear Probe transducer and a Philips Affiniti 70 ultrasound equipment in the recovery room before the operation. Some patients were scanned the day before the operation using a Philips iU22 ultrasound system with a linear probe in the ultrasound outpatient clinic.

The carotid plaque was demonstrated using both grayscale and colour Doppler imaging. The degree of stenosis was evaluated using the NASCET criteria. Variables such as peak-systolic and end-diastolic velocities and internal carotid artery to common carotid artery ICA/CCA ratio were recorded. The images were saved in DICOM format and filed away for subsequent analysis. An existing classification system of plaque surfaces was used [52], [61], which divided the surface details into three categories: anfractuosity (more than two millimetres in depth), irregularity or soft surface. Gray-Weale's classifications were used to define plaque echogenicity [35], [55]. Plaques of type 1 were uniformly echolucent; those of type 2 were predominately hypoechoic; those of type 3 were predominately isoechogenic or hyperechogenic; those of type 4 were uniformly isoechogenic or hyperechogenic; and those of type 5 were indistinguishable due to dense calcification and acoustic shadows (Fig.39).

Due to the lack in the literature of a standard detailed carotid ultrasound report, a complete report was created by myself and was used for each patient ([Appendix 2](#)). I recorded these specifics for each patient's operated side (and, when possible, the opposite side). The report was modified and approved by two senior angiologists*.

**Dr Marie-Pierre Gobin-Metteil, Service d'Imagerie Morphologique et Fonctionnelle (SIMF), Centre hospitalier Sainte-Anne – Paris.*

**Dr Josette Le Doeuff, Service de Chirurgie Vasculaire et Endovasculaire, Hôpital Pitié Salpêtrière.*

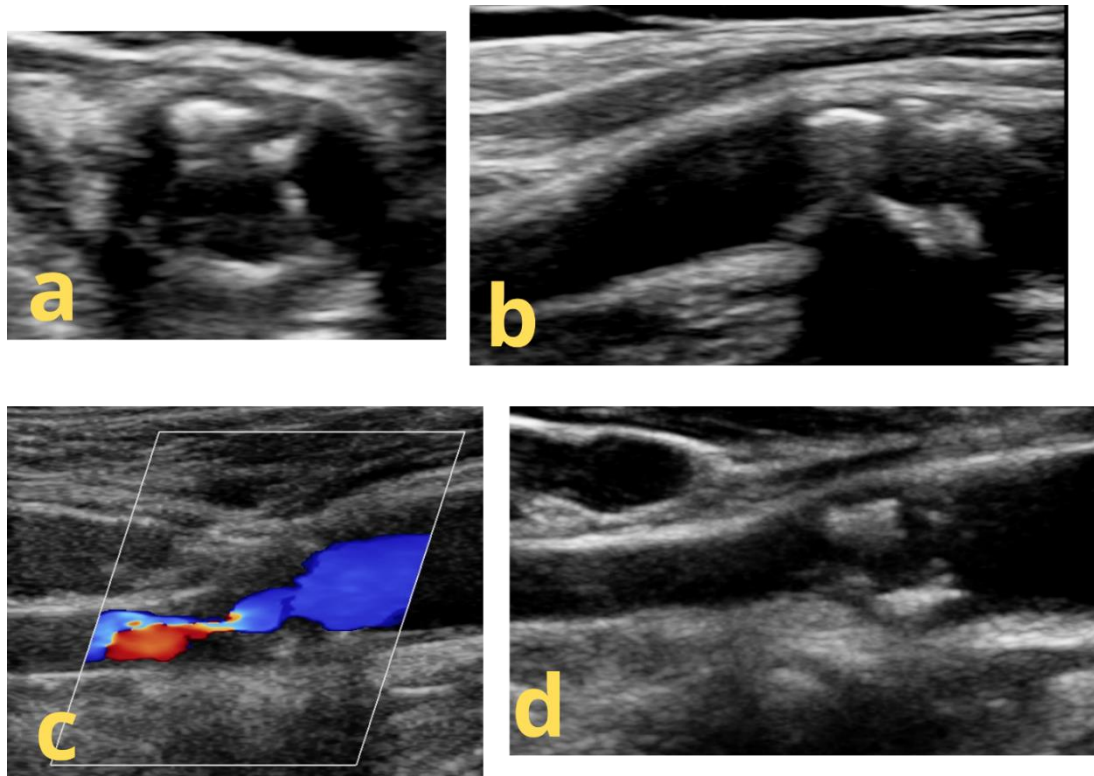


Figure 39. a) Transverse photo of an irregular heterogeneous plaque b) the same plaque in a longitudinal view showing acoustic shadowing. c) Colour Doppler was used to visualise the hypoechoic regions of a heterogeneous hypoechoic plaque. d) The same plaque without colour Doppler challenging to visualize the entire plaque.

4.4. CEA

Patients underwent surgery while under general anaesthesia. Before cross-clamping, the systolic pressure was set to 160 mmHg. Eversion carotid endarterectomy (eCEA) was conducted to excise carotid plaques as a single specimen (Fig.40), which was then split longitudinally, i.e. parallel to the lumen, by the vascular surgeon into two similar samples. A high-definition photograph of the plaque was captured. One specimen was immersed in 4% formol and sent for histopathological analysis (labelled with the protocol name), while the other was maintained in saline for MWI measurements as the bench testing was not possible directly after the operation, so this step ensured that the sample did not dry out. However, for the final few samples, rapid transit to the laboratory was guaranteed; thus, they were analysed without being submerged in physiological serum.

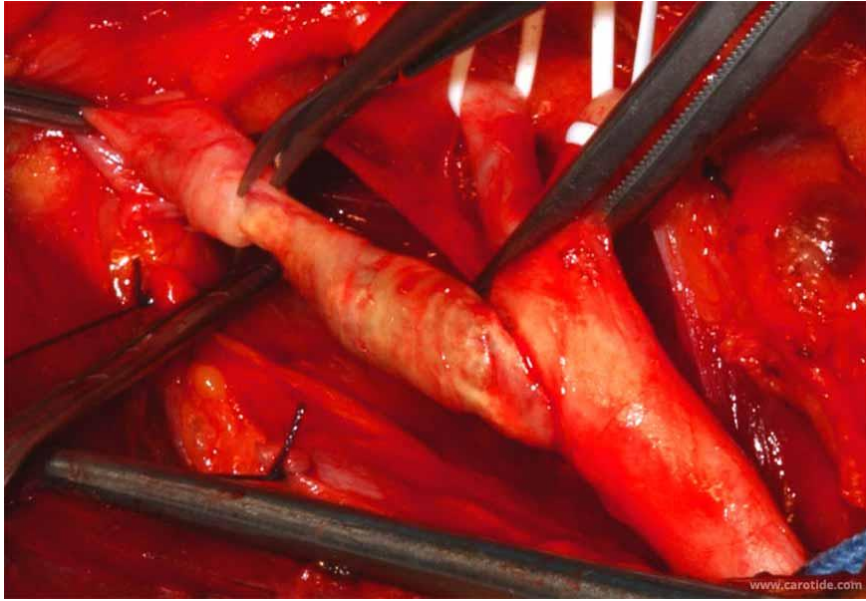


Figure 40. Van Mahle Eversion carotid endarterectomy technique [193]

The patient's excel sheet, including their baseline data, was then updated with all the surgical details. Information collected during surgery includes the date of surgery, duration of hospitalisation, post-operative stroke / TIA, date of post-operative stroke / TIA if happened, re-intervention within 30 days of surgery (type of re-intervention and details), death <30 days after the operation, and post-op doppler ultrasound findings.

4.5. Surgical observation score

Despite the fact that reports of intraoperative visual evaluation of carotid plaques are scarce, i found only one study that used this model [64]; one may believe that experienced surgeons are able to differentiate plaques that are highly fibrotic and calcified from the ones that are soft and display obvious signs of hematoma/haemorrhage visually. Therefore, a visual scoring sheet was created for this purpose ([Appendix 3](#)). The HD photographs taken during CEA were included in those sheets (Fig.41). Each patient was assigned a visual scoring sheet.

The questionnaire was sent to nine experienced vascular surgeons blind to the lesion and the patient's status; these surgeons subsequently assigned a plaque score. The goal was to concentrate on parameters pertinent to the clinical behaviour of the plaque and compatible with

other techniques. This study aimed to ascertain whether the intraoperative visual evaluation was helpful for plaque status.

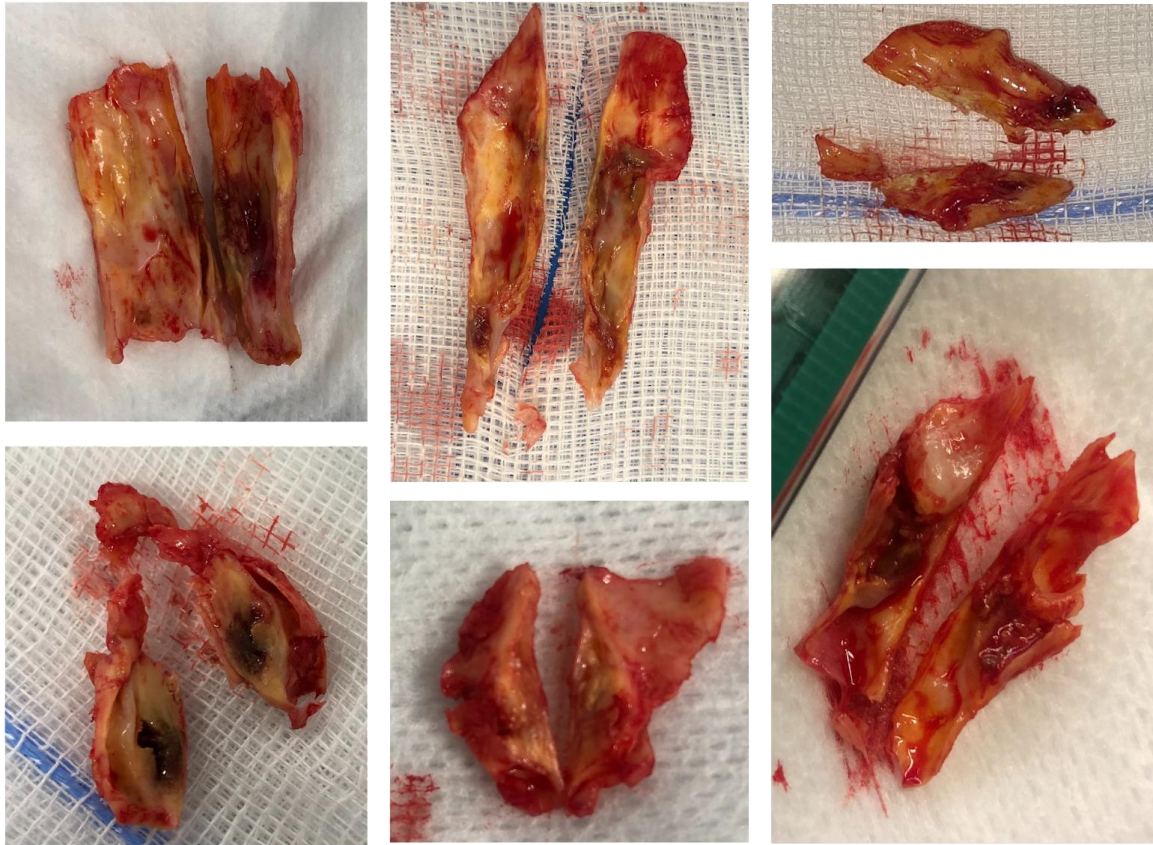


Figure 41. HD photos of a few plaques of different natures included in the questionnaire.

4.6. Histopathology

The histological study of the carotid plaques was performed by an experienced pathologist* and a digital pathology engineer* who were unaware of the other modalities' clinical information and outcomes. The samples were fixed in 10% buffered formalin before being decalcified with a Surgipath Decalcifier II solution (Leica Biosystems) and then embedded in paraffin. Histological slices were cut to a thickness of 3 microns and stained with H-E-S staining (hematein, eosin, saffron) using a slide stainer (Tissue-Tek Prisma SAKURA). A Nanozoomer Hamamatsu scanner was utilised to scan the complete sectional area of every slide at 40x magnification with a resolution of 0.24 micron/pixel. The digital slides in NDPI format

were later inspected on high-definition screens (BARCO Coronis Fusion) to determine the different tissue types. The entire section was observed for all samples.

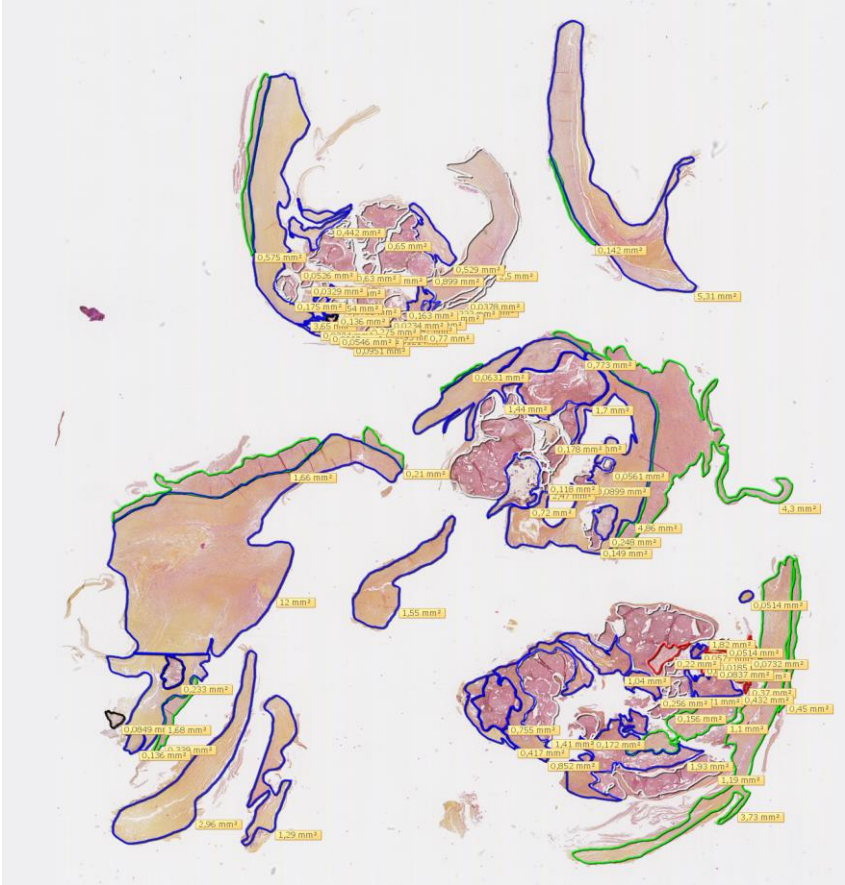


Figure 42. Semi-quantitative analysis of each plaque

Moreover, whole sections were manually outlined with high precision using Viewer (NDP.view2 +) to achieve a well-defined mapping of the area of each component of the specimen (Fig.42). This semi-quantitative analysis was implemented to ascertain the presence of calcification, OM, LRNC, IPH, and fibrous cap (Table.8).

Plaques with a large LRNC, thin fibrous cap, and IPH were considered vulnerable. Qualitative analyses were conducted afterwards to endorse the results (Fig.43).

* M. Gilles Le Naour & Prof. Isabelle Brochériou, Service d'Anatomie et de Cytologie Pathologiques, Hôpital Pitié Salpêtrière.

Table 8. The values collected and calculated for each plaque

Patient 48	Value	%
Fibrosis	42.08	38.86
Partially calcified fibrosis	0	0
Inflammatory fibrosis	8.93	8.25
LRNC	22.46	20.74
Partially calcified LRNC	14.17	13.08
Calcification	3.47	3.20
Very calcified fibrosis	0	0
Very calcified LRNC	0	0
Media	16.49	15.23
IPH	0	0
Intima	0.65	0.607
Adipose tissue	0	0
Fibrosis	51.02	47.11%
LRNC	36.63	33.83%
Calcification	3.473	3.20%
Total tissue	108.283215	

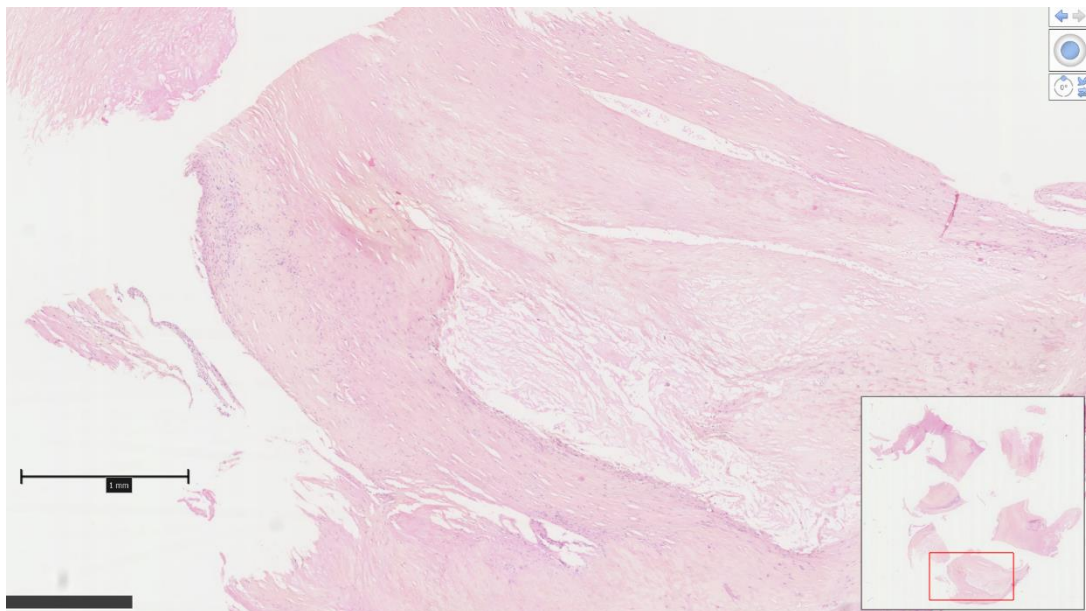


Figure 43. Qualitative analysis of the entire plaque

4.7. Microwave

The configuration of the apparatus for the measurements of the carotid plaques needed to be ensured for the reproducibility and reliability of the results before the measurements could begin. The first step in all measurements of biological samples was to incorporate the glass blade placed on the resonator's surface. Next, the resonator was installed inside the Plexiglas framework.

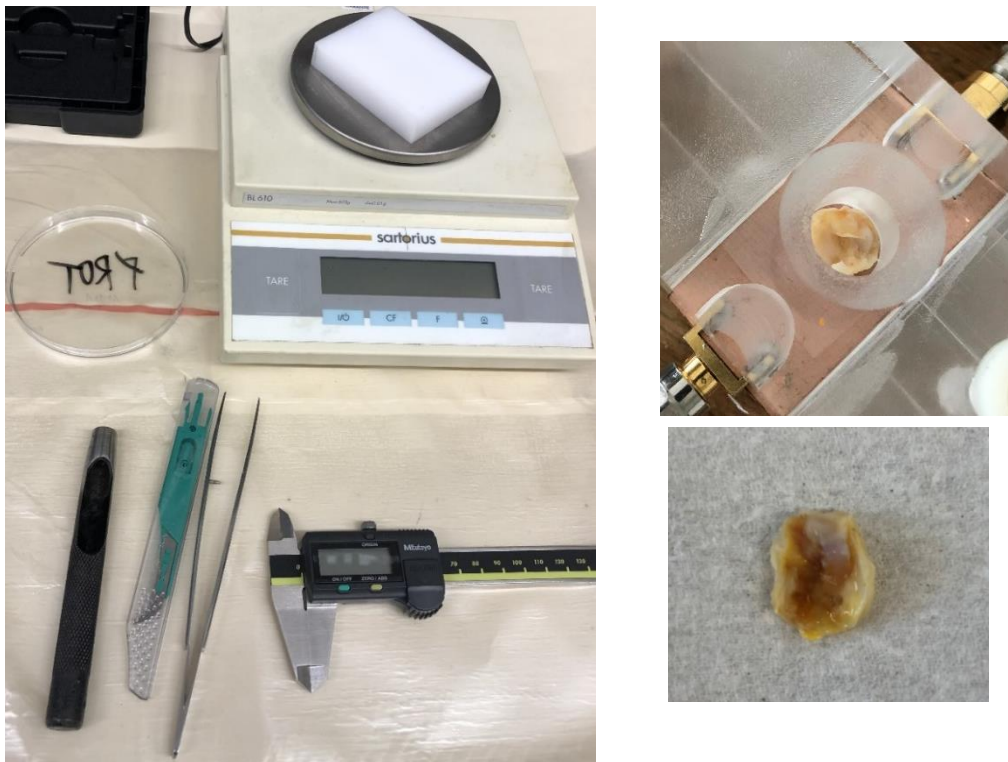


Figure 44. The scale, calliper and cutter used to prepare the carotid plaque samples before insertion in the Plexiglas structure

The carotid atherosclerotic plaques extracted were tested within a week of the CEA. They were carefully removed from the physiological serum and cut into a 1 cm diameter circle. Measurements of the plaques' weights and thicknesses were then performed; the thickness was measured using a Calliper (Fig.44). The carotid plaque was then placed on the glass layer covering the resonator, and the top part of the Plexiglas was locked in place. To prevent air from getting in the way of the electrical contact between the glass cover of the resonator and

the round plaque inside, i.e. the air gap effect, a piston made out of Teflon was placed over the plaque once it was put. The previously reported planar microwave resonators sometimes did not take into account the effect of an air gap between the sample being tested and the resonator, which negatively impacted the results. To solve this issue, several studies used clampers to lock the MUT and lessen the effect of air gaps during the measurements [185], [194], [195].

A group of *Polytech Sorbonne* engineering students that I chaperoned at the start of my PhD manufactured a pressure sensor with a screen that can apply specific pressure to the piston. The purpose was to secure the contact of the entire irregular surface of the plaque without squeezing the plaque (Fig.45 & Fig.46). The samples were first measured without pressure from this sensor and then with controlled pressure. This system experienced problems and was not applying the correct pressure; therefore, it was replaced with metal weights. 300 g metal weights were applied to the piston. This technique was less time-consuming and easier to use. However, it was not ideal; therefore, the following year, another group worked on an improved form of sensor that is still a work in progress; by my colleague Mrs Masini.

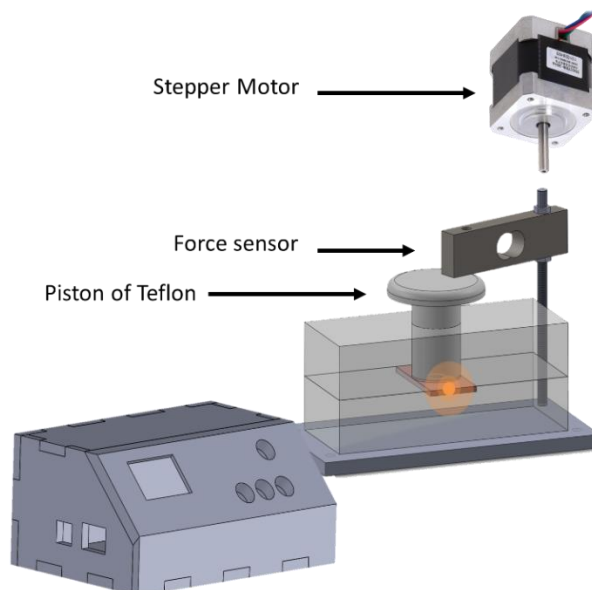


Figure 45. The pressure sensor prototype developed by Polytech Sorbonne engineering students.

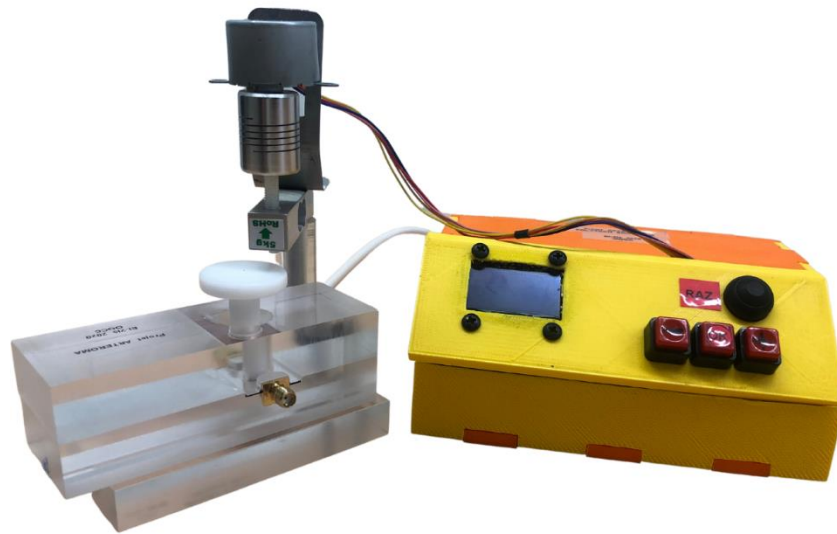


Figure 46. The pressure sensor with its box printed by a 3D printer and the Plexiglas structure with a resonator inside locked in and covered with the piston

Simulations using HFSS were conducted, and the constant dielectric values of each sample were extracted by comparison with the frequency obtained from the simulation of the ideal virtual material, i.e., mimicking samples, and depending on the frequency shift of the measurements and the dielectric losses while considering the sample's thickness. The plaques included in the study varied in thickness from 1.1 mm to 5.7 mm. The average thickness was 2.8 mm. An example of the HFSS results of two different plaques can be seen in Figure 47 & Figure 48. The plaque in Figure 47 was relatively soft upon analysis, while the plaque analysed in Figure 48 was hard and difficult to apply pressure to. Excellent agreement was observed in the frequency shift and width of the curve between simulation results and experimental data with all samples.

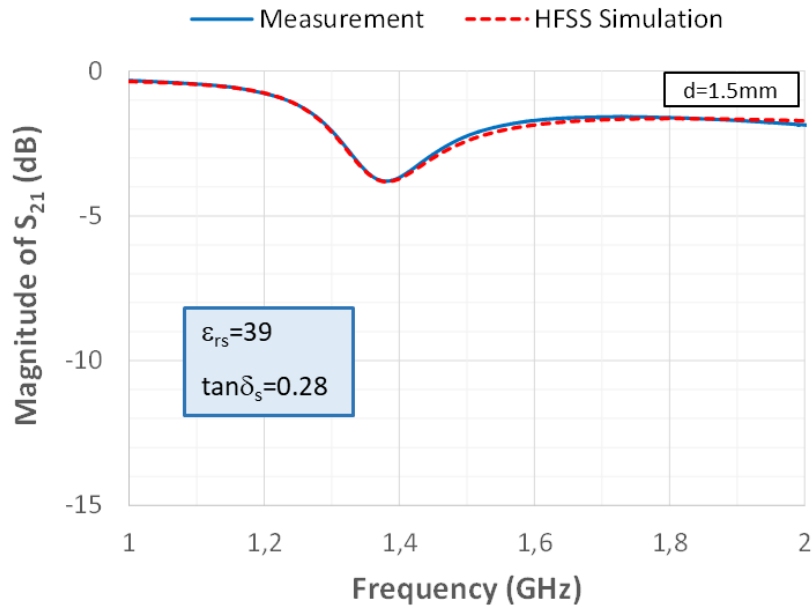


Figure 47. Measurement and simulation results of a soft plaque (d is the thickness of the plaque). The calculated permittivity and tangent loss values are in the blue box.

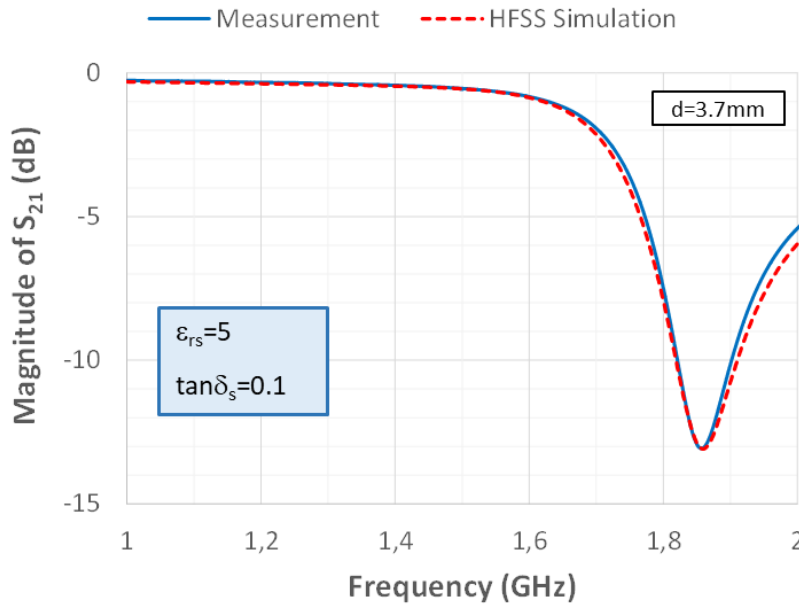


Figure 48. Measurement and simulation results of a hard plaque (d is the thickness of the plaque). The calculated permittivity and tangent loss values are in the blue box.

As the medical analysis (imaging and histology) of all plaques was completed a while later, the plaques were initially divided into two categories based on each patient's medical profile. They were divided into symptomatic and asymptomatic patient groups.

In Figure 49, eleven symptomatic patients' plaques were inserted in HFSS and had an average Δf of 465 MHz from the base measurement of the resonator empty in the Plexiglas structure with the glass layer (2.11 GHz, $|S_{21}| = -21.5$ dB). The highest Δf observed in this group was 826 MHz, and the lowest was 208 MHz. Similarly, in Figure 50, thirty-two asymptomatic patients' plaques were analysed together and had an average Δf of 505 MHz. The highest Δf observed in this group was 780 MHz, and the lowest was 232 MHz.

Those results were encouraging despite not being statistically significant, and the simple fact that the frequency shift is higher in the symptomatic group corresponds well with our theory that symptomatic vulnerable plaques ought to have a higher frequency shift and, consequently, a higher dielectric constant as they are softer, have less calcification, and are likely to have IPH.

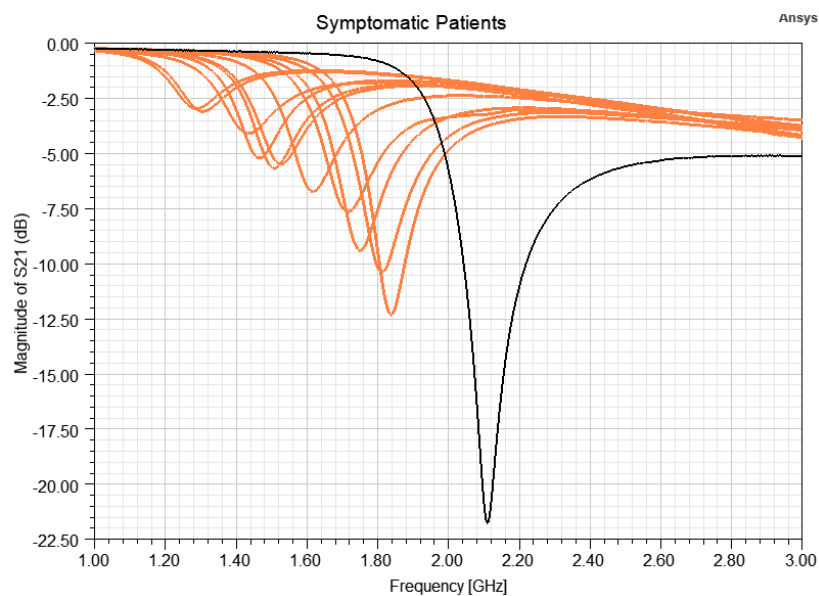


Figure 49. Average $\Delta f = 465$ MHz in the symptomatic group (curve in black is the measurement of the resonator empty with the glass layer and the Plexiglas structure)

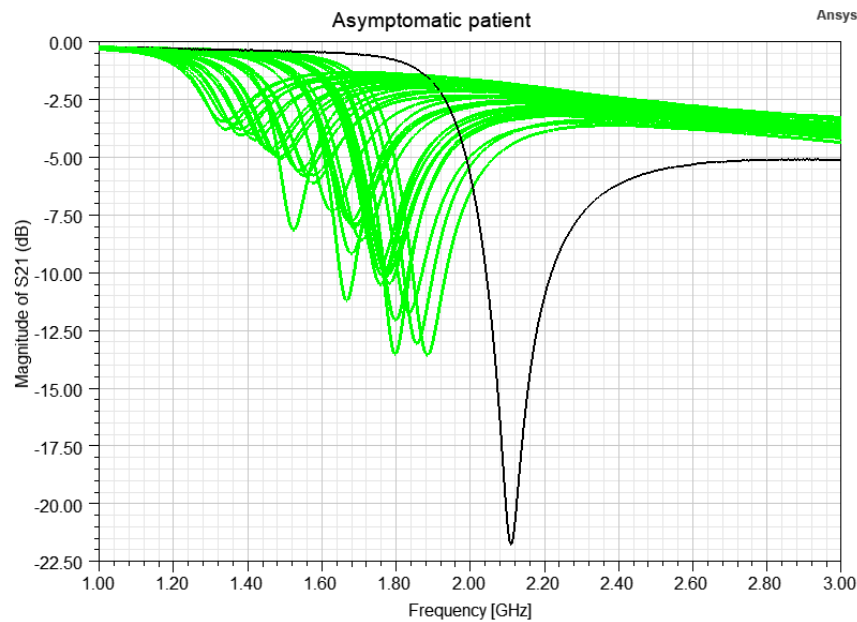


Figure 50. Average $\Delta f = 505$ MHz in the asymptomatic group (curve in black is the measurement of the resonator empty with the glass layer and the Plexiglas structure).

As my research progressed, I grasped the significance of the time of excision, temperature and humidity on the sample and the surrounding environment's influence on the reproducibility of the results. Most notably, the discrepancies in measurements that may have resulted from the physiological serum being entrapped inside the plaque.

In a study by [119], the time between excision and measurements was between 5 min to 5 h, and the tissue temperature was frequently equilibrated to room temperature by the time the dielectric spectroscopy observations were performed. They stated that with time increase between tissue excision and measurement, both the dielectric constant and effective conductivity decrease.

At 5 GHz, for instance, the median dielectric constant for adipose samples characterized 0–50 minutes after excision was approximately 6, while the median dielectric constant for samples defined 250–300 minutes after excision was around 4. This tendency, however, was not detected in the other two groups of adipose-defined tissues with higher water levels. Prior investigations indicate that extracellular water is more prevalent. It is believed that if the majority of the water in adipose tissue is extracellular, it will be lost to desiccation more rapidly than the intracellular water held within the cellular membranes of non-adipose tissues.

As a result, the room and sample temperatures were continuously monitored and, whenever feasible, examined the samples two hours after the procedure, i.e., they were not conserved in a physiological serum. As [158] indicated, immersing the samples in water is not ideal as it might alter the dielectric characteristics.

An infrared thermometer was used to measure the temperature of the sample. Seven carotid plaque samples were measured in these conditions. The room temperature ranged from 19°C to 22°C, while the samples were always at 22°C.

4.8. Conclusion

In conclusion, this chapter has presented a detailed summary of the samples collected in this study, which are statistically analysed in the next chapter. By carefully collecting and characterising these samples, different markers of the carotid plaque vulnerability can be understood better to identify the best indicators for diagnostic and therapeutic interventions. In Chapter 5, the results of the methods presented in this chapter will be explored, allowing for a comprehensive analysis of the data and an accurate interpretation of the results. Overall, the samples collected in this study represent a valuable resource for further research in the field of carotid artery disease and may contribute to the development of new and more effective diagnostic methods.

Chapter V: The Outcomes of Experiments Conducted on Atheromatous Carotid Plaques

Occasionally published studies employ a combination of techniques to distinguish carotid plaques. Even though most studies only contrast two types of imaging against histology. In this thesis, a longitudinal, multimodal examination of carotid plaques using DUS, CT, visual score, histology, and clinical symptoms was conducted. The goal was to study the microwave sensor's ability to differentiate risky and stable plaques and to statistically correlate its sensitivity and sensibility with histology, the gold standard, and the currently used radiological modalities. In addition, to establish an accurate benchmark against which all the approaches could be evaluated.

The results of the methods displayed in the previous chapters will be presented and discussed in this chapter. A complete analysis of the study's carotid atherosclerotic plaques is demonstrated and compared. The findings are interpreted in light of previous research, and the perks and drawbacks of the methods and results are covered. Constraints on the scope of the thesis are discussed.

5.1. Statistical Comparison of Imaging and Histopathological Techniques for the Evaluation of Carotid Artery Disease

Fifty plaques of forty-nine patients were included in this study; 35 had no TIA and/or stroke symptoms in the two months before the operation; therefore, they were considered asymptomatic. The mean age was 73 years old, with a majority of male patients (72%). Other demographics and cardiovascular comorbidities are detailed in Table 9.

Thirty-one patients out of the 49 had Best Medical Therapy (BMT) (1 or 2 antiplatelet drugs, statin, and antihypertensive drugs). The surgical site was on the right side in half of the cases. The median length of hospitalisation was three days. Only one post-operative TIA was observed during the hospitalisation period; however, no stroke nor significant adverse cardiovascular events were observed in the rest of the patients. There was no postoperative death. Four patients

had hematomas at the site of the surgery. Twenty-two patients had DUS before leaving the hospital, and they were all normal.

Table 9. Demographics and cardiovascular comorbidities

	Total n=50 (%)	Asymptomatic n=35 (%)	Symptomatic n=15 (%)
Total number of plaques	50 (100%)	35 (70%)	15 (30%)
Mean age	73.02 (8,8)	73,62	72,41
Body Mass Index (BMI)	25.1 (3.4)		
Female	14 (28%)	11 (31%)	3 (20%)
Arterial Hypertension	37 (74%)	26 (74%)	11 (73%)
Active smoker	8 (16%)	6 (17%)	2 (13%)
Previous smoker	18 (36%)	11 (31%)	7 (47%)
Diabetes	13 (26%)	7 (20%)	6 (40%)
Dyslipidaemia	31 (62%)	21 (60%)	10 (67%)
Obesity	3 (6%)	3 (9%)	0
Cardiovascular Disease (CVD)	23 (46%)	16 (46%)	7 (47%)
Peripheral Arterial Disease (PAD)	12 (24%)	9 (26%)	3 (20%)
History of stroke/TIA	19 (38%)	9 (26%)	10 (67%)
Antiplatelet drug (antiagregant)	35 (70%)	28 (80%)	7 (47%)
Vitamin K Antagonists (VKA)	1 (2%)	1 (3%)	0
Novel Oral Anticoagulant (NOAC)	3 (6%)	2 (6%)	1 (7%)
2 Antiplatelet drugs	9 (18%)	7 (20%)	2 (13%)
Beta-blockers	22 (44%)	15 (43%)	7 (47%)
Statin	43 (86%)	32 (91%)	11 (73%)
Diuretics	9 (18%)	7 (20%)	2 (13%)
Angiotensin II receptor blockers (ARBs)	16 (32%)	11 (31%)	5 (33%)
Angiotensin-converting enzyme (ACE)	18 (36%)	16 (46%)	2 (13%)
Calcium channel blockers (CCB)	22 (44%)	16 (46%)	6 (40%)

Histology was considered the gold standard for identifying Vulnerable Plaques (VP). Plaques were considered VP when they contained more than 35% Lipid Rich Necrotic Core (LRNC), which is the average of the proposed cut-offs by [57], which is 30% and 40% by [196]. 22 VPs were consequently identified. 46% of the VPs had caused symptoms in the patients. Most stable plaques did not cause any symptoms (Table 10).

Concerning risk factors, no statistically significant relationship was found between smoking and symptoms or plaque vulnerability nor with the other co-morbidities (Table 11).

Table 10. The number of histologically based VP and NVP in the symptomatic and asymptomatic group

	Vulnerable n=22	Non-Vulnerable n=28	p-value
Symptomatic vs Asymptomatic			0.035
Symptomatic n=15	10 (46%)	5 (18%)	
Asymptomatic n=35	12 (54%)	23 (82%)	

A p-value less than 0.05 (typically ≤ 0.05) is statistically significant. 60% of the symptomatic patients were on BMT, and none were obese. Only 20% of the symptomatic patients had PAD who were all diabetics.

Table 11. Risk factors and comorbidities in the vulnerable vs stable group

	Vulnerable n=22	NVP n=28	p-value
Sex			0.462
Female	5 (23%)	9 (32%)	
Arterial Hypertension	17 (77%)	21 (75%)	0.669
Smoking			0.333
Active	2 (9%)	6 (21%)	
Previous smoker	10 (46%)	8 (29%)	
Diabetes	4 (18%)	9 (32%)	0.264
Dyslipidaemia	15 (68%)	16 (57%)	0.425

Quantitatively, these VPs had a large content of LRNC (45%), a low amount of calcification (3%) and fibrous cap (42%) as opposed to Non-Vulnerable Plaques (NVP), which were less lipidic-necrotic (9%), more calcified (13%) and fibrotic (65%) ($p < 0.05$). Consistently, NVP were more frequently asymptomatic (82%) lesions ($p < 0.035$) (Table.12).

Table 12. Composition of the plaques in the VP vs NVP group and symptomatic vs asymptomatic group

	All	Vulnerable	Stable	p-value	Symptomatic	Asymptomatic	p-value
	Mean \pm SD	Mean \pm SD	Mean \pm SD		Mean \pm SD	Mean \pm SD	
Fibrosis %	55.1 \pm 17	41.9 \pm 11	65.4 \pm 15	0.000	47.5 \pm 13	58.3 \pm 18	0.043
LRNC%	25.3 \pm 21	45.7 \pm 11	9.3 \pm 9	0.000	32.2 \pm 20	22.4 \pm 20	0.133
Calcification%	8.5 \pm 12	3.0 \pm 3	12.8 \pm 15	0.010	12.5 \pm 15	6.8 \pm 10	0.074

Six patients only were found with Intraplaque Haemorrhage (IPH). Four out of these six plaques had caused symptoms. Three of them were VPs (Fig.51).

Osteoid Metaplasia (OM), i.e., ectopic bone tissue, has been identified undoubtedly in the histology slide in only one plaque out of the 50 (Fig.52). This patient was asymptomatic and had an NVP with 37% calcification levels.

Besides, the plaques underwent a visual surgical assessment. The questionnaire results were examined against all other modalities, including histology, and no correlation was found with any other modality.

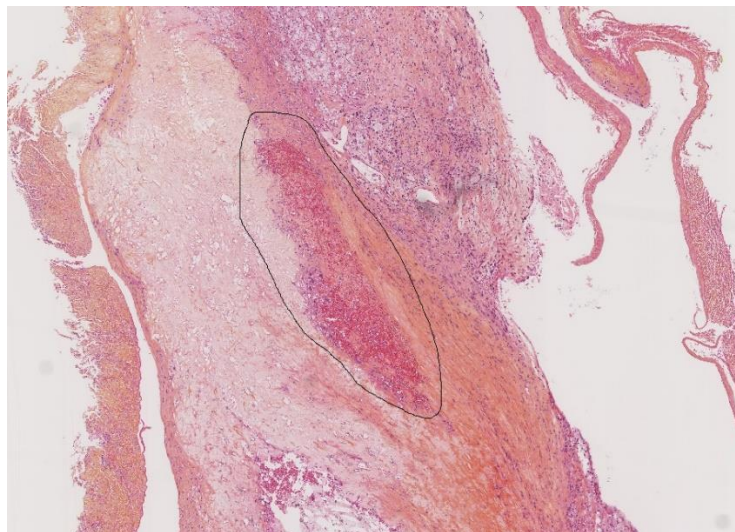


Figure 51. IPH bordered in black.

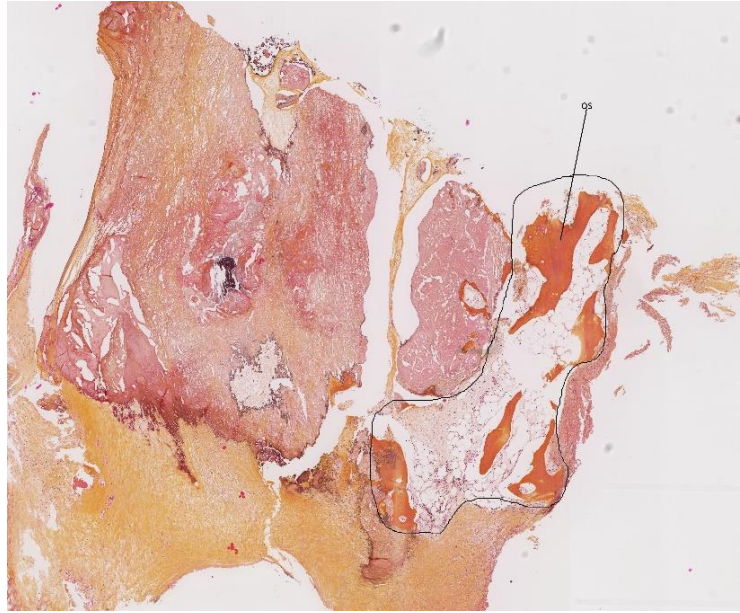


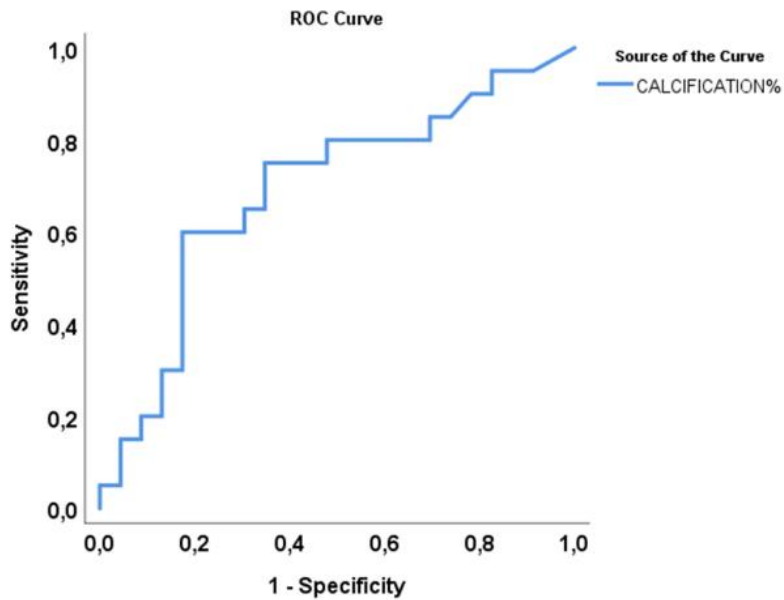
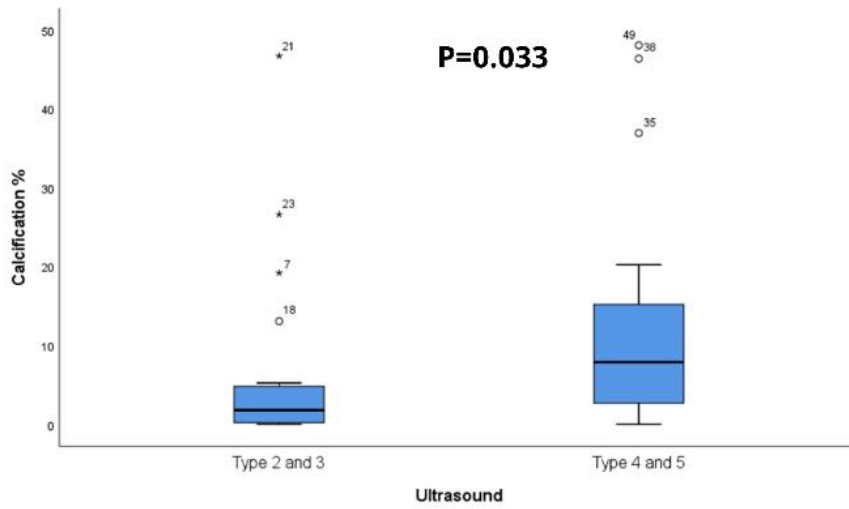
Figure 52. OM region encircled in black.

5.1.1 DUS vs Histology results

In the first imaging modality used for carotid stenosis, i.e. DUS, no patient was identified with type 1 of the Gray-Weale classification, i.e. uniformly echolucent. For the statistical analysis, types 2 and 3 were compared against 4 and 5.

DUS analysis showed that 78% of VPs were type 2&3 plaques as opposed to NVPs, that mainly were type 4&5 plaques. Correspondingly, the amount of LRNC significantly decreased ($p=0.010$), and the amount of calcification significantly increased ($p=0.033$) from type 2 to type 5 lesions (Fig.53&Fig.54). No significant relation was observed between fibrous cap levels in histology and Gray-Weale classification groups. In addition, diabetes levels were significantly higher in the type 4&5 group ($p=0.043$) compared to group 2&3.

The Receiver Operator Characteristic (ROC) curve illustrates the compromise between sensitivity and specificity. Classifiers that produce curves closest to the upper-left corner perform better. A random classifier is anticipated to produce points along the diagonal as a baseline. The less accurate the measurement, the closer the curve is to the 45-degree diagonal of the ROC space [197].



Test Result Variable(s)	Area	Std. Error ^a	Asymptotic 95% Confidence Interval		Asymptotic Sig.
			Lower Bound	Upper Bound	
CALCIFICATION%	0.690	0.084	0.526	0.854	0.023

Cutoff 4.21, Sensitivity = 65%, Specificity = 70%

Figure 53. Statistical analysis of Gray-Weale classification vs calcification levels in histology

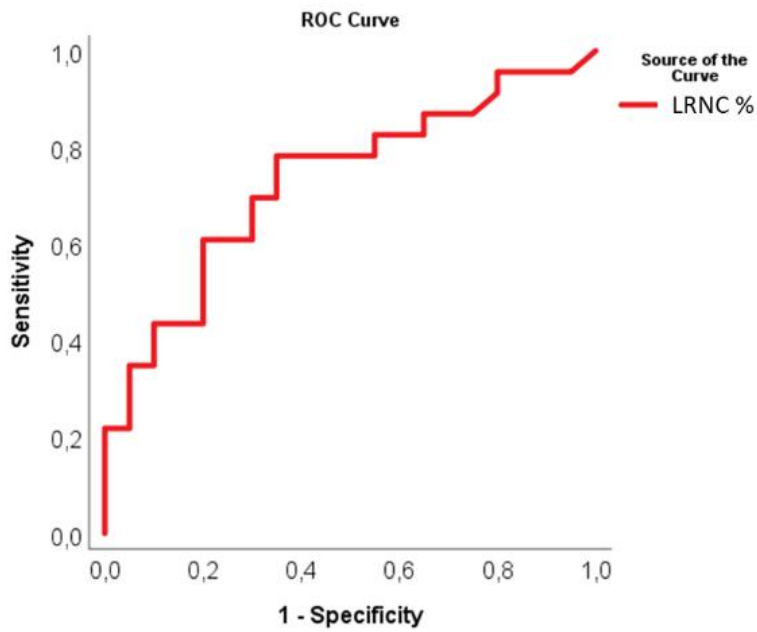
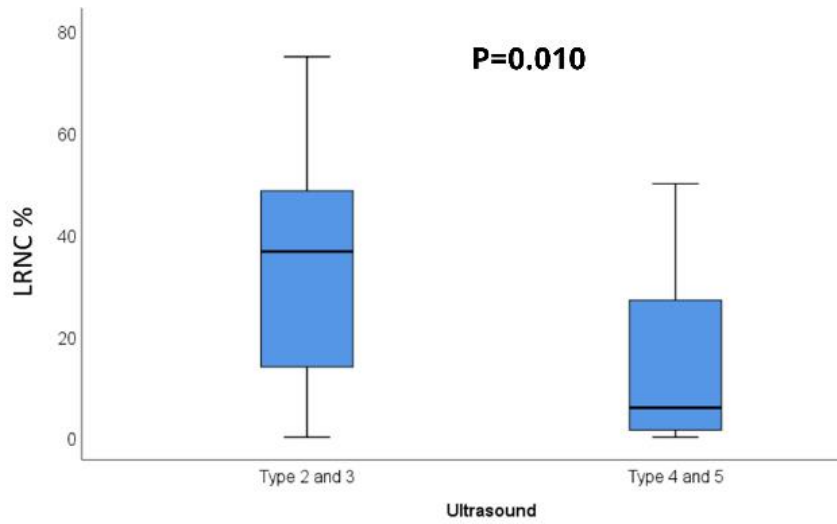
The area under the curve (AUC) in a ROC curve represents the measure of the overall performance of a binary classification model. It measures the degree of separability between the model's true positive rate (sensitivity) and false positive rate (1-specificity) over all possible discrimination thresholds. A perfect classifier would have an AUC of 1.0, while a random guess would have an AUC of 0.5. Generally, a higher AUC indicates better predictive performance of the model.

The results from each patient were used to plot the ROC curves presented in this chapter. The ROC analysis here showed that a cut-off of 17% of LRNC (sensitivity: 70%, specificity: 70%, $p=0.003$) and 4.2% of calcification (sensitivity: 65%, specificity: 70%, $p=0.023$) distinguished type 2&3 from type 4&5 plaques (Fig.53&Fig.54). Therefore, LRNC and calcification predicts the ultrasound group 2&3 vs 4&5 of DUS, in other words, the two groups (2&3, 4&5) of DUS can forecast the vulnerability of the plaque. This implies that clinicians could potentially use ultrasound imaging to identify which group a plaque belongs to and, based on that information, predict the risk of plaque vulnerability.

An Asymptotic Confidence Interval is a statistical interval that provides a range of plausible values for an unknown population parameter based on a sample from that population. It is called "asymptotic" because it is based on the assumption that the sample size is large enough to approximate the distribution of the sample mean or proportion as a normal distribution.

In other words, as the sample size increases, the sampling distribution approaches a normal distribution, allowing for the population parameter estimation with greater accuracy. An asymptotic confidence interval provides an estimated range of values for the population parameter that is likely to contain the true parameter value with a certain level of confidence based on the properties of the sampling distribution. The confidence level indicates the probability that the true population parameter falls within the interval. For example, a 95% asymptotic confidence interval indicates that there is a 95% probability that the true population parameter lies within the range of values provided by the interval [198].

The reported asymptotic confidence intervals provide a range of plausible values for the true population parameters of LRNC and calcification. The lower and upper bounds for calcification were 0.526 and 0.854, respectively, suggesting that the true population value of calcification is likely to fall between these values with a 95% confidence.



Test Result Variable(s)	Area	Std. Error ^a	Asymptotic 95% Confidence Interval		Asymptotic Sig. ^b
			Lower Bound	Upper Bound	
LRNC%	0.730	0.077	0.579	0.882	0.003

Cutoff 17.19, Sensitivity = 70%, Specificity = 70%

Figure 54. Statistical analysis of Gray-Weale classification vs LRNC levels in histology

The reported asymptotic p-value of 0.023 indicates that the association between calcification and ultrasound groups is statistically significant (Fig.53).

For LRNC, the lower and upper bounds of the asymptotic confidence interval were 0.579 and 0.882, respectively. This suggests that the true population value of LRNC is likely to fall between these two values with a 95% confidence. The reported asymptotic p-value of 0.003 indicates that the association between LRNC and the ultrasound echogenicity groups is statistically significant (Fig.54).

Regarding plaque surface characteristics, no correlation or association was observed with symptoms, plaque vulnerability, or ulceration in CT.

Although documented, complete velocity analysis is not presented here as it is not the goal of this research; however, it was interesting to note that 28% of the included patients in this study had < 69% stenosis on DUS. Of these patients, three patients were symptomatic but did not have VPs, and three others who had VPs in the histological analysis did not have symptoms at the time of the operation.

5.1.2 CT vs Histology & DUS results

The CT-scan statistical analysis found no significant difference in terms of Hounsfield Unit (HU) pattern between symptomatic and asymptomatic plaques, nor between VP and NVP (Table.13). In contrast, type 2&3 plaques in DUS had significantly more HU<60 and significantly more HU between 60 - 130 than type 4&5 plaques (p=0.035 and p=0.038, respectively) (Fig.55&Fig.56).

Table 13. HU components and PVFA in the VP vs NVP group and symptomatic vs asymptomatic group (SD= standard deviation).

	All	Vulnerable	Stable	p-value	Sympto	Asympto	p-value
	Mean ± SD	Mean ± SD	Mean ± SD		Mean ± SD	Mean ± SD	
<60HU%	17.9 ± 15	22.2 ± 16	14.7 ± 13	0.093	17.6 ± 14	18.1 ± 15	0.911
60 - 130HU%	25.9 ± 18	30.6 ± 18	22.5 ± 18	0.170	29.6 ± 17	24.5 ± 18	0.409
>130HU %	31.4 ± 24	32.9 ± 22	30.3 ± 26	0.722	37.9 ± 24	28.8 ± 24	0.229
PVFA	-54.3±35	-63.9 ± 25	-45.1 ± 40	0.081	-54.6 ± 27	-54.1 ± 37	0.770

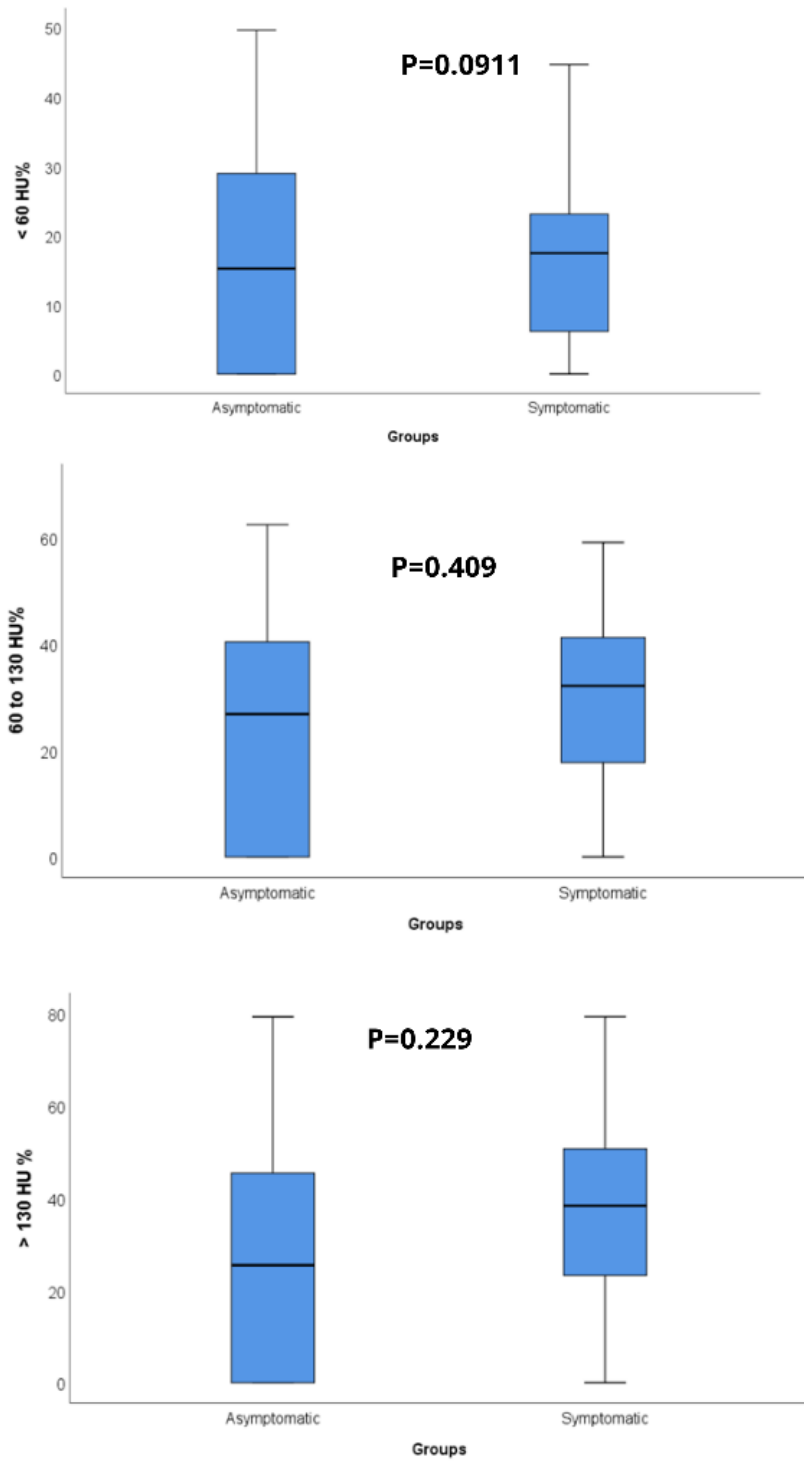


Figure 55. Box plot (whisker chart) analysis of HU groups vs symptoms

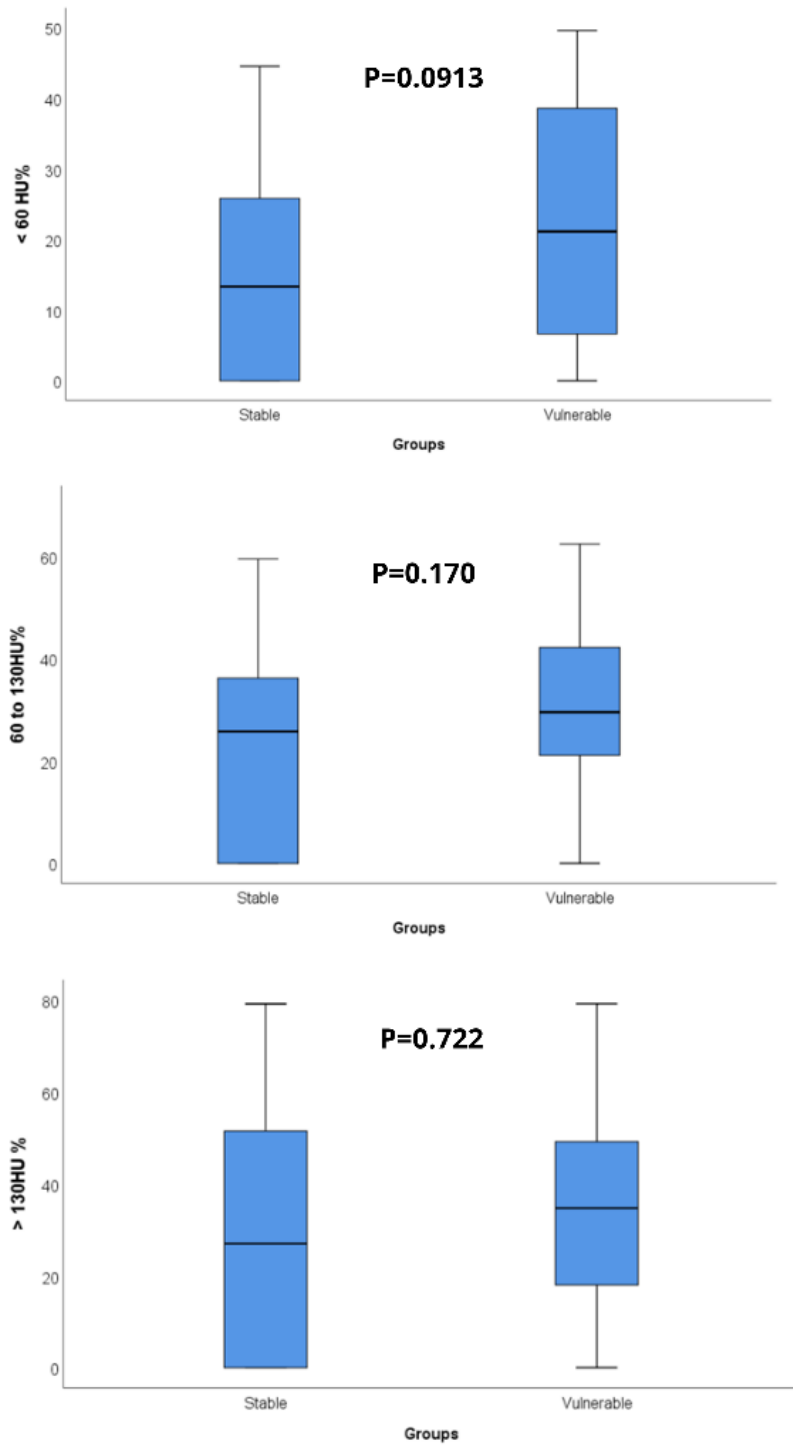


Figure 56. Box plot (whisker chart) analysis of HU groups vs VP&NVP, i.e. stable group

The significance of Peripheral Vascular Fat Attenuation (PVFA) was also investigated. PVFA was found lower in patients with VPs than in patients with NVPs, i.e. stable plaques, but the relationship was not statistically significant, and the values were almost identical in symptomatic and asymptomatic patients. Therefore, PVFA was not significant in any comparison. PVFA values were not significantly different between symptomatic, asymptomatic, VP, and NVP and between DUS type 2&3 and type 4&5 plaques (Fig.57). Moreover, ulceration detected on CT scans of the operated and control sides showed no correlation or association with symptoms. However, 62% of the VPs had ulceration on CT scan.

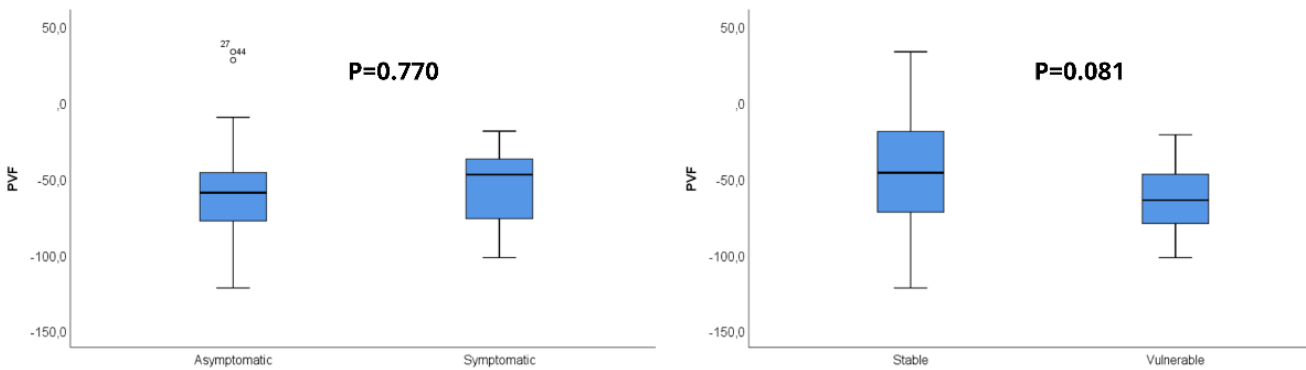


Figure 57. Box plot analysis of the PVFA vs symptoms and VP & NVP groups.

CTA is often performed in conjunction with DUS to characterise carotid plaques before surgery. When correlating DUS with CT scan, a significant relationship was observed between the Gray-Weale classification and the % HU < 60 and % HU 60-120 (Fig.58). Furthermore, 83% of the plaques in types 2 and 3 in DUS had ulceration on CT (p=0.0002).

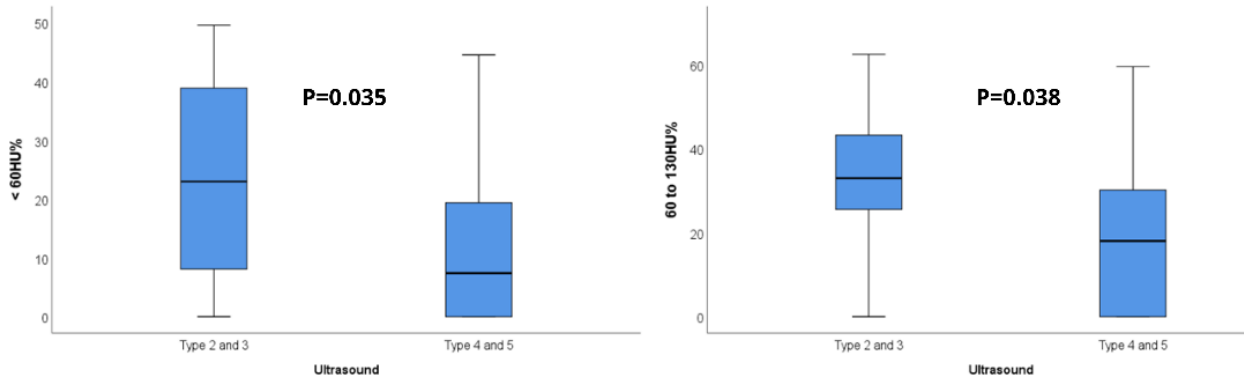


Figure 58. Box plot analysis of HU groups vs Gray-Weale groups in DUS

5.1.3. Microwave CSRR biosensor vs Histology and radiological imaging modalities

Samples had various frequency shifts and curve wideness. As expected, the dielectric constant ϵ_r differed according to the composition of the plaque and in a less manner with the thickness of the sample, which was partially controlled by the pressure applied. This was observed by considering the minimum frequency of the amplitude of the transmission coefficient $|S_{21}|$ parameter, which shifted towards lower frequencies as ϵ_r increased.

Table 14. Statistical analysis of the dielectric constant in the different groups of patients

	All	VP	NVP	p-value	Symptomatic	Asymptomatic	p-value
	Mean \pm SD	Mean \pm SD	Mean \pm SD		Mean \pm SD	Mean \pm SD	
ϵ_r	18.7 \pm 12	17.6 \pm 11	19.5 \pm 13	0.850	20.8 \pm 14	17.9 \pm 11	0.684

The dielectric constant was higher in symptomatic patients, as expected. However, it was lower in VPs (Table.14) (Fig.59). Nevertheless, a statistically significant relationship was observed when compared with the DUS echogenicity groups.

The dielectric constant significantly decreased from DUS type 2 to type 5 plaques ($p= 0.004$). ROC curve analysis showed a good dielectric constant (AUC: 0.761) ability to predict the groups of DUS the plaques belong to (cut-off value: 18.75, sensitivity: 73%, sensibility: 80%, $p= 0.001$, Figure 60). For the dielectric constant, the lower and upper bounds of the asymptotic confidence interval were 0.613 and 0.910, respectively. This suggests that the true population value of ϵ_r is likely to fall between these two values with a 95% confidence. The reported

asymptotic p-value of 0.001 indicates that the association between ϵ_r and the ultrasound heterogeneity groups is statistically significant (Fig.60).

No correlation was observed between CT results and the dielectric constant values.

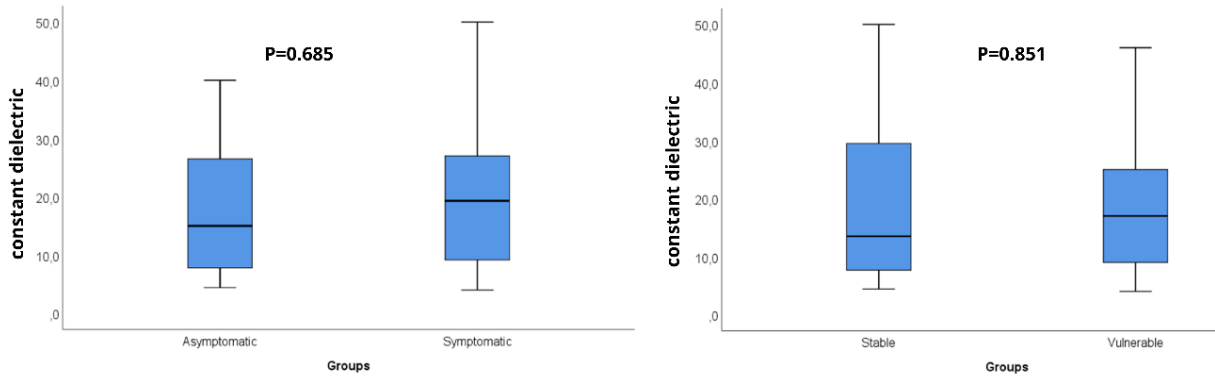
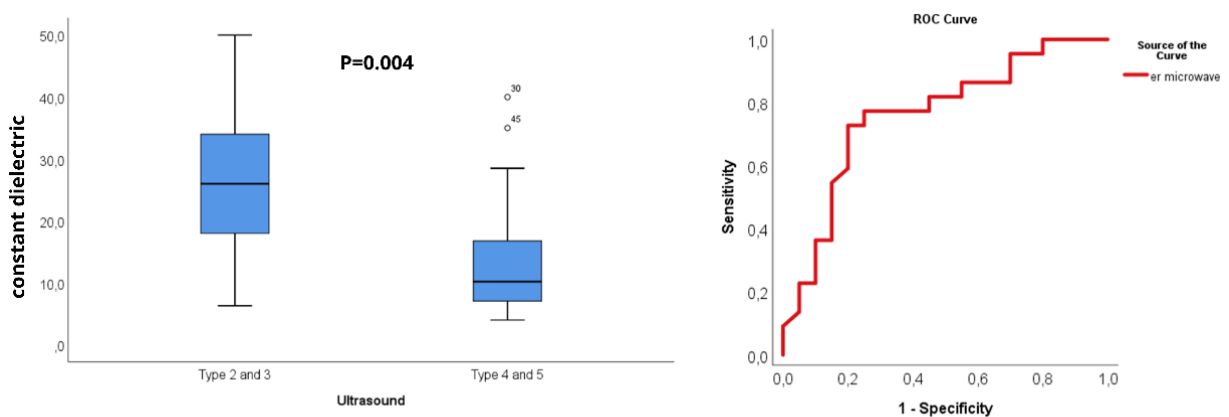


Figure 59. Whisker chart of the dielectric constant vs symptoms, VP and NVP groups



Test Result Variable(s)	Area	Std. Error ^a	Asymptotic 95% Confidence Interval		Asymptotic Sig. ^b
			Lower Bound	Upper Bound	
constant dielectric	0.761	0.076	0.613	0.910	0.001

Cutoff 18.75, Sensitivity = 73%, Specificity = 80%

Figure 60. Whisker chart and ROC curve statistical analysis of the dielectric constant vs DUS echogenicity types.

5.2 Multivariate analysis and multimodel prognostic score to predict VPs

Multivariate analysis refers to statistical methods and techniques that simultaneously analyse data involving multiple variables. It is used to understand the relationships between multiple variables and how they affect each other. In contrast to univariate analysis, which focuses on one variable at a time, multivariate analysis examines multiple variables to determine how they are related and interact. The multivariate analysis evaluates multiple variables (more than two) to identify any possible association among them [198].

A multimodel prognostic score is a statistical method that combines multiple individual prognostic models to provide a more accurate prediction of a clinical outcome, typically using a weighted average or algorithm. It is used to improve the accuracy and reliability of the prediction by incorporating a broader range of factors that may influence the outcome and taking into account the strengths and weaknesses of different models. The goal is to provide a more comprehensive and reliable prediction of the clinical outcome of interest.

Table 15. Multivariate analysis to predict VP.

Variables	OR	95% C.I. for OR		Sig.
		Lower	Upper	
Dielectric constant	0.940	0.856	0.993	0.047
Gray-Weale classification 2&3 or 4&5	0.035	0.003	0.410	0.008

Multivariate analysis showed that the dielectric constant ($p=0.047$) and Gray-Weale classification groups (2&3 – 3&4) ($p=0.008$) were predictive characteristics of VP (Table.15). In multivariate analysis, "OR" typically refers to the "odds ratio," which is a measure of association between an exposure and an outcome. The OR is the ratio of the odds of the outcome occurring in the exposed group compared to the unexposed group. An odds ratio greater than 1 indicates that the exposure is associated with an increased odds of the outcome, while an odds ratio less than 1 indicates that the exposure is associated with a decreased odds of the outcome. An odds ratio of 1 indicates that there is no association between the exposure and the outcome. The 95% confidence interval (CI) is used to calculate the OR's precision. A big CI implies that

the OR has a low level of precision, whereas a small CI suggests that the OR has a better level of precision [199].

Based on the coefficients of these variables, a multimodal prognostic score was able to significantly predict the presence of a VP (cut-off value: -4.5, AUC: 0.800, sensitivity: 77%, specificity: 70%, $p < 0.0004$, Figure 61). The AUC's lower and upper bounds of the confidence interval are 0.65 and 0.93, respectively (Fig.61). This means that there is a 95% probability that the true AUC for the population falls between these values. Since the lower bound is greater than 0.5, we can be confident that the model is statistically better than random chance. Finally, the p-value of 0.0004 indicates that the difference between the observed AUC and a hypothetical AUC of 0.5 (random chance) is statistically significant at the 0.05 level. In other words, the probability of observing an AUC of 0.8 or higher by chance alone is less than 0.004, assuming that the model has no discriminatory ability. Therefore, it can be concluded that the model has a significant predictive ability for the outcome of interest.

It is then established that Microwave and DUS are more predictive of the Vulnerable group than others using the following Multimodel score formula:

$$1.760 + (-0.062 \times \epsilon_r) + (-3.367 \times \text{Gray-Weale classification 2\&3 or 4\&5}) \quad (17)$$

The cut-off is calculated using this formula; therefore, any value above -4.5 is VP, and less than -4.50 is NVP. Consequently, patients with a multimodel score between -4 to -4.5 would need further examination, and they are considered vulnerable until proven stable with further assessment.

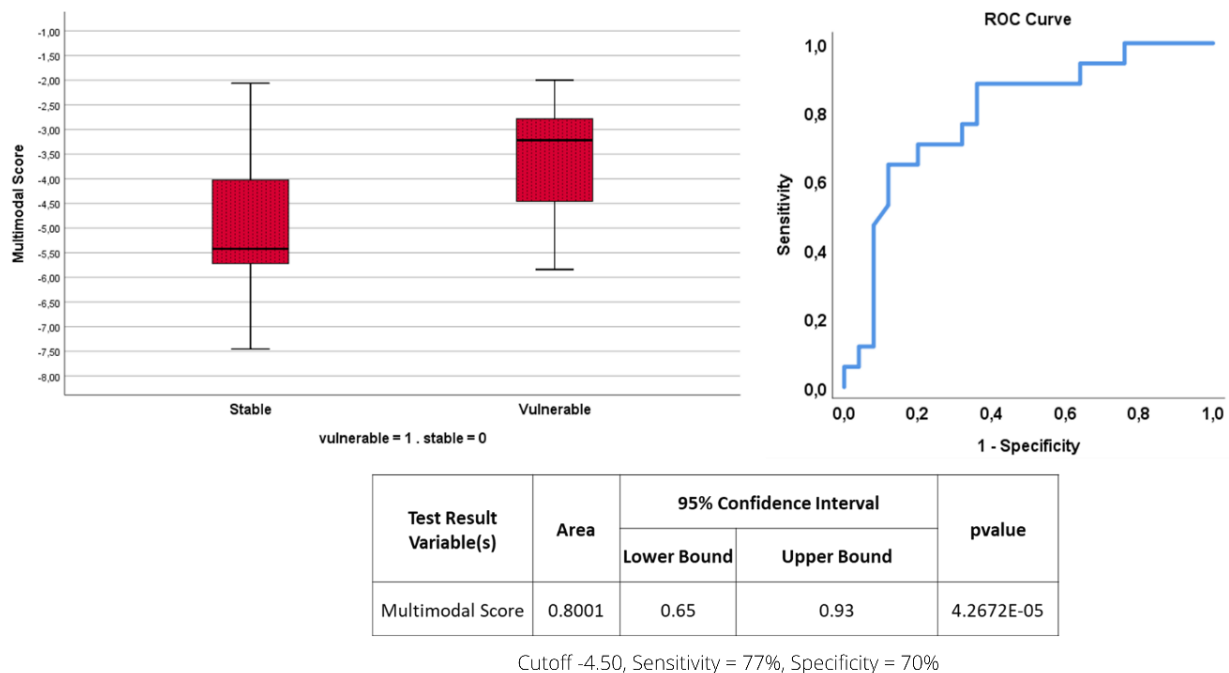


Figure 61. Multimodal prognostic score to predict better the vulnerability of carotid plaques.

5.3. Interpretation of the results in light of previous research

Two distinct clinical patterns of carotid lesions were detected. The first was defined by type 2&3 lesions in DUS according to Gray-Weale classification, which were more frequently symptomatic plaques with slightly higher dielectric constant values in microwave analysis. Lesions in this group were substantially more likely to be vulnerable in histology. The second group, on the other hand, was distinguished by type 4&5 Gray-Weale lesions that were frequently asymptomatic and had relatively lower dielectric constant values. In histology, this second group exhibited characteristics of a non-vulnerable plaque. Furthermore, an algorithm based on the combination of DUS and microwave imaging was developed that can identify vulnerable plaques with high sensitivity and specificity (Fig.62).

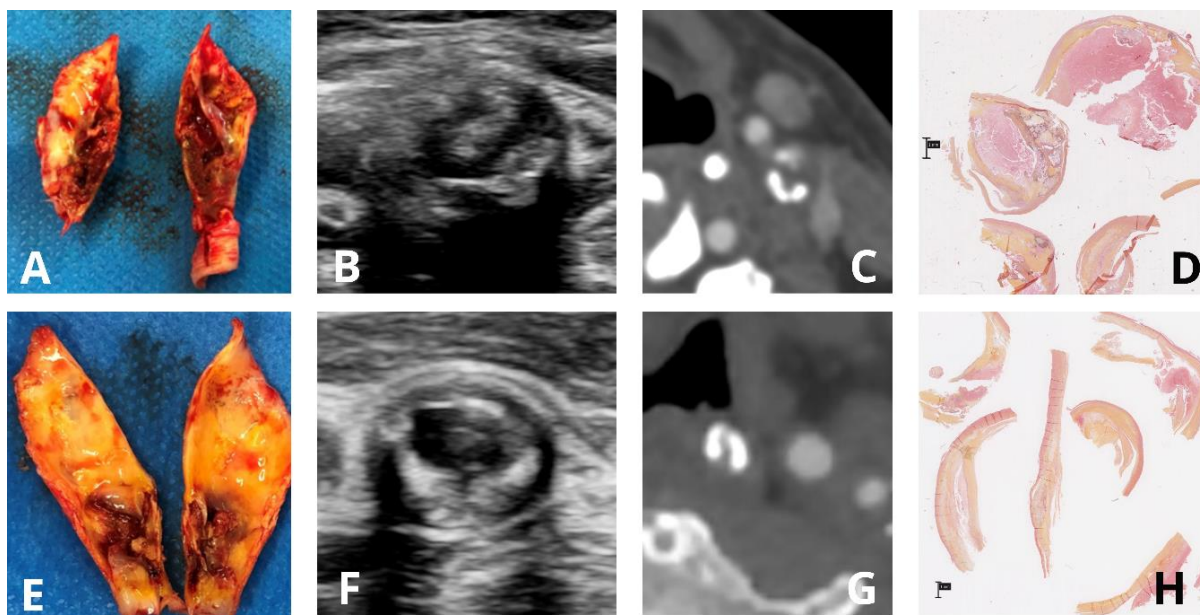


Figure 62. The VP in (A) shows similar findings between the in-vivo examination of DUS and CT (B,C), respectively and the histological analysis in (D). Similarly, the NVP in (E) displays comparable findings between the in-vivo assessment of DUS and CT (F,G), respectively and the histological analysis in (H).

Using DUS, Gray-Weale classification is one of the most prevalent methods for classifying plaques based on their echogenicity [200]. Types 1 and 2 are majority LRNC plaques, 3 and 4 are mixed, and type 5 plaques are calcified [201], [202]. [200] demonstrated a correlation between plaque type and symptoms, which was also observed in this thesis. Nevertheless, and probably due to the small sample size, this study did not find any patient with type one of Gray-weale classification, i.e. purely echolucent plaque. Another study analysed 747 consecutive carotid lesions using the same Gray-Weale approach and classified type 1 and 2 plaques as VP [203]. These findings corroborate our assumption that DUS with Gray-Weale classification is highly effective at diagnosing VPs and that the plaque phenotype is substantially linked with symptomatic clinical presentation. As a result, a more detailed analysis in DUS should be encouraged beyond the degree of stenosis and velocity measurements, and the Gray-Weale classification should be part of the routine Doppler US report. It is observed in this cohort that thresholds of 17% of LRNC and 4% of calcification in histology-characterised VPs were highly correlated with type 2&3 plaques in Doppler US. These values contrast with the 30% or 40% values of LRNC found in previous work [196], [204].

CTA has proven previously to be a reliable method for evaluating carotid plaque ulceration [17], [63]. In our study, ulceration was detected in many VPs however no significant relationship was observed between ulceration and other markers. Furthermore, type 2&3 plaques in DUS had a higher content of <60HU and 60-130 HU material than type 4&5 plaques. CT scan indicates plaque composition with fatty, fibrotic and calcified plaques displaying different values of HU [68], [69]. Fatty plaques are associated with a higher risk of stroke than calcified plaques [47], [48], [64]. The present work adds up to previous studies, and altogether, these data may help better characterize the relationship between histology and routine preoperative modalities, which is critical to improving surgical screening of carotid lesions. The significance of PVFA using CT was also studied. Increased density of PVFA has been suggested to correlate with histopathologic markers of inflammation in coronary plaques, such as inflammatory cytokines and macrophages, and it seems that a significant increase in PVFA is observed in symptomatic compared to asymptomatic carotids [71]–[74], [205].

Two studies have found a substantial rise in PVFA levels between symptomatic and asymptomatic carotids [74], [205]. In addition, they noticed that the levels of PVFA were more prominent on the stenotic carotid side compared to the non-stenotic contralateral side, regardless of symptoms. Notably, this was retrospective research with no histological controls. Here, an opposite pattern was observed with lower PVFA values in symptomatic and VPs as opposed to asymptomatic and NVPs.

Recently, it was discovered that PVFA is substantially linked with IPH (-41 HU vs -56 HU without IPH) ($p=0.001$) [18]. Another team reported similar results [206] but with different values: approximately -48 without IPH and -29 with IPH ($p=0.001$). In this thesis, the plaques with IPH had an average HU of PVFA of -67, while those with no IPH had an average HU of PVFA of -46. Therefore, PVFA was lower in patients with IPH, contrary to the abovementioned studies. Regarding those findings, all previous investigations were retrospective, used different protocol analyses, and had no histopathologic control. PVFA levels vary significantly between studies, restricting comparability.

Overall, the verdicts here suggest that PVFA may be a potential marker to utilise in routine CTA practice to identify inflammatory plaques that are more likely to rupture; however, this needs to be confirmed by a prospective trial and a standardised protocol assessment.

Furthermore, some limitations as the low reproducibility of those kinds of measurements (ROI chosen manually), the relatively small sample size and technical considerations (multiple CTAs with different protocols), may have diminished the statistical significance.

It is important to note that the relationship between symptoms and their cause is less apparent in the carotid arteries than in the coronary ones. While VPs and stable plaques can be identified in both asymptomatic and symptomatic patients, the plaque phenotype at the carotid level does not necessarily represent the symptoms. As a result, a multimodal and longitudinal approach should be favoured to identify accurately plaques that are suitable candidates for CEA.

Several publications have researched the calcification process in carotid lesions. According to recent research, microcalcification accumulates within the fibrous cap of the plaques [150] and appears exceptionally early in the atherosclerotic process, specifically at the plaque shoulder, where it induces mechanical stress that contributes to plaque instability. In contrast, excessive calcification tends to stabilise the structure. This could explain the difference in our results, as calcification was lower in the VP group than in the NVP group. However, it was higher in the symptomatic group against the asymptomatic group. This could mean that the calcification in the symptomatic group was early microcalcification or that the symptoms caused were of another origin apart from the carotid plaque. In addition, only a few patients had IPH or high levels of calcification in histological analysis; this could be attributed to the fact that the plaques were submerged in formol and then cut into a multitude of slides, and only one slide of each plaque was analysed so that some IPH or calcification could have been lost in the process.

From a molecular perspective, OM in one carotid plaque has been identified. This specific form of calcification is strongly linked to asymptomatic, persistent plaques. The fact that the histology slides only show a fragment of the whole plaque may account for our finding of only one patient with OM. Moreover, the plaques were decalcified in the histological analysis before cutting them.

Regarding the surgical observational score, even in the case of experienced surgeons, the data suggested that the visual assessment of carotid plaque is unreliable. Notwithstanding the fact that macroscopic intraoperative examination of the carotid lesion has no preoperative value, these findings are rather insightful.

Histological analysis is frequently used in contemporary dielectric studies to identify the types of tissue present in a given sample and/or confirm abnormal tissue presence [155]. However, the histological radius and depth are not consistently defined in the literature, nor is there a consensus on how these crucial measurements should be made. Therefore, comparing constant dielectric data from different experiments with histology is problematic. This could be why no universal agreement exists between published dielectric measurements of the same tissue types. Those working on medical device development are hampered by the lack of consistency in reported dielectric qualities because it is unclear which data set should be used [155].

According to [155], the histology depth is very indicative when analysing a tissue sample. The correct interpretation of the measured dielectric characteristics relies on an accurate estimate of this depth. When comparing results from measurements on different types of tissues, histology depth is crucial. In this study, the plaques were analysed in one slice only in histology, and the penetration depth of the electrical field was not studied yet for each plaque, even though the thickness was recorded. Moreover, the sample analysed by histology was not precisely the same one analysed by the microwave resonator. When studying homogeneous tissues, it is sufficient to ensure the sample is large enough so that reflections from the sample's boundaries are minimal. Histology, on the other hand, is often performed after dielectric measurements have been taken to assess the sample composition (i.e., which specific tissue types are present and their relative distribution) in cases of heterogeneous tissues. Histology depth must be properly known in this situation for correct findings interpretation. This could not be assured in this thesis as the carotid plaque was chosen to be cut into two specimens as histological analysis included preservation in formol that would have altered the microwave measurements.

The microwave sensor analysed the plaque's composition to fill the void left by the incapacity of existing radiological modalities to identify the composition of plaques with extraordinarily high sensitivity and specificity. Although preliminary, these in vitro results are highly encouraging. The in vivo potential of this resonator is now being investigated. For surgical screening, a new easy and reproducible technique to identify carotid plaques at risk would be of great value. Furthermore, dielectric characteristics of biological tissues at microwave frequencies are of great importance to study for many reasons, including the advancement of wireless communications, as the increased use of wireless technologies, such as Wi-Fi,

Bluetooth, and cellular networks, has been linked to various health problems. Understanding how the body reacts to EM fields is crucial for this reason. The other factor is the progress made in the field of MWI medical devices [154], [187]. Therefore the development of novel medical diagnostic and therapeutic applications, or the enhancement of current ones, may result from a deeper understanding of the complex permittivity of biological tissues and hence allow the production of clinically used devices [125]. An MWI sensor that can characterise biological tissues can also hold great potential in the agricultural sector, particularly in food monitoring [118].

In this thesis, a multimodal prognostic score analysis showed that using the dielectric constant value of the plaque combined with Gray-Weale classification in DUS results led to the following multimodel score formula:

$$=1.760 + (-0.062 \times \epsilon_r) + (- 3.367 \times \text{Gray-Weale classification 2\&3 vs 4\&5})$$

Using a cutoff of -4.5 allowed us to identify a VP with 77% and 70% of sensitivity and specificity, respectively (AUC= 0.8). Though very preliminary, this algorithm could prove helpful in better-selecting candidates for surgical treatment.

This study does have certain restrictions and limitations. First, despite my best efforts to accurately compare histology and microwave analysis, it was impossible to measure the specimen using our sensor while keeping it intact prior to histology; therefore, slicing it in half was the best alternative. One half was used for histology, and the other half for microwave analysis. This is due to the fact that tissues used in histology must be undamaged, fixed, and kept in formol. Therefore I cannot say with absolute certainty that the microwave samples precisely represented the histological slides. Perhaps the calcified portion of the plaque was examined by histology while the soft portion was examined by microwave, which would explain the discrepancy between the two methods. This may account for the contradictory results of those heterogeneous plaques. [155] stated that the results of a histological investigation can be effectively interpreted only by selecting the appropriate histology section and attributing any disparity between histological analysis and dielectric constant measurements to the fact that the analysed region is not always the sample. Furthermore, the histological analysis of half of the specimen sent to the histology department was only done in one slice of the sample that was 3 microns thick, which neglects all the other parts of the

specimen. In addition, the samples were preserved in physiological serum; the microwave sensor may not have detected any IPH as it dissolved in the serum. For this reason, microwave analysis may have produced inaccurate results. It is also possible that the results were affected if, in some cases, the serum got absorbed inside the plaque or it did not dry in the allotted time. Despite all this, the analyses' overall picture of the compositional differences between the carotid plaques via the dielectric constant is quite accurate.

Another challenge in exploring MWI systems is that experimental circumstances are not always precise. Although performing a dielectric measurement on a tissue sample appears basic, excess confounders can alter the measured data. These factors are likely the source of variations in reported statistics. The calibration procedure, validation procedure, reference ideal samples used for validation and accuracy of its model properties, and disconnection, reconnection, or movement of cables or probes are the main equipment-based measurement confounders shown to affect the accuracy of dielectric data [182]. The following can also produce little variations [134]: discrepancies in sample thickness (measurement errors), deformation caused by the pressure applied on the sample hence uncorrelation between simulations and real measurements. However, clinical variables have been relatively uninvestigated and may provide additional uncertainty in the dielectric data. Clinical confounders that have been identified in the literature are the tissue source, age and weight; the use of anaesthesia/drugs; physiological parameters; in-vivo vs ex-vivo measurements; time since death or excision; the sample temperature and cooling or warming of the sample; sample dehydration and blood loss; contamination or artificial drying of surface; quality of probe-sample contact; probe-sample pressure; the sensing depth and sample size; tissue sample heterogeneity; the technique for marking measurement location on the tissue sample; sample or data exclusion criteria; pathologist methodology; and the histological analysis technique [182]. In addition, if the dielectric characteristics of the tissues are not examined at different temperatures and frequencies, it is difficult to tell if the models accurately reflect the dielectric properties of the tissues [125]. Therefore, the dielectric characteristics of various human tissue types have been the subject of many scientific investigations [109]. To my knowledge, no one has attempted to measure the dielectric characteristics of the carotid atherosclerotic plaques; thus, we do not have any database to compare it with for validation.

We ascribe the observed disparities in the carotid plaque dielectric constant to the carotid plaque's heterogeneity and the variation in processes and protocols used throughout the different investigations. By necessity, dielectric spectroscopic techniques average the dielectric properties of the entire volume probed by electromagnetic fields. Thus, heterogeneity presents a unique barrier to identifying the true range of tissue-specific dielectric characteristics of carotid plaques.

Additionally, the proximity of the dielectric constant values of lipidic and calcified components may help explain the dielectric constant variation within each group (symptomatic, asymptomatic, VP, NVP). In theory, the dielectric constant of blood, fat, and bones was proposed as a reference, but on a physiological level, the composition of atherosclerotic plaque is not essentially the same as those tissues. For example, in a study on breast tissue, they could not distinguish between the impacts of fibroconnective and glandular tissue types on the overall dielectric characteristics of breast tissue, as they both increase the sample's dielectric properties as their contribution to the tissue composition increases. In addition, since all three tissue types are interdependent (i.e., their contributions must always total up to 100 per cent), they could not be analyzed separately [119]. In the context of carotid plaques, even on a histological level, the components were difficult to distinguish, as they included partially calcified fibrosis, highly calcified LRNC, etc.

While MRI has been shown to identify VP and NVP with great accuracy [196]. We could not incorporate it into my thesis as the vascular department where I conducted my research evaluates carotid lesions using only DUS and CTA. This is because MRI access is more complicated, expensive, and time-consuming, and many vascular surgeons are less practised with this modality than CTA and DUS. This research aimed to utilise the most regularly used modalities for carotid examination. However, the addition of MRI would have supported this study's hypothesis.

5.4 Conclusion

Routine use of multimodal characterisation of carotid plaques should be encouraged to determine which individuals may benefit the most from surgical intervention. The preoperative

utilisation of a microwave biosensor to diagnose carotid plaques is a technique that is currently in its developmental stages but has the potential to be functional one day.

In the following chapter, the second and comparatively more minor part of this PhD will be presented, which involves evaluating the sensor on animal tissues and phantoms representing the human neck.

Chapter VI - Moving Beyond the Single Layer: Navigating the Transition to in-vivo Multilayer Models

Since the ultimate purpose of the resonator is to produce a device that can be placed on the patient's neck, and as the project evolved and the carotid plaque analysis showed some encouraging results, it was essential to test the resonator's ability to measure the tissues in the neck anterior to the carotid plaque. In contrast to the basic one-layer heterogeneous model tested with the carotid plaques ex-vivo, the human body has multiple layers of tissues that the sensors' signals must pass through to reach the plaque. Hence, the frequency response shifts should be less pronounced than those observed on the carotid plaques.

The human neck has several layers before the carotid artery (Fig.63), each with its unique structure and function. These layers, from superficial to deep, include:

1. Skin: the outermost layer of the neck and serves as a protective barrier against external stimuli.
2. Subcutaneous Tissue (SAT): This layer of fat and connective tissue provides insulation and cushioning for the neck.
3. Fascia: The fascia is a dense connective tissue that covers and separates the neck muscles.
4. Muscles: The neck contains several muscles responsible for movement and stability, including the sternocleidomastoid (SCM), scalenes, and splenius muscles.
5. Nerves: The neck contains several nerves, including the spinal accessory and phrenic nerve, which control movement and sensation in the neck and upper extremities.

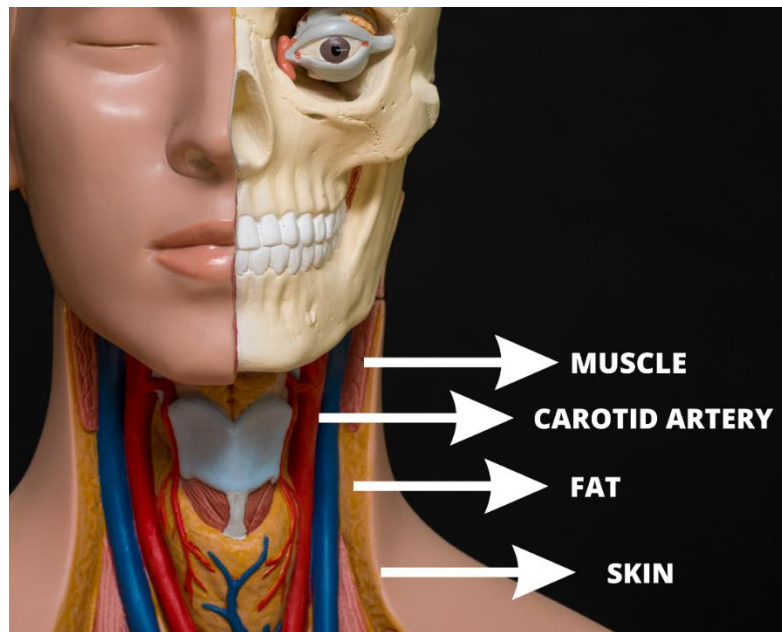


Figure 63. The neck anatomy

Thus, measurements were obtained of animal tissue samples representing the principal layers of the neck, including skin, fat, and muscle. These layers were selected due to their availability and accessibility, in addition to the fact that they are the most extensive segment representing the neck layers.

According to [184], planning each set of measurements for the experimental purpose effectively reduces tissue-related confounders. The first stage is deciding which animals to study and what kind of tissue to collect as a sample (since the dielectric characteristics could change depending on the animals' age or weight).

6.1 Animal tissues

The first batch of samples was of pork origin, and the age and dehydration stage of the samples were unknown as they were collected from the butcher the morning of the analysis. Pig tissues are often used in medical device testing as they are similar in structure and function to human tissues, which provides a good approximation of how the device will perform in the human

body. Using ex-vivo animal tissues to replace human tissues exemplifies how our animal study followed the 3Rs guidelines for humane research (replace, reduce, refine) [207].

The pork's skin, fat, and muscle tissues were organized in layers. According to [136], the EM characteristics of these tissues are consistent with those of human tissues. In light of this, the values in [Table 5](#) (*section 2.2.3*) are used as reference data. The depth into a tissue contributing to the dielectric measurement was studied by [123] and [208], although the two groups specified the depth parameter differently. Recently, [155] showed how the frequency and dielectric characteristics of the tissues occupying the sensing volume could affect the calculated sensing depth value based on a variety of definitions of the sensing depth.

A simplified version of the multi-layer neck model was created by [209] (Fig.64). The SCM is located beneath the skin's epidermis and dermis (Fig.65), which together measure around 1 – 2 mm in thickness, and the subcutaneous fat layer, the thickness of which varies from person to person.

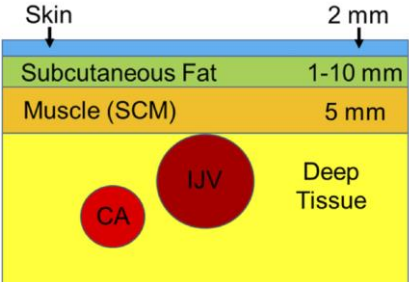


Figure 64. The neck layers' thickness, according to [209]

The typical thickness of an SCM is 5 mm. Below the SCM, the Internal Jugular Vein (IJV) was modelled as a cylinder with a 5 mm radius, while the Carotid Artery (CA) was represented as a cylinder with a 3.5 mm radius. In other studies, the average epidermal thickness in the anterior neck in humans is 0.0407 mm, the dermal thickness is 1.23 mm [210], and the SCM thickness is 5.34 mm [211].

Following collection, the animal samples underwent the exact calibration, verification, and thickness measurement steps as the carotid plaques. They were similarly inserted on the glass layer in the plexiglass structure after being cut into a circular shape. The layers were measured

independently and then in a multi-layer model. The skin was measured on both sides, while fat and muscle were measured on one side only.

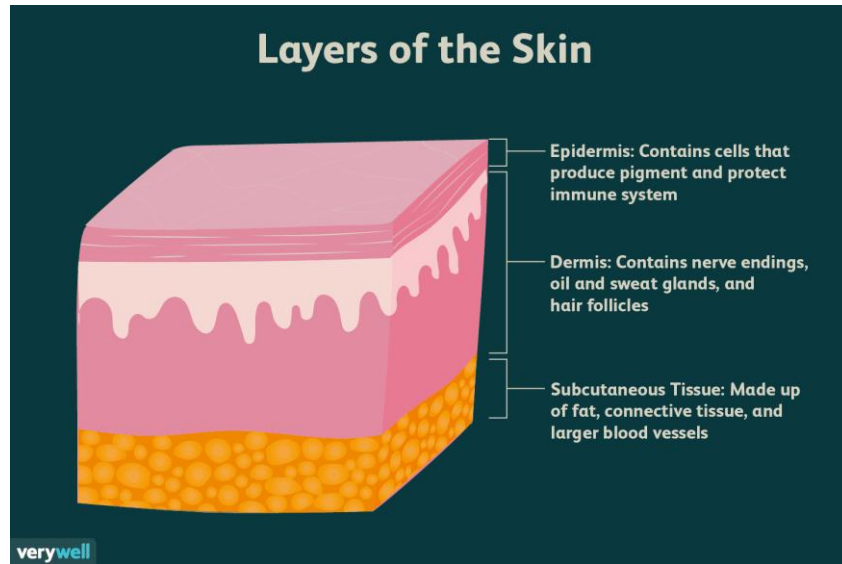


Figure 65. The three layers of the skin [212]

A 3.4 mm thick skin sample was characterized by first situating the exterior portion of the sample, made primarily of keratin and then the inside portion, which is composed primarily of adipose fat (Fig.65). Therefore, the skin was considered a bilayer structure, and dielectric permittivity was measured depending on the side in direct contact with the resonator. When the inside skin layer is applied to the sensor, the resonant $\Delta f = 256$ MHz, which is half of the Δf when the outer layer of skin is applied = 517 MHz (Fig.66). Simulations under HFSS of the skin have allowed the parameters of these tissues to be extracted (Table 16). These findings are not consistent with the SAT values in Table 4; however, they are consistent with the non-infiltrated fat values [213]. Moreover, $\epsilon_r = 14$ was found for the epidermis, which is much lower than that given in the databases. This could be the result of dehydration, as the animal sample was excised at least several hours before the analysis.

As observed, the lack of blood flow and dehydration significantly influences the ex-vivo biological tissue measurements of the dielectric constant. For example, in a study by *Dubuc et al.*, an experiment was performed utilising near-field microwave sensing techniques on two mice. In vitro microwave results found more significant dielectric differences between

tumorous and healthy tissue, while in vivo tests revealed enhanced parameters consistent with the increased vascularisation density and, consequently, water volume in vitro tissues [214].

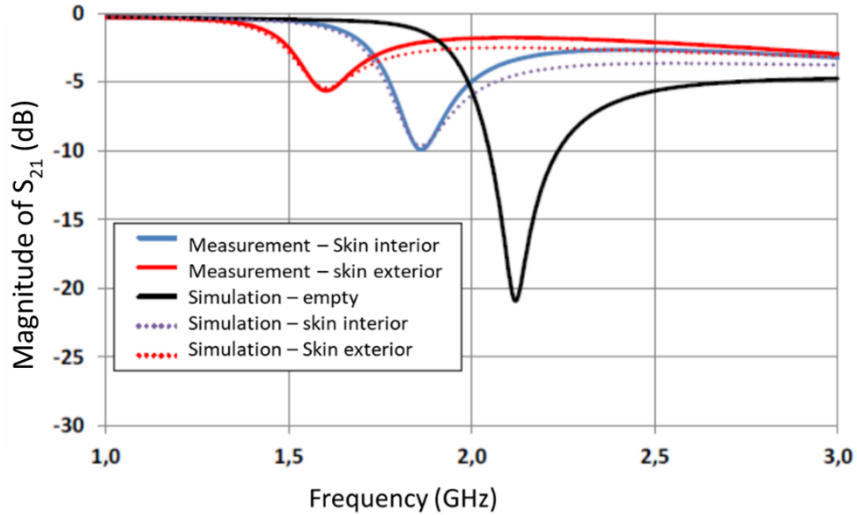


Figure 66. Measurements and HFSS simulations of the pig skin layers

Table 16. The frequency shift, dielectric constant, and losses of the first pig samples

Tissue sample	Δf (MHz)	ϵ_r	$\tan \delta$
Skin interior (SAT)	256	5	0.23
Skin exterior (epidermis)	517	14	0.28
Fat	257	4.8	0.29
Muscle	868	54	0.41
Multilayer (skin, fat, muscle)	349	7	0.22

Furthermore, to date, only basic setups have been fully modelled to assess the effect of tissue heterogeneity. For bilayer materials, [72] [143] showed that the permittivity of either layer might be determined from the reflection coefficient, with no knowledge of the first layer's thickness or the probe capacitances required. Bilayer material effective dielectric characteristics have also been modelled in [107], in general and in the context of coaxial probes. Additional work [107] generalized these findings to the case of multilayer materials. To investigate the effect of changes in layer parameters (such as thickness and permittivity) on the dielectric

measurement with frequency, *Huclova et al.* employed a numerical three-layer skin model [184].

After the skin analysis, a 4.5 mm thick fat sample was measured and simulated. The values of the recovered parameters, $\epsilon_r = 4.8$ from the simulated curves in Figure 67 and Table 16, are in good agreement with the published data (Table.5) at the frequency under consideration. Figure 67 depicts the frequency responses of the measured and simulated sample.

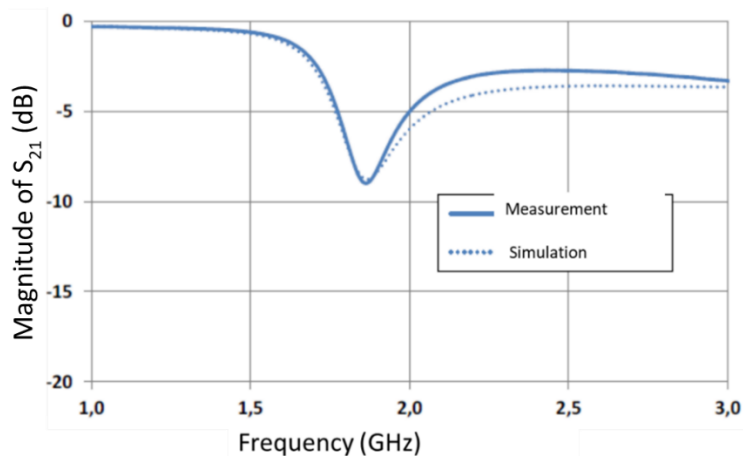


Figure 67 Measurements and simulations of the pig fat layer

The sample of pig muscle used was 7.7 mm thick. The findings revealed a substantially more significant frequency shift than the other samples investigated, with a significant decrease in the amplitude of $|S_{21}|$ at resonance and a strong peak broadening (Fig.68). This indicates that the muscle has substantial dielectric losses due to its high-water content; the results presented in Table 16 are consistent with those of the literature (Table 5).

Numerical and experimental verifications demonstrated that f_r and $\tan \delta$ responses are correlated with the thicknesses of fat and muscle tissues. Due to its low water content, adipose tissue has the lowest relative permittivity of any biological tissue, hovering around 5 (at 2.2 GHz). Since muscle contains much water, its relative permittivity is 53, which is lower than that of blood ($\epsilon_r=58$). As a result, there is an extensive range in the frequency dependence of relative permittivity in tissues with high water content.

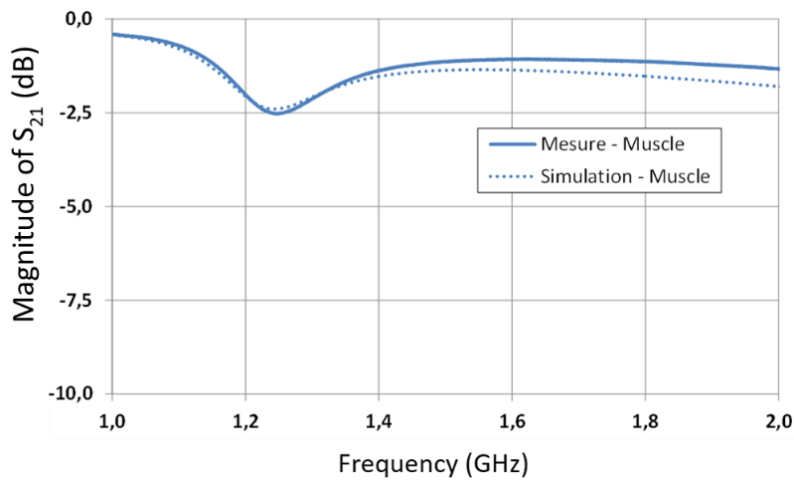


Figure 68. Measurements and HFSS simulations of the pig muscle layer

6.2 Multilayer model

A multilayer prototype was then put together using those monolayers positioned on the resonator in the sequence in which they occur in an in-vivo model, i.e., skin (external face), fat, then muscle (Fig.69). Figure 70 depicts the preliminary results acquired for the multilayer and those simulated under HFSS using approximated parameters representative of this multilayer structure (layer thicknesses, dielectric permittivities). The simulation revealed a reduction in amplitude at resonance and a broadening of the resonance width. The observed resonance shift is more significant than that measured by 180 MHz to low frequencies. This could be explained by the top layers adding pressure on the skin layer, diminishing its thickness and apparent dielectric permittivity. $\epsilon_r = 13.5$ and $\tan \delta = 0.28$ correspond to the simulation's global parameters.

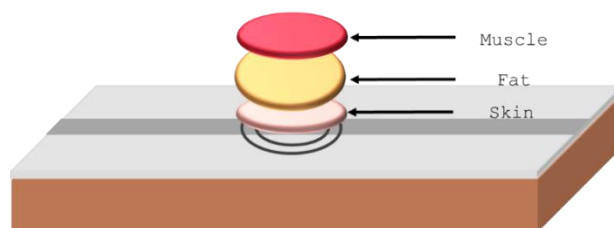


Figure 69. Multilayer model of pig tissues placed on the resonator.

A multilayer structure optimization reduced this frequency shift and extracted the multilayer's equivalent dielectric constant ($\epsilon_r = 7$) and losses ($\tan \delta = 0.22$). The simulation's higher dielectric constant is more consistent with the predictions of a structured skin-fat medium, favouring greater wave penetration in the multilayer (Table 16). Two significant factors are at play here: i) dielectric losses due to material properties and (ii) reflection signal loss as it travels through numerous layers of tissue. The thickness of more conductive tissues, like the muscle layer, also affects the penetration depth at a given distance. Given the large difference in dielectric constants between the muscle and fat layers, even relatively thin muscle layers can serve as effective barriers that keep signals within the fat layer.

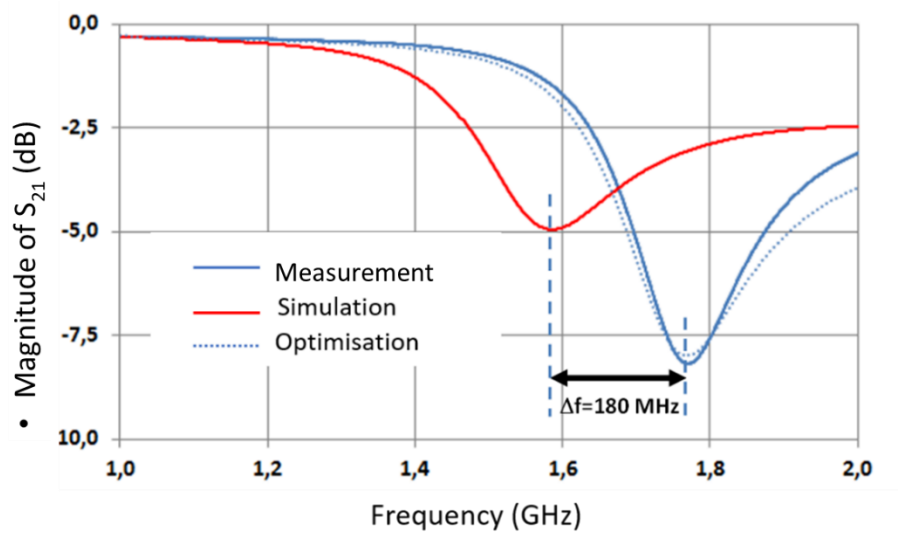


Figure 70. Measurement, simulation, and optimisation of the pig multilayer model

A few months later, the problem of the samples' undetermined excision time was alleviated by the availability of freshly dissected specimens for analysis. A surgeon was testing an orthopaedic medical device on a pig in a study approved by the French Ministry of Research (under authorization number 20287, the Animal Care and Use Committee number 16 EnvA-anses-upec), and took samples of skin, fat, and muscle as part of the experiment. The adult pig (*sus 2 scrofa domesticus*) had the surgery at the dorsal level.

Those excised tissues no longer in use were collected and placed in an airtight, insulated container in a cooler bag and transported to our laboratory. The samples were delivered to our

laboratory roughly two hours after the extraction, where the experiment commenced. As was described previously for the bench testing steps, the VNA was turned on that morning, and the necessary calibration and preparation procedures were carried out upon arrival. Each layer was approximately 5 cm long and 3 cm wide. The specimens were cut into two samples each, and all were preserved in the container to prevent drying while measuring them individually in a single layer form and then in a multilayer model (Fig.71). The room temperature was 23°C, and the temperature of the samples was at 20°C.

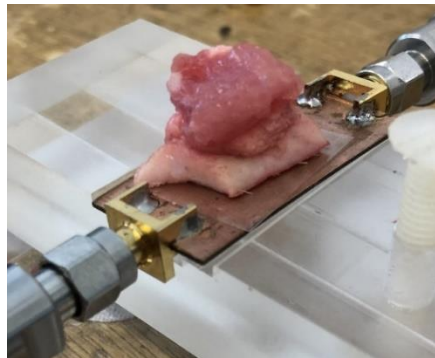


Figure 71. Multilayer model of (skin, fat, and muscle), the upper part of the Plexiglas was removed for picture purposes.

In contrast to the measurements described by [159], which were all taken at body temperature (37 degrees Celsius) and how this temperature is obtained is not reported, the data presented here were collected at room temperature. Heating the tissue was avoided since it would impair tissue dryness, and the data would not be representative. Therefore, the Minimum Information for Dielectric Measurements of Biological Tissues (MINDER) principles were adhered to by not heating the tissues and reporting the measurement temperature. The dielectric characteristics are temperature sensitive, a drawback of this method. Thus, the dielectric characteristics of the multiple biological tissues at body temperature were not reflected but rather at room temperature. The effect of temperature on tissue dielectric properties has been extensively studied in the scientific literature. The ambient and body temperatures must be regulated in order to obtain a standard measurement. Even when the tissue temperature was held constant during previous studies, dehydration was observed. Depending on the ambient temperature, the tissue sample size, the tissue's water content, the tissue handling techniques,

and the length of time the tissue is exposed to air, surface dehydration can have varying effects. All of these factors must be considered during in-vitro and in-vivo measurements.

These samples were analysed using the sensor described in this thesis as well as the newly fabricated sensor with improved designs. The first article attached in the appendix shows the details of those new sensors in addition to the results of the samples mentioned above. Moreover, the tissues' E-field distribution was investigated to estimate the penetration depth. A summary of those samples' dielectric constant and losses can be observed in Table 17. Most of the data were quite close to their theorised value.

Table 17. The parameters recorded during the experiment and the extracted results of the pig sample

Tissue sample	ϵ_r	$\tan \delta$	Thickness (mm)	Time
Skin - epidermis	45	0.30	6.6	13:00
Dermis	21	0.33	6.6	13:00
SAT	10.5	0.25	4	13:10
Muscle	47	0.28	3.2	12:45

Multiple factors may account for the discrepancies between the results [136]. While the database we used (Table 5) had built its model on data from the literature and data from experimental research on numerous other species, the data in this study were measured on pork tissues only. Therefore, four causes could explain the discrepancies between the database and those results: tissue temperature, hydration, species differences, and regional variations. Moreover, [155] emphasised that despite the apparent similarity between the animal tissue samples, the underlying biological variability means that no two tissue samples will ever be identical.

Despite the uncertainties caused by possible deterioration of the samples in these ex-vivo tests, the CSRR sensor has enabled the classification and characterisation of the analysed samples based on their dielectric properties. The observations on animal tissues are reasonably consistent with those reported in the literature, considering the limited number of tissues tested. This reveals the potential ability of the biosensor to differentiate the dielectric characteristics of diverse biological tissues. The microwave dielectric characterization approach is sensitive enough to detect alterations in tissue composition. As a result of this preliminary research, it

could be potentially possible to estimate the dielectric properties of each of the tissues that microwaves pass through before reaching the carotid plaque. However, the bench testing of multilayer structures constructed from these elementary layers is challenging due to the difficulty of controlling all structural factors, and it must be repeated on a large number of samples. In the creation of MWI devices, even a slight discrepancy in the dielectric characteristics can significantly impact the device's accuracy and reliability. More importantly, the findings imply that extrapolating the dielectric characteristics of tissues from one animal species to another may not be valid.

Notwithstanding the results of this study and all the promising rising MWI technologies, the diagnostic use of microwaves presents significant difficulties. Recent years have seen a plethora of studies devoted to imaging both the breast and the brain, and dedicated imaging equipment has been developed to serve both of these uses. Breast and brain imaging researchers have employed qualitative and quantitative inversion techniques to create dielectric reconstructions. In qualitative techniques, that interest is in recovering the locations, size, or other characteristics of the discontinuities inside the body [112]. Quantitative methods, on the other hand, attempt to reconstruct complete distributions of dielectric characteristics inside the target. These data correlate with dielectric discontinuities, enabling direct visualisation of the pathology's consequences. From a computational standpoint, quantitative techniques are typically more time-consuming and costly [112].

Moreover, it is essential to remember that when the tissues are assumed to be homogeneous, there is still a degree of variability in the measured dielectric characteristics. Consequentially, the results of permittivity measurements taken at various sites on the same specimen can vary substantially.

[163] report that the measured range of standard deviation is around 6% for the real part of the permittivity and between 8% and 10% for the imaginary component of the permittivity, based on their extensive measurement investigation. It is believed to originate from a mix of biological tissue variations and localised temperature variations at the measurement sites. Similarly, [213] reports that the variability of their results was within 5%, indicating that changes in tissue qualities within a species may very well exceed those across species. When comparing

measurements taken from similar specimens, this is an additional cause of uncertainty that must be accounted for. This could be another reason for the inconsistent values of the pig tissues that were tested here, in addition to the temperature and dehydration status of the samples.

6.3 Phantoms

Phantoms are used for medical device testing as they are designed to mimic the properties of human tissues and organs. This allows testing the device in a controlled and repeatable way before they are used on real patients. Any medical device can potentially be dangerous, so testing them in a safe and controlled environment is essential. Phantoms are designed to have consistent physical properties, which makes it easier to repeat tests and compare results. This helps ensure that the future device performs consistently and reliably across different testing scenarios.

Furthermore, testing medical devices on real patients is expensive and time-consuming. Everyone working on a medical device must comply with regulatory standards requiring controlled and repeatable testing. Using phantoms can help demonstrate that the devices meet these requirements. Numerous phantoms have been discovered and designed recently, including real and virtual phantoms. Real phantoms can be divided into three categories: liquid, semi-solid (gel), and solid (dry). Several phantoms depicting human body layers are shown in the following paragraph.

In a study by [215] on bladder monitoring, several bladder phantoms were constructed as three-layer models. Tissue-mimicking material having dielectric characteristics similar to human muscle was present in the first and third layers. A saline solution with dielectric characteristics like those of urine was put in the intermediate layer.

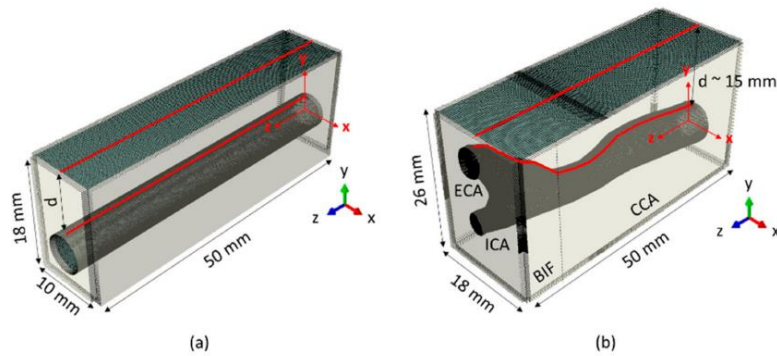


Figure 72. (a) The common carotid artery (CCA) geometry is embedded within a cuboidal domain. The free (skin) surface is dark grey, while infinite mesh elements placed on the outer boundaries are light grey. (b) Geometry of the patient-specific CA embedded within a cuboidal domain. Sub-regions common carotid artery, CCA; bifurcation, BIF; ICA and external carotid artery, ECA are indicated [216].

For brain imaging, numerical analytic models were favoured [217], [218]. In the carotid artery phantoms field, numerical and physical models were used depending on the technique tested. Building a 3D replica of the carotid artery, complete with a plaque inside, out of dielectric material, is an advantage for the future. *Abaqus 14.1*, a finite element method program, was used to study the carotid model (Fig.73) [216].

[219] produced a carotid bifurcation model made of silicone rubber from CTA images of a 75-year-old patient's common carotid bifurcation with significant ICA stenosis (Fig.74).

[220] made a head model for non-invasive healing monitoring after craniostylosis-based surgery with just three primary homogenous materials: skin, bone, and brain (Fig.75). They are all assumed to have dielectric properties in the microwave range comparable to the natural tissue. The skin in the head phantom model was 1 mm thick, while the underlying skull was 6.5 mm thick and 51 mm² in size. In order to simulate the skin, brain, and bone, agar-based phantoms were used. Using the three-layer head model, the antenna was simulated. Computational simulations confirmed the expected poor radiation pattern (typical of a near-field device) and located the majority of the electric field distribution in the target region. The phantom measurements were found to be consistent with that of the simulated scenarios [220].

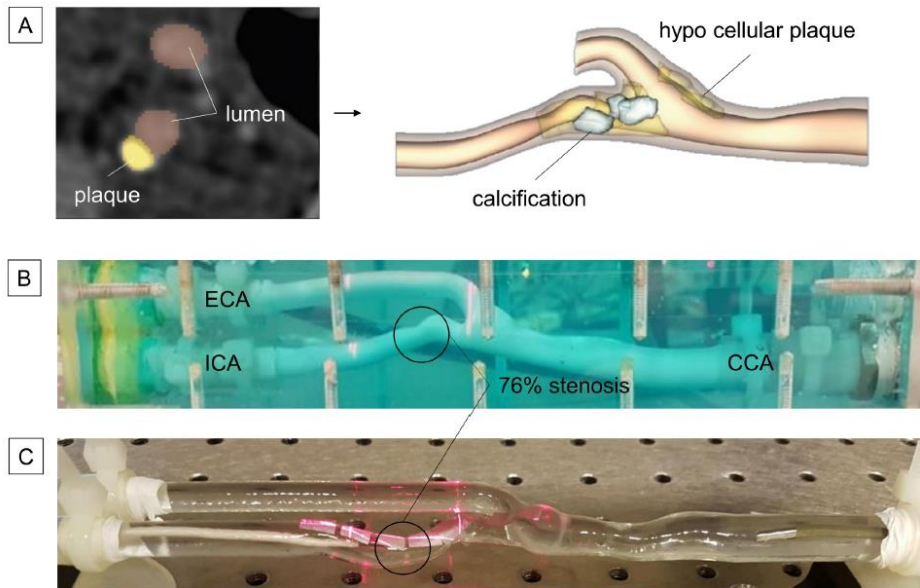


Figure 73. (A) CTA images of the carotid bifurcation from a 75-year-old male were processed to obtain a patient-specific model of the plaque-free stenosed vessel. The compliant (B) and stiff (C) models used for the hydraulic tests replicate the geometry of the patient-specific common carotid artery (CCA), external carotid artery (ECA), and ICA where the 76% area stenosis (circled) is located [219].

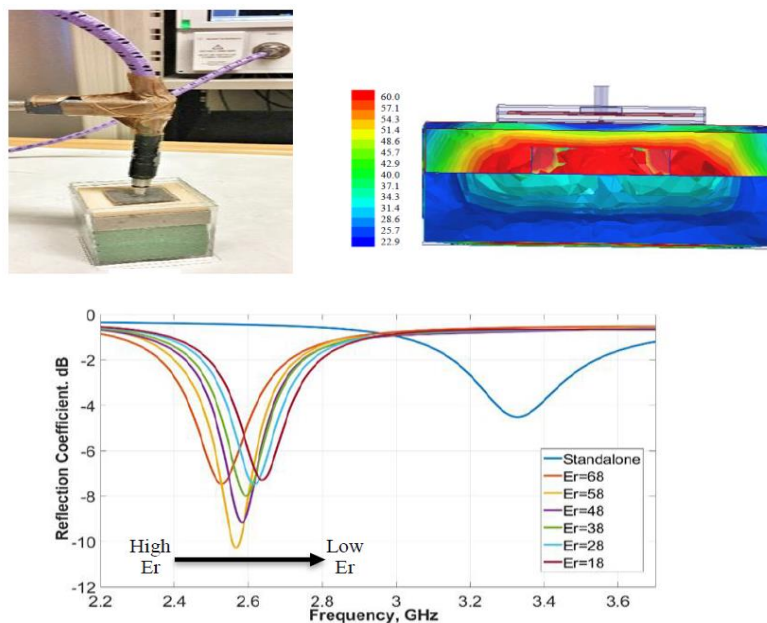


Figure 74. Distribution of electric field after simulation of the sensor on a phantom with CST and the simulated resonance frequency curve of the antenna with head phantom, with variation in dielectric constant from 18 to 68 [220].

For the purpose of this thesis, two phantoms were tested. The LifeLike VI Embedded Carotid Arteries with Plaque and Dermis Model and the LifeLike Double Layer Skin (© 2021 LifeLike BioTissue, Canada) were chosen as the most realistic models of the carotid artery with a plaque and the layers before it. Those phantoms are realistic and affordable solutions designed to acquire, retain, and improve basic and advanced vascular and general surgical skills. Life-like tissue phantoms are artificial models designed to mimic human tissue's mechanical, optical, and physiological properties. However, the electrical properties were unknown to the producer. They are made by proprietary polymer processing hydrogel technology.



Figure 75. The LifeLike VI Embedded Carotid Arteries with Plaque

The Dermis Model of the skin measured 3.3 mm in dermis thickness and 4.5 mm in fat thickness. The carotid artery model (Fig. 76) dimensions are found in Table.18. Those phantoms were measured multiple times with the FR4 resonator and with new resonators that my colleague Mrs Masini developed for her thesis, which is the sequel to mine (Table.19). Therefore, the results are still in progress.

Table 18. Dimensions of the carotid phantom used (ID = Inside Diameter, OD= Outside diameter)

Thickness	1.0"
Common carotid size	10 mm ID, 13 mm OD
Internal carotid size	6 mm ID, 8 mm OD
External carotid size	4 mm ID, 6 mm OD
Dermis thickness	2.2 mm

Table 19. First practical measures of the skin phantom

	Sample 1 f_0 (GHz)	Sample 2 f_0 (GHz)
Skin	1.486	1.504
Fat	1.756	1.558
Skin + fat	1.468	1.486
Fat + skin	1.972	1.84

6.4 Conclusion

All results from the literature, including this study, should be interpreted cautiously for the reasons mentioned above.

Therefore, the development of MWI clinical devices is still in its early stages, and several technical limitations need to be overcome, including the need for better sensors, improved signal processing algorithms, and more efficient data processing systems.

In conclusion, there are several challenges associated with MWI, e.g. the complexity of tissues; the dielectric properties of biological tissues vary greatly depending on the tissue type and its state of health. This can make it challenging to interpret the information obtained from MWI accurately. Another challenge is the limited penetration depth; MWI has limited penetration depth, meaning it is only effective for imaging shallow structures within the body. This makes it challenging to image deep-seated structures such as organs or tumours.

Conclusion & Perspectives

As of this writing, no particular technique can definitively determine which plaques are vulnerable, require surgical removal, and which are stable and can be treated with the best medical treatment alone. Consequently, new modalities are anticipated.

This was the purpose of developing the planar microwave biosensor operating in the centimetre band based on the CSRR structure. This biosensor was created using conventional printed circuit technology in this microwave domain. In addition to its small dimensions ($\lambda/10$), it has excellent resonant properties with a relatively good quality coefficient (~ 80). Those factors play an essential role in accurately characterising the dielectric parameters of biological tissues.

This thesis used this biosensor primarily to identify the composition of different atheromatous carotid plaques. Those plaques were obtained post-carotid endarterectomy from symptomatic and asymptomatic patients. Initially, the aim was to obtain at least one hundred carotid plaques of different clinical states to perform a statistical study that shows the biosensor's ability to differentiate stable plaques from those at risk.

Nonetheless, due to the impact of the COVID-19 pandemic of no access to patients for three months, followed by very limited access even after the partial easing of lockdown restrictions as a result of the reduction in the number of surgeries due to the shortage of operation theatres, the assessment hence was conducted on a sample size of 50 patients.

A complete histological analysis of all plaques was conducted in parallel in addition to the routinely used imaging modalities, i.e., DUS and CT, to validate the biosensor results.

Every patient had undergone DUS and CT as part of their routine clinical examination before the study; however, an additional detailed ultrasound scan was done the day before the operation, and the CT results were interpreted in extensive detail with an exhaustive investigation only for this study. Each patient's clinical data and medical history were recorded before and after the operation. The composition measurements of the plaques using the biosensor were performed post-op. The signal reflected by each sample varied depending on the composition of the plaque. At this frequency, no risk is expected.

The results of all medical imaging techniques were correlated statistically with the relative permittivity of the carotid plaques against the gold standard, i.e. histology.

Of the various standard imaging modalities that have been incorporated, DUS has been demonstrated to be the most reliable and easily accessible method. The CT results were not quite as astounding as described in the literature, and the PVFA values were, to our surprise, the exact opposite of what the recently available publications propose.

The histological study yielded useful findings; nevertheless, there needs to be a standardised method of histological analysis that could guarantee the inclusion of all the sample components. A significant correlation was observed between the ultrasound echogenicity groups and the dielectric constant of the carotid plaques. The ability of the microwave sensor to identify VPs in-vitro appears promising. The end goal is a transcutaneous microwave biosensor that could help in decision-making.

Nonetheless, there is much space for improvement in the method used and bench testing. There is still a considerable amount of research to be carried out to clearly distinguish the plaque's fatty components from the calcified components, as these two have a dielectric constant that is almost in the same range. This investigation establishes the groundwork for future research.

Additional development of microwave sensor technology is required to make possible a more accurate characterisation of plaque and to transform the device into a diagnostic tool that medical practitioners can use. Even if the preliminary data obtained from the biosensor are encouraging, additional results are necessary to guarantee the sensor's dependability and efficiency. Independent verification of the depth of the electrical field penetration is required, and depending on the findings, either the substrate, the design, or the frequency may need to be adjusted.

In addition, further work must be done on the pressure control system to make the results more reliably reproducible. Finally, the upgraded sensor that will be chosen needs to be validated by being tested on a large number of ex-vivo samples and phantoms. The findings of these measurements need to be reproducible and consistent so they can be used as a benchmark for the measurements that will be done in-vivo. My fellow PhD student is continuing to make headway on this project.

Bibliography

- [1] V. L. Feigin *et al.*, ‘Global, regional, and national burden of stroke and its risk factors, 1990–2019: a systematic analysis for the Global Burden of Disease Study 2019’, *The Lancet Neurology*, vol. 20, no. 10, pp. 795–820, Oct. 2021, doi: 10.1016/S1474-4422(21)00252-0.
- [2] A. Mishra *et al.*, ‘Stroke genetics informs drug discovery and risk prediction across ancestries’, *Nature*, vol. 611, no. 7934, pp. 115–123, Nov. 2022, doi: 10.1038/s41586-022-05165-3.
- [3] INSERM, ‘Accident vasculaire cérébral (AVC) La première cause de handicap acquis de l’adulte’, 2017. <https://www.inserm.fr/dossier/accident-vasculaire-cerebral-avc/>
- [4] E. Messas *et al.*, ‘Management of carotid stenosis for primary and secondary prevention of stroke: State-of-the-art 2020: A critical review’, *European Heart Journal, Supplement*, vol. 22, pp. M35-M42B, 2020, doi: 10.1093/EURHEARTJ/SUAA162.
- [5] Stroke Info, ‘Stroke Facts & Statistics’, *Stroke Awareness Foundation*. <https://www.strokeinfo.org/stroke-facts-statistics/>
- [6] H. P. Adams *et al.*, ‘Classification of Subtype of Acute Ischemic Stroke Definitions for Use in a Multicenter Clinical Trial’. [Online]. Available: <http://ahajournals.org>
- [7] E. Jauch, ‘Guidelines for the Early Management of Patients With Acute Ischemic Stroke’, *Stroke*, vol. 44, no. 3, pp. 870–947, 2013, doi: 10.1161/STR.0b013e318284056a.
- [8] D. Dowlatshahi *et al.*, ‘Predicting Intracerebral Hemorrhage Growth with the Spot Sign: The Effect of Onset-to-Scan Time’, *Stroke*, vol. 47, no. 3, pp. 695–700, Mar. 2016, doi: 10.1161/STROKEAHA.115.012012.
- [9] E. S. Connolly *et al.*, ‘Guidelines for the management of aneurysmal subarachnoid hemorrhage: A guideline for healthcare professionals from the american heart association/american stroke association’, *Stroke*, vol. 43, no. 6, pp. 1711–1737, Jun. 2012, doi: 10.1161/STR.0b013e3182587839.
- [10] E. Qaja, P. Tadi, and P. T. Kariyanna, ‘Carotid Artery Stenosis’, *Handbook of Endovascular Peripheral Interventions*, pp. 215–240, Aug. 2022, doi: 10.1007/978-1-4614-0839-0_12.
- [11] P. Sobieszczyk and J. Beckman, ‘Carotid artery disease’, *Circulation*, vol. 114, no. 7, Aug. 2006, doi: 10.1161/CIRCULATIONAHA.105.542860.
- [12] R. Araso, A. Arasu, and J. Muller, ‘Carotid artery stenosis An approach to its diagnosis and management’, *The Royal Australian College of General Practitioners*, vol. 50, pp. 821–825, Nov. 2021.
- [13] M. H. F. Poorthuis *et al.*, ‘Development and Internal Validation of a Risk Score to Detect Asymptomatic Carotid Stenosis’, *European Journal of Vascular and Endovascular Surgery*, vol. 61, no. 3, pp. 365–373, Mar. 2021, doi: 10.1016/j.ejvs.2020.11.029.
- [14] A. S. Larson *et al.*, ‘Carotid intraplaque hemorrhage and stenosis: At what stage of plaque progression does intraplaque hemorrhage occur, and when is it most likely to be associated with symptoms?’, *American Journal of Neuroradiology*, vol. 42, no. 7, pp. 1285–1290, Jul. 2021, doi: 10.3174/ajnr.A7133.

- [15] V. Crespy *et al.*, ‘Impact of the first COVID-19 pandemic peak and lockdown on the interventional management of carotid artery stenosis in France’, *Journal of Vascular Surgery*, vol. 75, no. 5, pp. 1670-1678.e2, May 2022, doi: 10.1016/j.jvs.2021.11.064.
- [16] H. Hetterich *et al.*, ‘Grating-based X-ray phase-contrast tomography of atherosclerotic plaque at high photon energies’, *Zeitschrift für Medizinische Physik*, vol. 23, no. 3, pp. 194–203, Sep. 2013, doi: 10.1016/j.zemedi.2012.12.001.
- [17] L. Hermus, G. M. van Dam, and C. J. Zeebregts, ‘Advanced Carotid Plaque Imaging’, *European Journal of Vascular and Endovascular Surgery*, vol. 39, no. 2, pp. 125–133, Feb. 2010, doi: 10.1016/j.ejvs.2009.11.020.
- [18] S. Zhang, H. Gu, X. Yu, B. Kang, X. Yuan, and X. Wang, ‘Association Between Carotid Artery Perivascular Fat Density and Intraplaque Hemorrhage’, *Frontiers in Cardiovascular Medicine*, vol. 8, Sep. 2021, doi: 10.3389/fcvm.2021.735794.
- [19] R. W. Chang *et al.*, ‘Incidence of Ischemic Stroke in Patients with Asymptomatic Severe Carotid Stenosis Without Surgical Intervention’, *JAMA*, vol. 327, no. 20, pp. 1974–1982, May 2022, doi: 10.1001/jama.2022.4835.
- [20] E. Qaja and P. T. Kariyanna, ‘Carotid Artery Surgery’, *Neurovascular Imaging: From Basics to Advanced Concepts*, pp. 191–201, Jul. 2022, doi: 10.1007/978-1-4614-9029-6_51.
- [21] E. Uthman, ‘Atherosclerotic plaque from carotid endarterectomy (gross pathology)’, *Radio Paedia*, May 2020, doi: <https://doi.org/10.53347/rID-77475>.
- [22] P. A. Ringleb *et al.*, ‘Carotid endarterectomy or stenting or best medical treatment alone for moderate-to-severe asymptomatic carotid artery stenosis: 5-year results of a multicentre, randomised controlled trial’, 2022. [Online]. Available: www.thelancet.com/neurology
- [23] G. Louridas and A. Junaid, ‘Management of carotid artery stenosis Update for family physicians’, *CME*, vol. 51, no. 7, pp. 984–989, Jul. 2005.
- [24] L. Saba and G. Mallarini, ‘A comparison between NASCET and ECST methods in the study of carotids: Evaluation using Multi-Detector-Row CT angiography’, *European Journal of Radiology*, vol. 76, no. 1, pp. 42–47, Oct. 2010, doi: 10.1016/j.ejrad.2009.04.064.
- [25] J. M. Wardlaw and S. Lewis, ‘Carotid stenosis measurement on colour Doppler ultrasound: Agreement of ECST, NASCET and CCA methods applied to ultrasound with intra-arterial angiographic stenosis measurement’, *European Journal of Radiology*, vol. 56, no. 2, pp. 205–211, Nov. 2005, doi: 10.1016/j.ejrad.2005.04.021.
- [26] A. Pierro, P. Modugno, R. Iezzi, and S. Cilla, ‘Challenges and Pitfalls in CT-Angiography Evaluation of Carotid Bulb Stenosis: Is It Time for a Reappraisal?’, *Life*, vol. 12, no. 11, Nov. 2022, doi: 10.3390/life12111678.
- [27] M. L. Flaherty *et al.*, ‘Carotid artery stenosis as a cause of stroke’, *Neuroepidemiology*, vol. 40, no. 1, pp. 36–41, Dec. 2012, doi: 10.1159/000341410.
- [28] B. Nasr *et al.*, ‘Late Outcomes of Carotid Artery Stenting for Radiation Therapy-Induced Carotid Stenosis’, *Journal of Endovascular Therapy*, vol. 29, no. 6, pp. 921–928, Dec. 2022, doi: 10.1177/15266028211068757.

- [29] R. Coscas *et al.*, ‘Open surgery remains a valid option for the treatment of recurrent carotid stenosis’, *Journal of Vascular Surgery*, vol. 51, no. 5, pp. 1124–1132, 2010, doi: 10.1016/j.jvs.2009.12.020.
- [30] P. M. Rothwell *et al.*, ‘Analysis of pooled data from the randomised controlled trials of endarterectomy for symptomatic carotid stenosis’, *Lancet*, vol. 361, no. 9352, pp. 107–116, Jan. 2003, doi: 10.1016/S0140-6736(03)12228-3.
- [31] P. L. Allan, ‘The Carotid and Vertebral Arteries; Transcranial Colour Doppler’, *Radiology Key*, Mar. 2016. <https://radiologykey.com/the-carotid-and-vertebral-arteries-transcranial-colour-doppler/>
- [32] T. G. Brott *et al.*, ‘Stenting versus Endarterectomy for Treatment of Carotid-Artery Stenosis’, *New England Journal of Medicine*, vol. 363, no. 1, pp. 11–23, Jul. 2010, doi: 10.1056/nejmoa0912321.
- [33] A. Halliday and J. W. Norris, ‘Carotid artery stenosis’, *BMJ (Online)*, vol. 340, no. 7744, p. 431, Feb. 2010, doi: 10.1136/bmj.c748.
- [34] J. D. Spence, ‘Comment’, *The Lancet Neurology*, vol. 20, Mar. 2021.
- [35] D. D. De Waard, D. Morris, G. J. De Borst, R. Bulbulia, and A. Halliday, ‘Asymptomatic carotid artery stenosis: Who should be screened, who should be treated and how should we treat them?’, *Journal of Cardiovascular Surgery*, vol. 58, no. 1, pp. 3–12, 2017, doi: 10.23736/S0021-9509.16.09770-6.
- [36] X. Kan *et al.*, ‘Carotid artery stenting versus carotid endarterectomy in the treatment of symptomatic and asymptomatic carotid stenosis: a systematic review and meta-analysis’, *Journal of Interventional Medicine*, vol. 1, no. 1, pp. 42–48, 2018, doi: 10.19779/j.cnki.2096-3602.2018.01.09.
- [37] D. P. J. Howard, L. Gaziano, and P. M. Rothwell, ‘Risk of stroke in relation to degree of asymptomatic carotid stenosis: a population-based cohort study, systematic review, and meta-analysis’, *The Lancet Neurology*, vol. 20, no. 3, pp. 193–202, Mar. 2021, doi: 10.1016/S1474-4422(20)30484-1.
- [38] L. Saba *et al.*, ‘Carotid intraplaque-hemorrhage volume and its association with cerebrovascular events’, *American Journal of Neuroradiology*, vol. 40, no. 10, pp. 1731–1737, 2019, doi: 10.3174/ajnr.A6189.
- [39] G. Zhu *et al.*, ‘Carotid plaque imaging and the risk of atherosclerotic cardiovascular disease’, *Cardiovasc Diagn Ther*, vol. 10, no. 4, pp. 1048–1067, Aug. 2020, doi: 10.21037/cdt.2020.03.10.
- [40] J. K. Lovett, P. J. Gallagher, L. J. Hands, J. Walton, and P. M. Rothwell, ‘Histological correlates of carotid plaque surface morphology on lumen contrast imaging’, *Circulation*, vol. 110, no. 15, pp. 2190–2197, Oct. 2004, doi: 10.1161/01.CIR.0000144307.82502.32.
- [41] M. Higashi, N. Yamada, C. Yutani, H. Ishibashi-Ueda, K. Iihara, and H. Naito, ‘CT-pathologic correlation of non-calcified atherosclerotic arterial plaques: a study using carotid endarterectomy specimens’, *Br J Radiol*, vol. 93, pp. 20190901, 2022.
- [42] A. V. Finn, M. Nakano, J. Narula, F. D. Kolodgie, and R. Virmani, ‘Concept of vulnerable/unstable plaque’, *Arteriosclerosis, Thrombosis, and Vascular Biology*, vol. 30, no. 7, pp. 1282–1292, Jul. 2010, doi: 10.1161/ATVBAHA.108.179739.

- [43] T. Hishikawa, K. Iihara, N. Yamada, H. Ishibashi-Ueda, and S. Miyamoto, ‘Assessment of necrotic core with intraplaque hemorrhage in atherosclerotic carotid artery plaque by MR imaging with 3D gradient-echo sequence in patients with high-grade stenosis: Clinical article’, *Journal of Neurosurgery*, vol. 113, no. 4, pp. 890–896, 2010, doi: 10.3171/2010.3.JNS091057.
- [44] A. Kelly-Arnold, N. Maldonado, D. Laudier, E. Aikawa, L. Cardoso, and S. Weinbaum, ‘Revised microcalcification hypothesis for fibrous cap rupture in human coronary arteries’, *Proc. Natl. Acad. Sci. U.S.A.*, vol. 110, no. 26, pp. 10741–10746, Jun. 2013, doi: 10.1073/pnas.1308814110.
- [45] J. M. Davaine *et al.*, ‘Osteoprotegerin, pericytes and bone-like vascular calcification are associated with carotid plaque stability’, *PLoS ONE*, vol. 9, no. 9, Sep. 2014, doi: 10.1371/journal.pone.0107642.
- [46] T. Funaki, K. Iihara, S. Miyamoto, K. Nagatsuka, T. Hishikawa, and H. Ishibashi-Ueda, ‘Histologic characterization of mobile and nonmobile carotid plaques detected with ultrasound imaging’, *Journal of Vascular Surgery*, vol. 53, no. 4, pp. 977–983, Apr. 2011, doi: 10.1016/j.jvs.2010.10.105.
- [47] R. Naylor *et al.*, ‘Editor’s Choice – European Society for Vascular Surgery (ESVS) 2023 Clinical Practice Guidelines on the Management of Atherosclerotic Carotid and Vertebral Artery Disease’, *European Journal of Vascular and Endovascular Surgery*, vol. 65, no. 1, pp. 7–111, Jan. 2023, doi: 10.1016/j.ejvs.2022.04.011.
- [48] E. Karlöf *et al.*, ‘Carotid Plaque Phenotyping by Correlating Plaque Morphology from Computed Tomography Angiography with Transcriptional Profiling’, *European Journal of Vascular and Endovascular Surgery*, vol. 62, no. 5, pp. 716–726, Nov. 2021, doi: 10.1016/j.ejvs.2021.07.011.
- [49] H. C. Stary, ‘Natural History and Histological Classification of Atherosclerotic Lesions: An Update’, *ATVB*, vol. 20, no. 5, pp. 1177–1178, May 2000, doi: 10.1161/01.ATV.20.5.1177.
- [50] H. J. M. Barnett *et al.*, ‘Beneficial effect of carotid endarterectomy in symptomatic patients with highgrade carotid stenosis’, *N Engl J Med.*, vol. 325, no. 7, pp. 445–453, Aug. 1991, doi: 10.1056/NEJM199108153250701.
- [51] ECST, ‘Randomised trial of endarterectomy for recently symptomatic carotid stenosis: final results of the MRC European Carotid Surgery Trial (ECST).’, *Lancet*, vol. 351, no. 9113, pp. 1379–1387, May 1998.
- [52] W. K. Ly and R. Sztajzel, ‘Ultrasonographic assessment of the morphological characteristics of the carotid plaque’, *SMW*, vol. 135, no. 43–44, pp. 635–643, 2005, doi: 10.4414/smw.2005.11038.
- [53] G. L. ten Kate *et al.*, ‘Noninvasive Imaging of the Vulnerable Atherosclerotic Plaque’, *Current Problems in Cardiology*, vol. 35, no. 11, pp. 556–591, Nov. 2010, doi: 10.1016/j.cpcardiol.2010.09.002.
- [54] L. Saba *et al.*, ‘State-of-the-art CT and MR imaging and assessment of atherosclerotic carotid artery disease: standardization of scanning protocols and measurements—a consensus document by the European Society of Cardiovascular Radiology (ESCR)’, *Eur Radiol*, vol. 33, no. 2, pp. 1063–1087, Oct. 2022, doi: 10.1007/s00330-022-09024-7.

- [55] D. Valchkova Lukanova, N. Krasimirov Nikolov, K. Zaharieva Genova, M. Draganov Stankev, and E. Valcheva Georgieva, 'The accuracy of noninvasive imaging techniques in diagnosis of carotid plaque morphology', *Open Access Macedonian Journal of Medical Sciences*, vol. 3, no. 2, pp. 224–230, 2015, doi: 10.3889/oamjms.2015.039.
- [56] M. Ajduk *et al.*, 'Comparison of multidetector-row computed tomography and duplex Doppler ultrasonography in detecting atherosclerotic carotid plaques complicated with intraplaque hemorrhage.', *Coll Antropol*, vol. 37, no. 1, pp. 213–219, Mar. 2013.
- [57] Y. Watanabe *et al.*, 'Characterization of atherosclerotic plaque of carotid arteries with histopathological correlation: Vascular wall MR imaging vs. color Doppler ultrasonography (US)', *Journal of Magnetic Resonance Imaging*, vol. 28, no. 2, pp. 478–485, Aug. 2008, doi: 10.1002/jmri.21250.
- [58] T. Elatrozy, A. Nicolaides, T. Tegos, and M. Griffin, 'The objective characterisation of ultrasonic carotid plaque features', *European Journal of Vascular and Endovascular Surgery*, vol. 16, no. 3, pp. 223–230, Sep. 1998, doi: 10.1016/S1078-5884(98)80224-4.
- [59] N. M. El-Barghouty, T. Levine, S. Ladva, A. Flanagan, and A. Nicolaides, 'Histological verification of computerised carotid plaque characterisation', *European Journal of Vascular and Endovascular Surgery*, vol. 11, no. 4, pp. 414–416, May 1996, doi: 10.1016/S1078-5884(96)80172-9.
- [60] I. Gonçalves *et al.*, 'Echoluency of carotid plaques correlates with plaque cellularity', *European Journal of Vascular and Endovascular Surgery*, vol. 26, no. 1, pp. 32–38, Jul. 2003, doi: 10.1053/ejvs.2002.1907.
- [61] A. M. Johri *et al.*, 'Recommendations for the Assessment of Carotid Arterial Plaque by Ultrasound for the Characterization of Atherosclerosis and Evaluation of Cardiovascular Risk: From the American Society of Echocardiography', *Journal of the American Society of Echocardiography*, vol. 33, no. 8, pp. 917–933, Aug. 2020, doi: 10.1016/j.echo.2020.04.021.
- [62] D. Staub *et al.*, 'Vasa Vasorum and Plaque Neovascularization on Contrast-Enhanced Carotid Ultrasound Imaging Correlates With Cardiovascular Disease and Past Cardiovascular Events', *Stroke*, vol. 41, no. 1, pp. 41–47, Jan. 2010, doi: 10.1161/STROKEAHA.109.560342.
- [63] A. Ebrahimi, J. Scott, and K. Ghorbani, 'Microwave reflective biosensor for glucose level detection in aqueous solutions', *Sensors and Actuators, A: Physical*, vol. 301, Jan. 2020, doi: 10.1016/j.sna.2019.111662.
- [64] C. C. Mitchell *et al.*, 'Histopathologic Validation of Grayscale Carotid Plaque Characteristics Related to Plaque Vulnerability', *Ultrasound in medicine & biology*, vol. 43, no. 1, pp. 129–137, Jan. 2017, doi: 10.1016/J.ULTRASMEDBIO.2016.08.011.
- [65] T. D. DenOtter and J. Schubert, 'Hounsfield Unit.', in *StatPearls*, Treasure Island (FL): StatPearls Publishing, 2022.
- [66] E. Choi *et al.*, 'Carotid plaque composition assessed by CT predicts subsequent cardiovascular events among subjects with carotid stenosis', *American Journal of Neuroradiology*, vol. 42, no. 12, pp. 2199–2206, Dec. 2021, doi: 10.3174/ajnr.A7338.
- [67] T. T. Weert *et al.*, 'Assessment of atherosclerotic carotid plaque volume with multidetector computed tomography angiography', *International Journal of*

- Cardiovascular Imaging*, vol. 24, no. 7, pp. 751–759, 2008, doi: 10.1007/s10554-008-9309-1.
- [68] L. Saba *et al.*, ‘Relationship between Carotid Computed Tomography Dual-Energy and Brain Leukoaraiosis’, *Journal of Stroke and Cerebrovascular Diseases*, vol. 26, no. 8, pp. 1824–1830, Aug. 2017, doi: 10.1016/j.jstrokecerebrovasdis.2017.04.016.
- [69] W. Kristanto, P. M. A. van Ooijen, M. C. Jansen-van der Weide, R. Vliegenthart, and M. Oudkerk, ‘A Meta Analysis and Hierarchical Classification of HU-Based Atherosclerotic Plaque Characterization Criteria’, *PLoS ONE*, vol. 8, no. 9, p. e73460, Sep. 2013, doi: 10.1371/journal.pone.0073460.
- [70] E. K. Oikonomou *et al.*, ‘Non-invasive detection of coronary inflammation using computed tomography and prediction of residual cardiovascular risk (the CRISP CT study): a post-hoc analysis of prospective outcome data’, *The Lancet*, vol. 392, no. 10151, pp. 929–939, Sep. 2018, doi: 10.1016/S0140-6736(18)31114-0.
- [71] J. T. Sun *et al.*, ‘Pericoronary Fat Attenuation Index Is Associated With Vulnerable Plaque Components and Local Immune-Inflammatory Activation in Patients With Non-ST Elevation Acute Coronary Syndrome.’, *J Am Heart Assoc*, vol. 11, no. 2, p. e022879, Jan. 2022, doi: 10.1161/JAHA.121.022879.
- [72] D. Chatterjee *et al.*, ‘Perivascular fat attenuation for predicting adverse cardiac events in stable patients undergoing invasive coronary angiography.’, *J Cardiovasc Comput Tomogr*, vol. 16, no. 6, pp. 483–490, Dec. 2022, doi: 10.1016/j.jcct.2022.05.004.
- [73] A. S. Antonopoulos *et al.*, ‘Detecting human coronary inflammation by imaging perivascular fat.’, *Sci Transl Med*, vol. 9, no. 398, p. eaal2658, Jul. 2017, doi: 10.1126/scitranslmed.aal2658.
- [74] H. Baradaran *et al.*, ‘Association between carotid artery perivascular fat density and cerebrovascular ischemic events’, *Journal of the American Heart Association*, vol. 7, no. 24, Dec. 2018, doi: 10.1161/JAHA.118.010383.
- [75] K. Misaki, N. Uchiyama, M. Mohri, and M. Nakada, ‘Carotid Artery Plaque Diagnosis Using CT’, *NOUSHINKEI KEKKANNAI TIRYOU*, vol. 12, no. 12, pp. 592–596, 2018, doi: 10.5797/jnet.ra.2018-0052.
- [76] M. Garg *et al.*, ‘Radiation Exposure and Lifetime Attributable Risk of Cancer Incidence and Mortality from Low- and Standard-Dose CT Chest: Implications for COVID-19 Pneumonia Subjects’, *Diagnostics*, vol. 12, no. 12, Dec. 2022, doi: 10.3390/diagnostics12123043.
- [77] A. J. Patterson *et al.*, ‘Association between White Matter Ischaemia and Carotid Plaque Morphology as Defined by High-resolution In Vivo MRI’, *European Journal of Vascular and Endovascular Surgery*, vol. 38, no. 2, pp. 149–154, Aug. 2009, doi: 10.1016/j.ejvs.2009.04.005.
- [78] K. Skagen *et al.*, ‘Carotid Plaque Inflammation Assessed with F-FDG PET/CT is Higher in Symptomatic Compared with Asymptomatic Patients’, *International Journal of Stroke*, vol. 10, no. 5, pp. 730–736, Jul. 2015, doi: 10.1111/ijvs.12430.
- [79] R. Y. Khamis *et al.*, ‘Near Infrared Fluorescence (NIRF) Molecular Imaging of Oxidized LDL with an Autoantibody in Experimental Atherosclerosis’, *Sci Rep*, vol. 6, no. 1, p. 21785, Feb. 2016, doi: 10.1038/srep21785.

- [80] B. Modarai *et al.*, ‘European Society for Vascular Surgery (ESVS) 2023 Clinical Practice Guidelines on Radiation Safety’, *European Journal of Vascular and Endovascular Surgery*, Feb. 2023, doi: 10.1016/j.ejvs.2022.09.005.
- [81] N. Horie *et al.*, ‘Communication of inwardly projecting neovessels with the lumen contributes to symptomatic intraplaque hemorrhage in carotid artery stenosis’, *Journal of Neurosurgery*, vol. 123, no. 5, pp. 1125–1132, Nov. 2015, doi: 10.3171/2014.12.JNS142371.
- [82] M. Cattaneo *et al.*, ‘Imaging of Carotid Plaque Neovascularization by Contrast-Enhanced Ultrasound and Dynamic Contrast-Enhanced Magnetic Resonance Imaging’, *Cerebrovascular Diseases*, vol. 48, no. 3–6, pp. 140–148, 2019, doi: 10.1159/000504042.
- [83] L. Xiong, Y.-B. Deng, Y. Zhu, Y.-N. Liu, and X.-J. Bi, ‘Correlation of Carotid Plaque Neovascularization Detected by Using Contrast-enhanced US with Clinical Symptoms’, *Radiology*, vol. 251, no. 2, pp. 583–589, May 2009, doi: 10.1148/radiol.2512081829.
- [84] Y. Wang, T. Wang, Y. Luo, and L. Jiao, ‘Identification Markers of Carotid Vulnerable Plaques: An Update’, *Biomolecules*, vol. 12, no. 9, p. 1192, Aug. 2022, doi: 10.3390/biom12091192.
- [85] E. Ammirati, F. Moroni, G. D. Norata, M. Magnoni, and P. G. Camici, ‘Markers of Inflammation Associated with Plaque Progression and Instability in Patients with Carotid Atherosclerosis’, *Mediators of Inflammation*, vol. 2015, pp. 1–15, 2015, doi: 10.1155/2015/718329.
- [86] M. F. Heymann *et al.*, ‘Role of the OPG/RANK/RANKL triad in calcifications of the atheromatous plaques: Comparison between carotid and femoral beds’, *Cytokine*, vol. 58, no. 2, pp. 300–306, May 2012, doi: 10.1016/j.cyto.2012.02.004.
- [87] E. Martinez, J. Martorell, and V. Riambau, ‘Review of serum biomarkers in carotid atherosclerosis’, *Journal of Vascular Surgery*, vol. 71, no. 1, pp. 329–341, Jan. 2020, doi: 10.1016/j.jvs.2019.04.488.
- [88] M. Reiter *et al.*, ‘Plaque imaging of the internal carotid artery - correlation of B-flow imaging with histopathology.’, *AJNR Am J Neuroradiol*, vol. 28, no. 1, pp. 122–126, Jan. 2007.
- [89] L. L. Kingstone *et al.*, ‘Advanced Ultrasound Evaluation of Vulnerable Carotid Artery Plaque: Can a Combined Two-dimensional and Three-dimensional Plaque Imaging Analysis Identify Significant Plaque Characteristics Responsible for Strokes? A Case Series Study’, *Journal of Medical Imaging and Radiation Sciences*, vol. 45, no. 4, pp. 440–447, Dec. 2014, doi: 10.1016/J.JMIR.2014.04.005.
- [90] L. Saba *et al.*, ‘Review of imaging biomarkers for the vulnerable carotid plaque’, *JVS-Vascular Science*, vol. 2, pp. 149–158, Jan. 2021, doi: 10.1016/j.jvssci.2021.03.001.
- [91] A. W. Guy, ‘History of Biological Effects and Medical Applications of Microwave Energy’, *IEEE Transactions on Microwave Theory and Techniques*, vol. 32, no. 9, pp. 1182–1200, 1984, doi: 10.1109/TMTT.1984.1132830.
- [92] A. Joisel *et al.*, ‘Microwave imaging techniques for biomedical applications’, in *IMTC/99. Proceedings of the 16th IEEE Instrumentation and Measurement Technology Conference (Cat. No.99CH36309)*, Venice, Italy: IEEE, 1999, pp. 1591–1596. doi: 10.1109/IMTC.1999.776093.

- [93] R. Chandra, H. Zhou, I. Balasingham, and R. M. Narayanan, 'On the Opportunities and Challenges in Microwave Medical Sensing and Imaging', *IEEE Transactions on Biomedical Engineering*, vol. 62, no. 7, pp. 1667–1682, Jul. 2015, doi: 10.1109/TBME.2015.2432137.
- [94] A. Davis, 'How Marie Curie Helped Save a Million Soldiers During World War I - IEEE Spectrum', *IEEE Spectrum*, Feb. 01, 2016. <https://spectrum.ieee.org/how-marie-curie-helped-save-a-million-soldiers-during-world-war-i>
- [95] R. V. Leslie, 'Microwave Sensors', in *Comprehensive Remote Sensing*, Elsevier, 2018, pp. 435–474. doi: 10.1016/B978-0-12-409548-9.10328-8.
- [96] WHO TEAM, 'Radiation: Electromagnetic fields', *W.H.O. Q&A*, Aug. 2016, [Online]. Available: <https://www.who.int/news-room/questions-and-answers/item/radiation-electromagnetic-fields>
- [97] Z. Izadifar, Z. Izadifar, D. Chapman, and P. Babyn, 'An Introduction to High Intensity Focused Ultrasound: Systematic Review on Principles, Devices, and Clinical Applications', *JCM*, vol. 9, no. 2, p. 460, Feb. 2020, doi: 10.3390/jcm9020460.
- [98] Y. Yang, Z. Xia, H. Xia, Y. Li, G. Liu, and J. Xu, 'Applied current thermoacoustic imaging for biological tissues', *THC*, vol. 28, pp. 57–65, Jun. 2020, doi: 10.3233/THC-209007.
- [99] J. Li, Z. Wu, C. Peng, L. Song, and Y. Luo, 'Microwave-induced thermoacoustic imaging for the early detection of canine intracerebral hemorrhage', *Front. Physiol.*, vol. 13, p. 1067948, Nov. 2022, doi: 10.3389/fphys.2022.1067948.
- [100] H. Zhang, M. Ren, S. Zhang, J. Liu, and H. Qin, 'Microwave-induced thermoacoustic imaging for biomedical applications', *Phys. Scr.*, vol. 98, no. 3, p. 032001, Mar. 2023, doi: 10.1088/1402-4896/acbc55.
- [101] M. Soltani, R. Rahpeima, and F. M. Kashkooli, 'Breast cancer diagnosis with a microwave thermoacoustic imaging technique—a numerical approach', *Med Biol Eng Comput*, vol. 57, no. 7, pp. 1497–1513, Jul. 2019, doi: 10.1007/s11517-019-01961-8.
- [102] A. R. Buchberger, K. DeLaney, J. Johnson, and L. Li, 'Mass Spectrometry Imaging: A Review of Emerging Advancements and Future Insights', *Anal. Chem.*, vol. 90, no. 1, pp. 240–265, Jan. 2018, doi: 10.1021/acs.analchem.7b04733.
- [103] J. G. Fujimoto, C. Pitris, S. A. Boppart, and M. E. Brezinski, 'Optical Coherence Tomography: An Emerging Technology for Biomedical Imaging and Optical Biopsy', *Neoplasia*, vol. 2, no. 1–2, pp. 9–25, Jan. 2000, doi: 10.1038/sj.neo.7900071.
- [104] G. Ku, B. D. Fornage, X. Jin, M. Xu, K. K. Hunt, and L. V. Wang, 'Thermoacoustic and photoacoustic tomography of thick biological tissues toward breast imaging.', *Technol Cancer Res Treat*, vol. 4, no. 5, pp. 559–566, Oct. 2005, doi: 10.1177/153303460500400509.
- [105] J. Xia, J. Yao, and L. V. Wang, 'Photoacoustic tomography: principles and advances', *NIH Public Access*, vol. 147, pp. 1–22, 2015.
- [106] A. E. Adeoye, E. Ajenifuja, B. A. Taleatu, and A. Y. Fasasi, 'Rutherford Backscattering Spectrometry Analysis and Structural Properties of Zn x Pb 1 - x S Thin Films Deposited by Chemical Spray Pyrolysis', *Journal of Materials*, vol. 2015, pp. 1–8, Oct. 2015, doi: 10.1155/2015/215210.

- [107] C. Jeynes and J. L. Colaux, ‘Thin film depth profiling by ion beam analysis’, *Analyst*, vol. 141, no. 21, pp. 5944–5985, 2016, doi: 10.1039/C6AN01167E.
- [108] S. Krishnamoorthy, J. H. Reed, C. R. Anderson, P. M. Robert, and S. Srikanteswara, ‘Characterization of the 2.4 GHz ISM Band Electromagnetic Interference in a Hospital Environment’, in *Annual International Conference of the IEEE Engineering in Medicine and Biology - Proceedings*, 2003, pp. 3245–3248. doi: 10.1109/iembs.2003.1280835.
- [109] M. Persson *et al.*, ‘Microwave-based stroke diagnosis making global prehospital thrombolytic treatment possible’, *IEEE Transactions on Biomedical Engineering*, vol. 61, no. 11, pp. 2806–2817, Nov. 2014, doi: 10.1109/TBME.2014.2330554.
- [110] F. Sterzer, ‘Microwave medical devices’, *IEEE Microwave Magazine*, vol. 3, no. 1, pp. 65–70, Mar. 2002, doi: 10.1109/6668.990689.
- [111] Y. Kozhemyakin, S. Rehault-Godbert, D. Dubuc, and K. Grenier, ‘Millifluidic Sensor Designed to Perform the Microwave Dielectric Spectroscopy of Biological Liquids’, in *2022 52nd European Microwave Conference, EuMC 2022*, Institute of Electrical and Electronics Engineers Inc., 2022, pp. 412–415. doi: 10.23919/EuMC54642.2022.9924355.
- [112] M. Maffongelli *et al.*, ‘Design and Experimental Test of a Microwave System for Quantitative Biomedical Imaging’, in *MeMeA 2018 - 2018 IEEE International Symposium on Medical Measurements and Applications, Proceedings*, Institute of Electrical and Electronics Engineers Inc., Aug. 2018. doi: 10.1109/MeMeA.2018.8438599.
- [113] S. A. Rezaeieh, K. S. Bialkowski, and A. M. Abbosh, ‘Microwave system for the early stage detection of congestive heart failure’, *IEEE Access*, vol. 2, pp. 921–929, 2014, doi: 10.1109/ACCESS.2014.2352614.
- [114] B. Amin, A. Shahzad, M. O’Halloran, B. McDermott, and A. Elahi, ‘Experimental Validation of Microwave Imaging Prototype and DBIM-IMATCS Algorithm for Bone Health Monitoring’, *IEEE Access*, vol. 10, pp. 42589–42600, 2022, doi: 10.1109/ACCESS.2022.3167715.
- [115] F. Deshours *et al.*, ‘Improved microwave biosensor for non-invasive dielectric characterization of biological tissues’, *Microelectronics Journal*, vol. 88, pp. 137–144, Jun. 2019, doi: 10.1016/j.mejo.2018.01.027.
- [116] R. M. Irastorza, E. Blangino, C. M. Carlevaro, and F. Vericat, ‘Modeling of the dielectric properties of trabecular bone samples at microwave frequency’, *Medical and Biological Engineering and Computing*, vol. 52, no. 5, pp. 439–447, 2014, doi: 10.1007/s11517-014-1145-y.
- [117] I. B. Vendik *et al.*, ‘Diagnostics of osteoporosis based on analysis of electromagnetic wave propagation in biological objects’, in *Proceedings of the 2019 Antennas Design and Measurement International Conference, ADMInC 2019*, Institute of Electrical and Electronics Engineers Inc., Oct. 2019, pp. 58–61. doi: 10.1109/ADMInC47948.2019.8969252.
- [118] M. Calvet-Chautard, P. J. Gonzalez, T. Veronese, D. Dubuc, and K. Grenier, ‘Microwave-Based Sensor Dedicated to the Characterization of Meat Freshness’, in *2020 IEEE MTT-S International Microwave Biomedical Conference, IMBioC 2020*, Institute

- of Electrical and Electronics Engineers Inc., Dec. 2020. doi: 10.1109/IMBIOc47321.2020.9385050.
- [119] M. Lazebnik *et al.*, ‘A large-scale study of the ultrawideband microwave dielectric properties of normal breast tissue obtained from reduction surgeries’, *Physics in Medicine and Biology*, vol. 52, no. 10, May 2007, doi: 10.1088/0031-9155/52/10/001.
- [120] A. Zamani, S. Ahdi Rezaeieh, K. S. Bialkowski, and A. M. Abbosh, ‘Boundary Estimation of Imaged Object in Microwave Medical Imaging Using Antenna Resonant Frequency Shift’, *IEEE Transactions on Antennas and Propagation*, vol. 66, no. 2, pp. 927–936, Feb. 2018, doi: 10.1109/TAP.2017.2780898.
- [121] L. Kranold, M. Taherzadeh, F. Nabki, M. Coates, and M. Popovic, ‘Microwave Breast Screening Prototype: System Miniaturization with IC Pulse Radio’, *IEEE Journal of Electromagnetics, RF and Microwaves in Medicine and Biology*, vol. 5, no. 2, pp. 168–178, Jun. 2021, doi: 10.1109/JERM.2020.3029214.
- [122] P. M. Meaney, A. P. Gregory, J. Seppala, and T. Lahtinen, ‘Open-Ended Coaxial Dielectric Probe Effective Penetration Depth Determination’, *IEEE Transactions on Microwave Theory and Techniques*, vol. 64, no. 3, pp. 915–923, Mar. 2016, doi: 10.1109/TMTT.2016.2519027.
- [123] P. M. Meaney *et al.*, ‘Clinical microwave tomographic imaging of the calcaneus: A first-in-human case study of two subjects’, *IEEE Transactions on Biomedical Engineering*, vol. 59, no. 12, pp. 3304–3313, 2012, doi: 10.1109/TBME.2012.2209202.
- [124] M. A. Aldhaeabi, K. Alzoubi, T. S. Almoneef, S. M. Bamatra, H. Attia, and O. M. Ramahi, ‘Review of microwaves techniques for breast cancer detection’, *Sensors (Switzerland)*, vol. 20, no. 8, Apr. 2020, doi: 10.3390/s20082390.
- [125] A. Matković, A. Kordić, A. Jakovčević, and A. Šarolić, ‘Complex Permittivity of Ex-Vivo Human, Bovine and Porcine Brain Tissues in the Microwave Frequency Range’, *Diagnostics*, vol. 12, no. 11, Nov. 2022, doi: 10.3390/diagnostics12112580.
- [126] J. Ljungqvist, S. Candefjord, M. Persson, L. Jönsson, T. Skoglund, and M. Elam, ‘Clinical Evaluation of a Microwave-Based Device for Detection of Traumatic Intracranial Hemorrhage’, *Journal of Neurotrauma*, vol. 34, no. 13, pp. 2176–2182, Jul. 2017, doi: 10.1089/neu.2016.4869.
- [127] A. Fhager and M. Persson, ‘A microwave measurement system for stroke detection’, in *LAPC 2011 - 2011 Loughborough Antennas and Propagation Conference*, 2011. doi: 10.1109/LAPC.2011.6114001.
- [128] A. Fhager, T. Mckelvey, and M. Persson, ‘Stroke Detection Using a Broadband Microwave Antenna System’, in *Proceedings of the Fourth European Conference on Antennas and Propagation*, Barcelona, Spain, 2010, pp. 1–3. [Online]. Available: www.vardalinstitutet.net
- [129] A. K. Martusevich, V. V. Nazarov, A. V. Surovegina, and A. V. Novikov, ‘Near-Field Microwave Tomography of Biological Tissues: Future Perspectives’, 2022. [Online]. Available: www.begellhouse.com
- [130] M. Drakopoulou, C. Moldovan, K. Toutouzas, and D. Tousoulis, ‘The role of microwave radiometry in carotid artery disease. Diagnostic and clinical prospective’, *Current Opinion in Pharmacology*, vol. 39, pp. 99–104, Apr. 2018, doi: 10.1016/j.coph.2018.02.008.

- [131] A. Saxena, V. Saha, and E. Y. K. Ng, ‘Skin temperature maps as a measure of carotid artery stenosis’, *Computers in Biology and Medicine*, vol. 116, Jan. 2020, doi: 10.1016/j.compbimed.2019.103548.
- [132] H. Y. Mesri, M. K. Najafabadi, and T. McKelvey, ‘A multidimensional signal processing approach for classification of microwave measurements with application to stroke type diagnosis’, in *Proceedings of the Annual International Conference of the IEEE Engineering in Medicine and Biology Society, EMBS*, 2011, pp. 6465–6469. doi: 10.1109/IEMBS.2011.6091596.
- [133] A. Hossain *et al.*, ‘Microwave brain imaging system to detect brain tumor using metamaterial loaded stacked antenna array’, *Scientific Reports*, vol. 12, no. 1, Dec. 2022, doi: 10.1038/s41598-022-20944-8.
- [134] P. K. B. Rangaiah *et al.*, ‘Dielectric Characterization and Statistical Analysis of Ex-Vivo Burnt Human Skin Samples For Microwave Sensor Development’, 2022, doi: 10.21203/rs.3.rs-1745760/v1.
- [135] Y. Feldman *et al.*, ‘The electromagnetic response of human skin in the millimetre and submillimetre wave range’, *Physics in Medicine and Biology*, vol. 54, no. 11, pp. 3341–3363, 2009, doi: 10.1088/0031-9155/54/11/005.
- [136] S. R. Mohd Shah *et al.*, ‘Analysis of Thickness Variation in Biological Tissues Using Microwave Sensors for Health Monitoring Applications’, *IEEE Access*, vol. 7, pp. 156033–156043, 2019, doi: 10.1109/ACCESS.2019.2949179.
- [137] N. B. Asan *et al.*, ‘Characterization of the fat channel for intra-body communication at R-Band frequencies’, *Sensors (Switzerland)*, vol. 18, no. 9, Sep. 2018, doi: 10.3390/s18092752.
- [138] M. D. Perez *et al.*, ‘Microwave Sensors for New Approach in Monitoring Hip Fracture Healing’, in *2017 11th European Conference On Antennas And Propagation (EUCAP)* ;, in Proceedings of the European Conference on Antennas and Propagation. IEEE, 2017, pp. 1838–1842. [Online]. Available: <http://ieeexplore.ieee.org/document/7928698/>
- [139] J. Griffith *et al.*, ‘Non-invasive electromagnetic skin patch sensor to measure intracranial fluid-volume shifts’, *Sensors (Switzerland)*, vol. 18, no. 4, Apr. 2018, doi: 10.3390/s18041022.
- [140] F. Alruwaili, K. Cluff, J. Griffith, and H. Farhoud, ‘Passive self resonant skin patch sensor to monitor cardiac intraventricular stroke volume using electromagnetic properties of blood’, *IEEE Journal of Translational Engineering in Health and Medicine*, vol. 6, 2018, doi: 10.1109/JTEHM.2018.2870589.
- [141] K. Cluff *et al.*, ‘Passive Wearable Skin Patch Sensor Measures Limb Hemodynamics Based on Electromagnetic Resonance’, *IEEE Transactions on Biomedical Engineering*, vol. 65, no. 4, pp. 847–856, Apr. 2018, doi: 10.1109/TBME.2017.2723001.
- [142] B. Amin *et al.*, ‘Dielectric characterization of diseased human trabecular bones at microwave frequency’, *Medical Engineering and Physics*, vol. 78, pp. 21–28, Apr. 2020, doi: 10.1016/j.medengphy.2020.01.014.
- [143] H. Choi, S. Luzio, J. Beutler, and A. Porch, ‘Microwave noninvasive blood glucose monitoring sensor: Human clinical trial results’, in *2017 IEEE MTT-S International Microwave Symposium (IMS)*, Honolulu, HI, USA: IEEE, Jun. 2017, pp. 876–879. doi: 10.1109/MWSYM.2017.8058721.

- [144] M. Baghelani, Z. Abbasi, M. Daneshmand, and P. E. Light, ‘Non-invasive continuous-time glucose monitoring system using a chipless printable sensor based on split ring microwave resonators’, *Scientific Reports*, vol. 10, no. 1, Dec. 2020, doi: 10.1038/s41598-020-69547-1.
- [145] Q. Xue, Z. Li, Q. Wang, W. Pan, Y. Chang, and X. Duan, ‘Nanostrip flexible microwave enzymatic biosensor for noninvasive epidermal glucose sensing’, *Nanoscale Horizons*, vol. 5, no. 6, pp. 934–943, Jun. 2020, doi: 10.1039/D0NH00098A.
- [146] A. E. Omer *et al.*, ‘Low-cost portable microwave sensor for non-invasive monitoring of blood glucose level: novel design utilizing a four-cell CSRR hexagonal configuration’, *Scientific Reports*, vol. 10, no. 1, Dec. 2020, doi: 10.1038/s41598-020-72114-3.
- [147] K. Abdesselam *et al.*, ‘A Non-Invasive Honey-Cell CSRR Glucose Sensor: Design Considerations and Modelling’, *IRBM*, vol. 44, no. 1, p. 100713, Feb. 2023, doi: 10.1016/j.irbm.2022.04.002.
- [148] M. Farooq *et al.*, ‘An Ex Vivo Study of Wireless Linkage Distance between Implantable LC Resonance Sensor and External Readout Coil’, *Sensors*, vol. 22, no. 21, Nov. 2022, doi: 10.3390/s22218402.
- [149] I. B. Vendik *et al.*, ‘Wireless monitoring of the biological object state at microwave frequencies: A review’, *Technical Physics*, vol. 61, no. 1, pp. 1–22, Jan. 2016, doi: 10.1134/S1063784216010242.
- [150] S. Vogt *et al.*, ‘A Newly Developed mm-Wave Sensor for Detecting Plaques of Arterial Vessels’, *Thoracic and Cardiovascular Surgeon*, vol. 66, no. 1, pp. 91–98, Jan. 2018, doi: 10.1055/s-0037-1606318.
- [151] D. Wagner *et al.*, ‘Packaging of a BiCMOS Sensor on a catheter tip for the characterisation of atherosclerotic plaque’, in *2016 6th Electronic System-Integration Technology Conference, ESTC 2016*, Institute of Electrical and Electronics Engineers Inc., Dec. 2016. doi: 10.1109/ESTC.2016.7764497.
- [152] Keysight Technologies, ‘Basics of Measuring the Dielectric Properties of Materials’. [Online]. Available: www.keysight.com
- [153] A. Vander, V. A. Rosen, and Y. Kotsuka, *RF/Microwave Interaction with Biological Tissues*. USA: John Wiley & Sons, Inc, 2006.
- [154] A. Shahzad, S. Khan, M. Jones, R. M. Dwyer, and M. O’Halloran, ‘Investigation of the effect of dehydration on tissue dielectric properties in ex vivo measurements’, *Biomedical Physics and Engineering Express*, vol. 3, no. 4, Jun. 2017, doi: 10.1088/2057-1976/aa74c4.
- [155] E. Porter and M. O’Halloran, ‘Investigation of Histology Region in Dielectric Measurements of Heterogeneous Tissues’, *IEEE Transactions on Antennas and Propagation*, vol. 65, no. 10, pp. 5541–5552, Oct. 2017, doi: 10.1109/TAP.2017.2741026.
- [156] P. A. Haggall *et al.*, ‘IT’IS Database for thermal and electromagnetic parameters of biological tissues V4.1’, *IT’IS Foundation*, Feb. 22, 2022. <https://itis.swiss/virtual-population/tissue-properties/>
- [157] D. Andreuccetti, R. Fossi, and C. Petrucci, ‘An Internet resource for the calculation of the dielectric properties of body tissues in the frequency range 10 Hz - 100 GHz’, *IFAC CNR*, 1997. <http://niremf.ifac.cnr.it/tissprop/#inizio>

- [158] N. Ištuk *et al.*, ‘Dielectric properties of ovine heart at microwave frequencies’, *Diagnostics*, vol. 11, no. 3, Mar. 2021, doi: 10.3390/diagnostics11030531.
- [159] C. Gabriel, S. Gabriel, and E. Corthout, ‘The dielectric properties of biological tissues: I. Literature survey’, *Physics in Medicine and Biology*, vol. 41, no. 11, pp. 2231–2249, Nov. 1996, doi: 10.1088/0031-9155/41/11/001.
- [160] K. R. Foster, J. L. Schepps, R. D. Stoy, and H. P. Schwan, ‘Dielectric properties of brain tissue between 0.01 and 10 GHz.’, *Phys Med Biol*, vol. 24, no. 6, pp. 1177–1187, Nov. 1979, doi: 10.1088/0031-9155/24/6/008.
- [161] A. Surowiec, S. S. Stuchly, L. Eidus, and A. Swarup, ‘In vitro dielectric properties of human tissues at radiofrequencies.’, *Phys Med Biol*, vol. 32, no. 5, pp. 615–621, May 1987, doi: 10.1088/0031-9155/32/5/007.
- [162] A. Peyman, A. A. Rezazadeh, and C. Gabriel, ‘Changes in the dielectric properties of rat tissue as a function of age at microwave frequencies.’, *Phys Med Biol*, vol. 46, no. 6, pp. 1617–1629, Jun. 2001, doi: 10.1088/0031-9155/46/6/303.
- [163] G. Schmid, G. Neubauer, U. M. Illievich, and F. Alesch, ‘Dielectric properties of porcine brain tissue in the transition from life to death at frequencies from 800 to 1900 MHz.’, *Bioelectromagnetics*, vol. 24, no. 6, pp. 413–422, Sep. 2003, doi: 10.1002/bem.10122.
- [164] L. Abdilla, C. Sammut, and L. Z. Mangion, ‘Dielectric properties of muscle and liver from 500 MHz-40 GHz.’, *Electromagn Biol Med*, vol. 32, no. 2, pp. 244–252, Jun. 2013, doi: 10.3109/15368378.2013.776436.
- [165] K. Sasaki, K. Wake, and S. Watanabe, ‘Measurement of the dielectric properties of the epidermis and dermis at frequencies from 0.5 GHz to 110 GHz.’, *Phys Med Biol*, vol. 59, no. 16, pp. 4739–4747, Aug. 2014, doi: 10.1088/0031-9155/59/16/4739.
- [166] M. A. Stuchly, A. Kraszewski, S. S. Stuchly, and A. M. Smith, ‘Dielectric properties of animal tissues in vivo at radio and microwave frequencies: comparison between species’, *Physics in Medicine & Biology*, vol. 27, no. 7, pp. 927–936, 1982, doi: 10.1088/0031-9155/27/7/004.
- [167] S. S. Chaudhary, R. K. Mishra, A. Swarup, and J. M. Thomas, ‘Dielectric properties of normal & malignant human breast tissues at radiowave & microwave frequencies.’, *Indian J Biochem Biophys*, vol. 21, no. 1, pp. 76–79, Feb. 1984.
- [168] A. J. Surowiec, S. S. Stuchly, J. B. Barr, and A. Swarup, ‘Dielectric properties of breast carcinoma and the surrounding tissues.’, *IEEE Trans Biomed Eng*, vol. 35, no. 4, pp. 257–263, Apr. 1988, doi: 10.1109/10.1374.
- [169] W. T. Joines, Y. Zhang, C. Li, and R. L. Jirtle, ‘The measured electrical properties of normal and malignant human tissues from 50 to 900 MHz.’, *Med Phys*, vol. 21, no. 4, pp. 547–550, Apr. 1994, doi: 10.1118/1.597312.
- [170] A. P. O’Rourke *et al.*, ‘Dielectric properties of human normal, malignant and cirrhotic liver tissue: in vivo and ex vivo measurements from 0.5 to 20 GHz using a precision open-ended coaxial probe.’, *Phys Med Biol*, vol. 52, no. 15, pp. 4707–4719, Aug. 2007, doi: 10.1088/0031-9155/52/15/022.
- [171] T. Sugitani *et al.*, ‘Erratum: “Complex permittivities of breast tumor tissues obtained from cancer surgeries” [Appl. Phys. Lett. **104**, 253702 (2014)]’, *Appl. Phys. Lett.*, vol. 107, no. 1, p. 019902, Jul. 2015, doi: 10.1063/1.4926798.

- [172] S. Salahuddin, A. La Gioia, M. Adnan Elahi, E. Porter, and A. Shahzad, 'Comparison of in-vivo and ex-vivo Dielectric Properties of Biological Tissues' *2017 International Conference on Electromagnetics in Advanced Applications (ICEAA)*, Verona, Italy, 2017, pp. 582-585, doi: 10.1109/ICEAA.2017.8065312..
- [173] S. Redzwan and R. Augustine Kachiramattom, 'Prospective Applications of Microwaves in Medicine Microwave Sensors for Orthopedic Monitoring and Burn Depth Assessment' 2019.
- [174] B. J. Klauenberg and D. Miklavčič, *Radio Frequency Radiation Dosimetry and Its Relationship to the Biological Effects of Electromagnetic Fields*, 1st ed. Springer Science & Business Media, 2000. [Online]. Available: https://books.google.com/books/about/Radio_Frequency_Radiation_Dosimetry_and.html?id=cjDpCAAAQBAJ
- [175] M. Cavagnaro, F. Frezza, R. Laurita, and M. Tannino, 'A model to evaluate dielectric properties of human tissues based on water content', in *2014 8th International Symposium on Medical Information and Communication Technology (ISMICT)*, Apr. 2014, pp. 1–5. doi: 10.1109/ISMICT.2014.6825221.
- [176] C. Gabriel, 'Dielectric properties of biological tissue: variation with age.', *Bioelectromagnetics*, vol. Suppl 7, pp. S12-18, 2005, doi: 10.1002/bem.20147.
- [177] K. R. Foster and H. P. Schwan, 'Dielectric properties of tissues and biological materials: a critical review.', *Crit Rev Biomed Eng*, vol. 17, no. 1, pp. 25–104, 1989.
- [178] R. J. Halter *et al.*, 'The correlation of in vivo and ex vivo tissue dielectric properties to validate electromagnetic breast imaging: initial clinical experience.', *Physiol Meas*, vol. 30, no. 6, pp. S121-136, Jun. 2009, doi: 10.1088/0967-3334/30/6/S08.
- [179] P. Hindle, 'Low-Priced, Full Featured VNA Comparison', *Pat Hindle, MWJ Editor*, Aug. 2022. <https://www.microwavejournal.com/blogs/9-pat-hindle-mwj-editor/post/38757-low-priced-full-featured-vna-comparison>
- [180] K. C. Yaw, 'Measurement of Dielectric Material Properties.', Rohde & Schwarz, Application Note, May 2012. [Online]. Available: https://scdn.rohde-schwarz.com/ur/pws/dl_downloads/dl_application/00aps_undefined/RAC-0607-0019_1_5E.pdf
- [181] Tektronix, 'Introduction to VNA Basics', Primer, Mar. 2017. [Online]. Available: www.tek.com
- [182] E. Porter *et al.*, 'Minimum information for dielectric measurements of biological tissues (MINDER): A framework for repeatable and reusable data', *International Journal of RF and Microwave Computer-Aided Engineering*, vol. 28, no. 3, Mar. 2018, doi: 10.1002/mmce.21201.
- [183] G. Ruvio, M. Vaselli, V. Lopresto, R. Pinto, L. Farina, and M. Cavagnaro, 'Comparison of different methods for dielectric properties measurements in liquid sample media', *International Journal of RF and Microwave Computer-Aided Engineering*, vol. 28, no. 3, p. e21215, Mar. 2018, doi: 10.1002/MMCE.21215.
- [184] A. La Gioia *et al.*, 'Open-ended coaxial probe technique for dielectric measurement of biological tissues: Challenges and common practices', *Diagnostics*, vol. 8, no. 2, Jun. 2018, doi: 10.3390/diagnostics8020040.

- [185] M. A. H. Ansari, A. K. Jha, and M. J. Akhtar, ‘Design and Application of the CSRR-Based Planar Sensor for Noninvasive Measurement of Complex Permittivity’, *IEEE Sensors J.*, vol. 15, no. 12, pp. 7181–7189, Dec. 2015, doi: 10.1109/JSEN.2015.2469683.
- [186] M. S. Venkatesh and G. S. V. Raghavan, ‘An overview of dielectric properties measuring techniques’, *Canadian Biosystems Engineering*, vol. 47, pp. 15–30, Jan. 2005.
- [187] S. Hardinata, F. Deshours, G. Alquie, H. Kokabi, and F. Koskas, ‘Biosensor miniaturization for non-invasive measurements of materials and biological tissues’, in *2017 International Seminar on Sensors, Instrumentation, Measurement and Metrology (ISSIMM)*, Surabaya: IEEE, Aug. 2017, pp. 137–140. doi: 10.1109/ISSIMM.2017.8124278.
- [188] M. Wellenzohn and M. Brandl, ‘A Theoretical Design of a Biosensor Device Based on Split Ring Resonators for Operation in the Microwave Regime’, *Procedia Engineering*, vol. 120, pp. 865–869, 2015, doi: 10.1016/j.proeng.2015.08.737.
- [189] J. D. Baena *et al.*, ‘Equivalent-circuit models for split-ring resonators and complementary split-ring resonators coupled to planar transmission lines’, *IEEE Transactions on Microwave Theory and Techniques*, vol. 53, no. 4 II, pp. 1451–1460, Apr. 2005, doi: 10.1109/TMTT.2005.845211.
- [190] E. L. Chuma, Y. Iano, G. Fontgalland, and L. L. Bravo Roger, ‘Microwave sensor for liquid dielectric characterization based on metamaterial complementary split ring resonator’, *IEEE Sensors Journal*, vol. 18, no. 24, pp. 9978–9983, Dec. 2018, doi: 10.1109/JSEN.2018.2872859.
- [191] S. Hardinata, F. Deshours, G. Alquié, H. Kokabi, and F. Koskas, ‘Miniaturization of Microwave Biosensor for Non-invasive Measurements of Materials and Biological Tissues’, in *International Seminar on Sensors, Instrumentation, Measurement and Metrology (ISSIMM)*, 2017, pp. 137–140. doi: 10.1109/ISSIMM.2017.8124278.
- [192] L. Saba *et al.*, ‘Carotid Artery Wall Imaging: Perspective and Guidelines from the ASNR Vessel Wall Imaging Study Group and Expert Consensus Recommendations of the American Society of Neuroradiology’, *Am. J. Neuroradiol.*, vol. 39, no. 2, p. E9, Feb. 2018, doi: 10.3174/ajnr.A5488.
- [193] Carotide, ‘Endartériectomie carotidienne par éversion type Van Mahle’, *Carotide/Chirurgiens/Institut Mutualiste Montsouris*. <https://www.carotide.com/technique-endarteriectomie-carotidienne-par-eversion-type-van-mahle/>
- [194] L. Ali *et al.*, ‘Design and Optimization of Microwave Sensor for the Non-Contact Measurement of Pure Dielectric Materials’, *Electronics*, vol. 10, no. 24, p. 3057, Dec. 2021, doi: 10.3390/electronics10243057.
- [195] F. Shanehsazzadeh, N. Azizi, H. K. Haghghat, F. Mashayekhi, and M. Fardmanesh, ‘Cost-Effective Flexible CSRR-Based Sensor for Noninvasive Measurement of Permittivity of Biomaterials’, in *The 8th International Electronic Conference on Sensors and Applications*, MDPI, Nov. 2021, p. 26. doi: 10.3390/ecsa-8-11303.
- [196] F. Cademartiri *et al.*, ‘Insight from imaging on plaque vulnerability: similarities and differences between coronary and carotid arteries—implications for systemic therapies’, *Cardiovasc Diagn Ther*, vol. 10, no. 4, pp. 1150–1162, Aug. 2020, doi: 10.21037/cdt-20-528.

- [197] W. J. Krzanowski, *Roc Curves For Continuous Data*. S.I.: CRC PRESS, 2023.
- [198] W. Mendenhall, R. J. Beaver, and B. M. Beaver, *Introduction to probability and statistics*, 14th ed./Student edition. Boston, MA, USA: Brooks/Cole, Cengage Learning, 2013.
- [199] M. Szumilas, ‘Explaining odds ratios’, *J Can Acad Child Adolesc Psychiatry*, vol. 19, no. 3, pp. 227–229, Aug. 2010.
- [200] G. Geroulakos *et al.*, ‘Characterization of symptomatic and asymptomatic carotid plaques using high-resolution real-time ultrasonography’, *British Journal of Surgery*, vol. 80, no. 10, pp. 1274–1277, Oct. 1993, doi: 10.1002/bjs.1800801016.
- [201] L. Saba, R. Sanfilippo, R. Montisci, M. Atzeni, D. Ribuffo, and G. Mallarini, ‘Vulnerable plaque: Detection of agreement between multi-detector-row CT angiography and US-ECD’, *European Journal of Radiology*, vol. 77, no. 3, pp. 509–515, Mar. 2011, doi: 10.1016/j.ejrad.2009.09.009.
- [202] H. R. Tahmasebpour, A. R. Buckley, P. L. Cooperberg, and C. H. Fix, ‘Sonographic Examination of the Carotid Arteries’, *RadioGraphics*, vol. 25, no. 6, pp. 1561–1575, Nov. 2005, doi: 10.1148/rg.256045013.
- [203] A. Casadei, M. Floreani, R. Catalini, C. Serra, A. P. Assanti, and P. Conci, ‘Sonographic characteristics of carotid artery plaques: Implications for follow-up planning?’, *Journal of Ultrasound*, vol. 15, no. 3, pp. 151–157, Sep. 2012, doi: 10.1016/j.jus.2012.06.002.
- [204] Y. Watanabe *et al.*, ‘Characterization of atherosclerotic plaque of carotid arteries with histopathological correlation: Vascular wall MR imaging vs. color Doppler ultrasonography (US)’, *Journal of Magnetic Resonance Imaging*, vol. 28, no. 2, pp. 478–485, Aug. 2008, doi: 10.1002/jmri.21250.
- [205] S. Zhang, X. Yu, H. Gu, B. Kang, N. Guo, and X. Wang, ‘Identification of high-risk carotid plaque by using carotid perivascular fat density on computed tomography angiography’, *European Journal of Radiology*, vol. 150, p. 110269, May 2022, doi: 10.1016/j.ejrad.2022.110269.
- [206] M. Yu *et al.*, ‘Associations between pericarotid fat density and image-based risk characteristics of carotid plaque’, *European Journal of Radiology*, vol. 153, Aug. 2022, doi: 10.1016/j.ejrad.2022.110364.
- [207] W. C. Vieira de Castro, H. Röcklinsberg, M. Gjerris, and I. A. S. Olsson, ‘The 3Rs and Good Scientific Practice’, in *Animal Ethics in Animal Research*, Cambridge University Press, 2017, pp. 15–40. doi: 10.1017/9781108354882.004.
- [208] D. M. Hagl, D. Popovic, S. C. Hagness, J.H. Booske, and M. Okoniewski, ‘Sensing volume of open-ended coaxial probes for dielectric characterization of breast tissue at microwave frequencies’, *IEEE Transactions on Microwave Theory and Techniques*, vol. 51, no. 4, pp. 1194–1206, Apr. 2003, doi: 10.1109/TMTT.2003.809626.
- [209] R. Istfan, C. A. Gómez, M. Applegate, D. Rozenberg, W. D. Reid, and D. Roblyer, ‘Hemodynamics of the sternocleidomastoid measured with frequency domain near-infrared spectroscopy towards non-invasive monitoring during mechanical ventilation’, *Biomedical Optics Express*, vol. 12, no. 7, p. 4147, Jul. 2021, doi: 10.1364/boe.430423.
- [210] K. Chopra *et al.*, ‘A comprehensive examination of topographic thickness of skin in the human face’, *Aesthetic Surgery Journal*, vol. 35, no. 8, pp. 1007–1013, Nov. 2015, doi: 10.1093/asj/sjv079.

- [211] H.-J. Lee and J.-M. Song, ‘Deep Neck Flexor and Sternocleidomastoid Muscle Thickness Change in Persons with No Current Neck Pain using Rehabilitative Ultrasonographic Imaging’, *The Journal of Korean Physical Therapy*, vol. 28, no. 6, pp. 349–354, Dec. 2016, doi: 10.18857/jkpt.2016.28.6.349.
- [212] A. Palmer, ‘The Anatomy of the Skin, Your largest organ protects, regulates heat, and provides sensation’, *Verywell Health*, Feb. 2020. <https://www.verywellhealth.com/skin-anatomy-4774706>
- [213] S. Gabriel, R. W. Lau, and C. Gabriel, ‘The dielectric properties of biological tissues: III. Parametric models for the dielectric spectrum of tissues’, *Phys. Med. Biol.*, vol. 41, no. 11, pp. 2271–2293, Nov. 1996, doi: 10.1088/0031-9155/41/11/003.
- [214] D. Dubuc, K. Grenier, F. Morfoisse, and B. Susini-Garmy, ‘In vitro and in vivo investigations toward near-field microwave-based detection of melanoma’, in *2017 First IEEE MTT-S International Microwave Bio Conference (IMBIOC)*, Gothenburg, Sweden: IEEE, May 2017, pp. 1–4. doi: 10.1109/IMBIOC.2017.7965789.
- [215] M. O’halloran, F. Morgan, D. Flores-Tapia, D. Byrne, M. Glavin, and E. Jones, ‘Ultra Wideband Radar System For Bladder Monitoring Applications’, *Progress In Electromagnetics Research C*, vol. 33, pp. 17–28, 2012.
- [216] D. Tommasin, A. Caenen, B. Verheghe, S. Greenwald, and P. Segers, ‘Physics of within-tissue wave propagation generated by pulse propagation in the carotid artery’, *Applied Sciences (Switzerland)*, vol. 9, no. 14, Jul. 2019, doi: 10.3390/app9142878.
- [217] D. Ireland and M. Bialkowski, ‘Microwave Head Imaging For Stroke Detection’, *Progress In Electromagnetics Research M*, vol. 21, pp. 163–175, 2011, doi: 10.2528/PIERM11082907.
- [218] R. Scapaticci, O. M. Bucci, I. Catapano, and L. Crocco, ‘Differential microwave imaging for brain stroke followup’, *International Journal of Antennas and Propagation*, vol. 2014, 2014, doi: 10.1155/2014/312528.
- [219] V. Mancini *et al.*, ‘Detecting carotid stenosis from skin vibrations using Laser Doppler Vibrometry – An in vitro proof-of-concept’, *PLoS ONE*, vol. 14, no. 6, Jun. 2019, doi: 10.1371/journal.pone.0218317.
- [220] M. D. Perez *et al.*, ‘Head-compliant microstrip split ring resonator for non-invasive healing monitoring after craniostylosis-based surgery’, *Healthcare Technology Letters*, vol. 7, no. 1, pp. 29–34, Feb. 2020, doi: 10.1049/htl.2018.5083.

Publications associated with this research

Journal articles

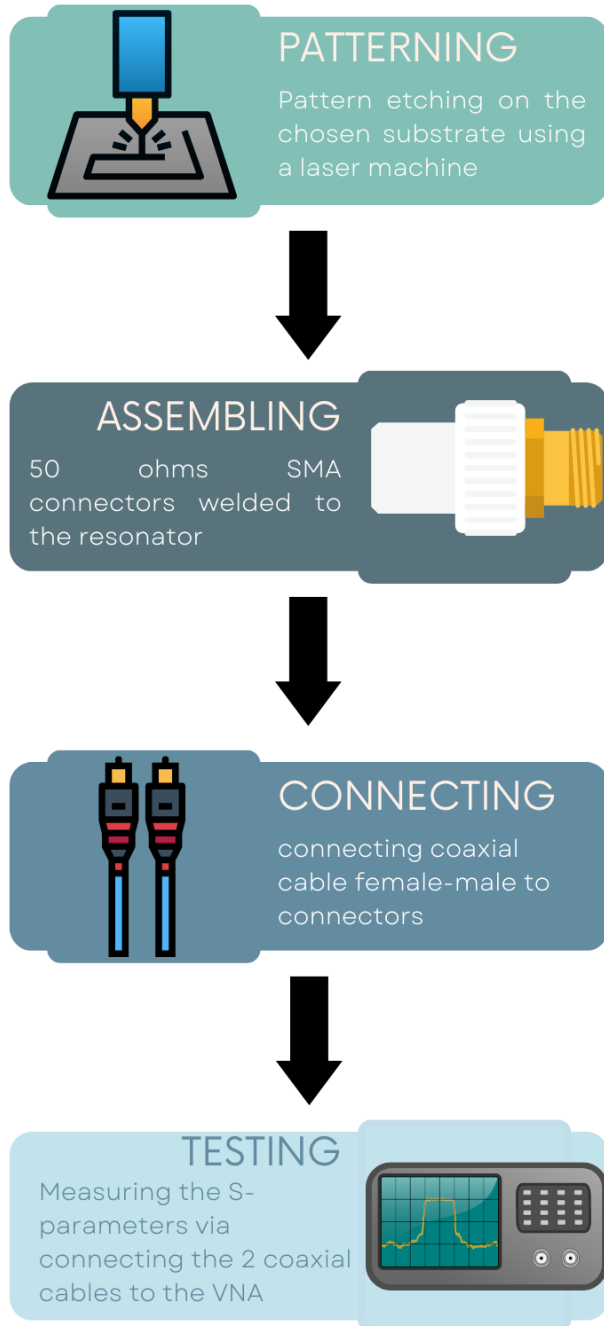
- [1] **R. Shahbaz**, F. Deshours, G. Alquie, H. Kokabi, F. Koskas, I. Brocheriou, G. Le Naour, C. Hannachi, J.-M. Davaine, "Identification of Carotid Plaques Composition Through a Compact CSRR-Based Microwave Sensor", *IRBM*, 2022, 100734, ISSN 1959-0318, <https://doi.org/10.1016/j.irbm.2022.09.001>
- [2] K. Abdesselam, C. Hannachi, **R. Shahbaz**, F. Deshours, G. Alquie, H. Kokabi, A. Omer, J.-M. Davaine, "A Non-Invasive Honey-Cell CSRR Glucose Sensor: Design Considerations and Modelling", *IRBM*, Vol. 44, no.1, 2023, 100713, ISSN 1959-0318, <https://doi.org/10.1016/j.irbm.2022.04.002>

Conference Proceedings

- [1] J.Masini, **R.Shahbaz**, F.Deshours, G.Alquié, S.Feruglio, O.Meyer, D.Galayko, H.Kokabi et J-M.Davaine, "Capteur micro-ondes en vue du diagnostic médical de l'athérosclérose. *JETSAN Colloque en TéléSANTé et dispositifs biomédicaux*. Paris. Juin. 2023.
- [2] **R. Shahbaz**, E. Charpentier, G. Le Naour, I. Brocheriou, F. Koskas, J-M. Davaine, and A. Redheuil, "Perivascular fat attenuation of carotid arteries assessed with CTA in preoperative patients: comparison between symptomatic and asymptomatic patients," *ESVB - The European Symposium on Vascular Biomaterials 2023*.
- [3] **R. Shahbaz**, E. Charpentier, F. Koskas, I. Brocheriou, G. Le Naour, J-M. Davaine, and A. Redheuil, "Can we really detect vulnerable carotid atherosclerotic plaques by routine ultrasound?," *Ultrasound 2022, British Medical Ultrasound (BMUS) Annual Scientific Meeting* – Cardiff. Dec. 2022.
- [4] J. Masini, **R. Shahbaz**, F. Deshours, G. Alquié, C. El bastami and H. Kokabi, "Penetration Depth in Multilayered Biological Tissues using a Compact Microwave Biosensor," *2022 52nd European Microwave Conference (EuMC)*, Milan, Italy, 2022, pp. 408-411, doi: 10.23919/EuMC54642.2022.9924283.
- [5] J-M. Davaine, A. Redheuil, E. Charpentier, I. Brocheriou, F. Koskas and **R. Shahbaz**, "The IMPPACT study: Imaging and Microwave Potential to Predict Asymptomatic Carotid Stenosis Treatment," *Ann. Vasc. Surg.*, vol. 84, pp. 80–81, Aug. 2022, doi: 10.1016/j.avsg.2022.06.043.
- [6] C. El Bastami, **R. Shahbaz**, J. Masini, F. Deshours, G. Alquié, H. Kokabi, F. Koskas, J-M. Davaine, "Caractérisation diélectrique de tissus biologiques multicouches à l' aide d'un biocapteur micro-ondes," *XXII èmes Journées Nationales Microondes 8-10 juin 2022* – Limoges. pp. 8–10, Nov. 2022.

- [7] **R. Shahbaz**, F. Deshours, I. Brocheriou, E. Charpentier, A. Redheuil, G. Le Naour, K. Kokabi, F. Koskas, and J-M. Davaine, "Imaging and Microwave Potential to Predict Asymptomatic Carotid stenosis Treatment". *ESVB - The European Symposium on Vascular Biomaterials 2021* – Strasbourg. Nov. 2021.
- [8] **R. Shahbaz**, C. Hannachi, F. Deshours, K. Kokabi, G. Alquié, I. Brocheriou, G. Le Naour, F. Koskas, and J-M. Davaine, "Conversion Loss Analysis in CSRR-Based Microwave Sensors for Carotid Plaques Characterization," *2021 4th International Conference on Bio-Engineering for Smart Technologies (BioSMART)*, 2021, pp. 1-4, doi: 10.1109/BioSMART54244.2021.9677745.
- [9] **R. Shahbaz**, C. Hannachi, F. Deshours, K. Kokabi, G. Alquié, I. Brocheriou, G. Le Naour, F. Koskas, and J-M. Davaine, "Diagnosis of atheromatous Carotid Plaque: Dielectric Constant Measurement Using Microwave Resonant Technique versus Ultrasound B-mode Images," 2021 USNC-URSI Radio Science Meeting (USNC-URSI RSM), 2021, pp. 040-044, doi: 10.23919/USNC-URSIRSM52661.2021.9552356.
- [10] **R. Shahbaz**, F. Deshours, G. Alquie, H. Kokabi, O. Meyer, and F. Koskas. J-M. Davaine, "Application d'un biocapteur micro-ondes pour la caractérisation de plaques carotidiennes athéromateuses," *JCMM*. pp. 2–5, 2020.

Appendix 1

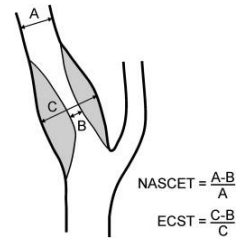


Appendix 1 Fabrication process of the CSRR

Appendix 2

Échographie Doppler TSA

NOM:..... IPP:..... Date:...../...../20.....



Etude morphologique

- Siège par rapport aux bifurcations.....
- Disposition (latérale, médiale, circonférentielle, centrée, excentrée)
- NASCET / ECST: A =, B =, C =

Echogénicité:

1. uniformément anéchoïque
2. à prédominance anéchogène ou hypoéchogène
3. à prédominance isoéchogène ou hyperéchogène
4. uniformément isoéchogène ou hyperéchogène
5. plaque calcifiée (avec ombre acoustique / sans ombre acoustique)

Surface de la plaque:

1. Lisse, régulière
2. présence de chape fibreuse ou non
3. Irrégulière (variations des contours de 0,4 à 1 mm),
4. Anfractuosité (présence d'un cratère >2 mm de profondeur) – niche d'au moins 2mm de large sur 2mm de profondeur remplie sans aliasing par la couleur avec un fond bien défini
5. Plaques successives

Etude hémodynamique

Côté opéré: (droit – gauche)

PSV/EDV

CCA (PSV 3cm prior to the bifurcation)/..... cm/s

ICA (PSV dans la sténose - segment le plus serré)/..... cm/s

ICA/ CCA ratio/.....

ICA post stenosis/..... cm/s

Flux en aval:

- Normale
- Turbulente
- Démodulé TMS > 0.7 sec (Turbulence meso-systolique)

carotid web – dissection – DFM -

Appendix 3

Analyse des plaques carotidiennes Etude IMPPACT

Patient n° : 13

Fibrose

peu intermédiaire beaucoup ne sait pas

Inflammation

peu intermédiaire beaucoup ne sait pas

Calcification

peu intermédiaire beaucoup ne sait pas
 intimales médiales les 2 ne sait pas

Nécrose

peu intermédiaire large cœur nécrotique
 ne sait pas

Lipide

peu intermédiaire beaucoup
 ne sait pas

Hémorragie intraplaque

présence absence ne sait pas

Au total cette plaque est selon vous Stable

oui non ne sait pas

Symptomatique

oui non ne sait pas



List of figures

<i>Figure 1. Types of strokes: Ischemic and Haemorrhagic [5]</i>	16
<i>Figure 2. Fatty deposits lining the wall of the carotid artery.</i>	17
<i>Figure 3. Anatomical dissection of a carotid bifurcation with an atherosclerotic plaque [21]</i>	18
<i>Figure 4. Differences between NASCET and ECST in the measurement of internal CAS [31]</i>	20
<i>Figure 5. Plaque composition analysis by GSM and Pixel Distribution Analysis (PDA) [61]</i>	27
<i>Figure 6. On a colour map of the HU (B) at the same level as a sagittal section of carotid artery stenosis (A), the inner area of plaque was colour-coded based on the HU. An HU of 130–250 reflects contrast medium in the vascular lumen. Of solid-line sections (C) source image, (D) colour map, (E) time-of-flight image, there was no IPH on the time-of-flight image, and CT showed a red area with an HU of ≤ 0 (dotted arrows). Of dotted-line sections (F) source image, (G) colour map, (H) time-of-flight image, intraplaque haemorrhage was detected on the time-of-flight image. CT confirmed the disappearance of the area with an HU of ≤ 0 (arrows) [75].</i>	30
<i>Figure 7. The ICG-based neovessel appearance is categorized into three groups.</i>	34
<i>Figure 8. Carotid atherosclerotic plaque progression from pathologic intimal thickening with acellular lipid pools to plaque rupture. (A) Early lipid pool (LP) lesion. (B, C) Fibroatheromatous plaque with an early and late necrotic core (NC), respectively. The early NC in (B) shows macrophages and a proteoglycan-rich matrix (light blue-green), while the late core shows mainly cholesterol (as noted in the higher power “c”) with a few surrounding macrophages and a generalized absence of extracellular matrix. (D) IPH can lead to the rapid expansion of the necrotic core and lesion progression through erythrocyte-derived free cholesterol and secondary inflammation. (E) Vulnerable or thin-cap fibroatheroma, a precursor lesion to plaque rupture characterized by a relatively thin fibrous cap (Thin-FC). (F) “Ulcerated” and (G) “luminal thrombus” represent two different presentations of plaque rupture where invariably, the intraluminal thrombus for the latter is relatively small and absent for the ulcerated plaque. The ulcerated plaque is from a patient with symptomatic stroke; the site of ulceration (arrow) represents a portion of the plaque where the fibrous cap and necrotic core are likely embolized [42].</i>	38
<i>Figure 9. EM waves spectrum [95]</i>	43
<i>Figure 10. Schematic view of the TAI system [98].</i>	45
<i>Figure 11. Breast cancer diagnosis with microwave-induced TAI [101]</i>	45
<i>Figure 12. (a) Envisioned wearable bra microwave radar. (b) Antenna arrangement in prosthetic bra for volunteer testing. (c) Current antenna arrangement in the 3D-printed hemisphere for phantom testing [109].</i>	50
<i>Figure 13. Microwave helmet to diagnose stroke.</i>	51
<i>Figure 14. Illustration of the portable radar-driven sensor for measuring the glucose level non-invasively from the fingertip [146].</i>	53
<i>Figure 15. A summary of some of the microwave approaches being developed for medical applications.</i>	55
<i>Figure 16. Cole-Cole diagram of a material with conductivity</i>	59

Figure 17. The frequency range of dielectric mechanisms contributing to dielectric permittivity [152].	60
Figure 18. Permittivity and conductivity of blood: prediction of the model (black filled and dotted curves), experimental data at 37C (grey filled and dotted curves) and data from the literature (triangles and circles) [157]	64
Figure 19. Different existing types and models of the VNA [179]	68
Figure 20. S-parameter theory [181]	69
Figure 21. Coaxial probe method [152]	70
Figure 22. Transmission line method [180]	71
Figure 23. Free space method [180]	71
Figure 24. Resonant cavity measurement [186]	73
Figure 25. Comparison between the measurement methods [152].	73
Figure 26. Design of structures (a) SRR (b) CSRR	75
Figure 27. CSRR dimensions	76
Figure 28. $ S_{11} $ and $ S_{21} $ of the retro simulation of the resonator vs real measurements	77
Figure 29. Equivalent electrical schema of the resonator	78
Figure 30. Graph comparing the modelling on ADS with the simulation on HFSS and the experimental measurements.	79
Figure 31. Design of the structure with glass slab for EM simulations with HFSS:	80
Figure 32. The CSRR covered with the glass blade and inserted inside the plexiglass structure.	80
Figure 33. Simulation of superstrates of two different thicknesses using HFSS and CST	82
Figure 34. Δf_r as a function of the ϵ_{rs}	82
Figure 35. Saturation effect observed as the thickness increases	83
Figure 36. Carotid artery stenosis quantification using the NASCET methodology (72% stenosis noticed here)	86
Figure 37. Plaque characterization with Terarecon software in a 85-year-old patient. After the segmentation of the right carotid artery plaque, the software calculated the three different components using HU threshold: fibrofatty (<60HU), fibrotic (60-130 HU).	87
Figure 38. PVFA measurement with two ROIs placed on an axial plane at the level of maximal stenosis in an 85 years old patient.	87
Figure 39. a) Transverse photo of an irregular heterogeneous plaque b) the same plaque in a longitudinal view showing acoustic shadowing. c) Colour Doppler was used to visualise the hypoechoic regions of a heterogeneous hypoechoic plaque. d) The same plaque without colour Doppler challenging to visualize the entire plaque.	89
Figure 40. Van Mahle Eversion carotid endarterectomy technique [193]	90
Figure 41. HD photos of a few plaques of different natures included in the questionnaire. ...	91
Figure 42. Semi-quantitative analysis of each plaque	92
Figure 43. Qualitative analysis of the entire plaque	93
Figure 44. The scale, calliper and cutter used to prepare the carotid plaque samples before insertion in the Plexiglas structure	94
Figure 45. The pressure sensor prototype developed by Polytech Sorbonne engineering students.	95

<i>Figure 46. The pressure sensor with its box printed by a 3D printer and the Plexiglas structure with a resonator inside locked in and covered with the piston.....</i>	<i>96</i>
<i>Figure 47. Measurement and simulation results of a soft plaque (d is the thickness of the plaque). The calculated permittivity and tangent loss values are in the blue box.</i>	<i>97</i>
<i>Figure 48. Measurement and simulation results of a hard plaque (d is the thickness of the plaque). The calculated permittivity and tangent loss values are in the blue box.</i>	<i>97</i>
<i>Figure 49. Average $\Delta f = 465$ MHz in the symptomatic group (curve in black is the measurement of the resonator empty with the glass layer and the Plexiglas structure).....</i>	<i>98</i>
<i>Figure 50. Average $\Delta f = 505$ MHz in the asymptomatic group (curve in black is the measurement of the resonator empty with the glass layer and the Plexiglas structure).....</i>	<i>99</i>
<i>Figure 51. IPH bordered in black.</i>	<i>104</i>
<i>Figure 52. OM region encircled in black.</i>	<i>105</i>
<i>Figure 53. Statistical analysis of Gray-Weale classification vs calcification levels in histology</i>	<i>106</i>
<i>Figure 54. Statistical analysis of Gray-Weale classification vs LRNC levels in histology....</i>	<i>108</i>
<i>Figure 55. Box plot (whisker chart) analysis of HU groups vs symptoms.....</i>	<i>110</i>
<i>Figure 56. Box plot (whisker chart) analysis of HU groups vs VP&NVP, i.e. stable group .</i>	<i>111</i>
<i>Figure 57. Box plot analysis of the PVFA vs symptoms and VP & NVP groups.</i>	<i>112</i>
<i>Figure 58. Box plot analysis of HU groups vs Gray-Weale groups in DUS.....</i>	<i>113</i>
<i>Figure 59. Whisker chart of the dielectric constant vs symptoms, VP and NVP groups</i>	<i>114</i>
<i>Figure 60. Whisker chart and ROC curve statistical analysis of the dielectric constant vs DUS echogenicity types.</i>	<i>114</i>
<i>Figure 61. Multimodel prognostic score to predict better the vulnerability of carotid plaques.</i>	<i>117</i>
<i>Figure 62. The VP in (A) shows similar findings between the in-vivo examination of DUS and CT (B,C), respectively and the histological analysis in (D). Similarly, the NVP in (E) displays comparable findings between the in-vivo assessment of DUS and CT (F,G), respectively and the histological analysis in (H).</i>	<i>118</i>
<i>Figure 63. The neck anatomy.....</i>	<i>127</i>
<i>Figure 64. The neck layers' thickness, according to [209]</i>	<i>128</i>
<i>Figure 65. The three layers of the skin [212].....</i>	<i>129</i>
<i>Figure 66. Measurements and HFSS simulations of the pig skin layers.....</i>	<i>130</i>
<i>Figure 67. Measurements and simulations of the pig fat layer.....</i>	<i>131</i>
<i>Figure 68. Measurements and HFSS simulations of the pig muscle layer</i>	<i>132</i>
<i>Figure 69. Multilayer model of pig tissues placed on the resonator.</i>	<i>132</i>
<i>Figure 70. Measurement, simulation, and optimisation of the pig multilayer model.....</i>	<i>133</i>
<i>Figure 71. Multilayer model of (skin, fat, and muscle), the upper part of the Plexiglas was removed for picture purposes.....</i>	<i>134</i>
<i>Figure 73. (a) The common carotid artery (CCA) geometry is embedded within a cuboidal domain. The free (skin) surface is dark grey, while infinite mesh elements placed on the outer boundaries are light grey. (b) Geometry of the patient-specific CA embedded within a cuboidal domain. Sub-regions common carotid artery, CCA; bifurcation, BIF; ICA and external carotid artery, ECA are indicated [216].</i>	<i>138</i>

Figure 74. (A) CTA images of the carotid bifurcation from a 75-year-old male were processed to obtain a patient-specific model of the plaque-free stenosed vessel. The compliant (B) and stiff (C) models used for the hydraulic tests replicate the geometry of the patient-specific common carotid artery (CCA), external carotid artery (ECA), and ICA where the 76% area stenosis (circled) is located [219]. 139

Figure 75. Distribution of electric field after simulation of the sensor on a phantom with CST and the simulated resonance frequency curve of the antenna with head phantom, with variation in dielectric constant from 18 to 68 [220]. 139

Figure 76. The LifeLike VI Embedded Carotid Arteries with Plaque..... 140

List of tables

<i>Table 1. ESVS listed the imaging features associated with an increased risk of stroke in patients with asymptomatic 50-99% CAS treated medically [47].....</i>	24
<i>Table 2. Summary of few inflammatory biomarkers associated with plaque progression and instability.....</i>	36
<i>Table 3. Comparison of multi-modality imaging techniques for the assessment of arterial plaque [63]</i>	40
<i>Table 4. Current evidence of the use of the imaging technique for the detection of features of vulnerability [90].....</i>	41
<i>Table 5. The permittivity and conductivity of several biological tissues at 2.2 GHz Blue [156], yellow [157].....</i>	62
<i>Table 6. Extracted parameters of the equivalent electrical model of the resonator empty</i>	78
<i>Table 7. Equivalent electrical parameters of the resonator with glass slab and Plexiglas mount.</i>	81
<i>Table 8. The values collected and calculated for each plaque</i>	93
<i>Table 9. Demographics and cardiovascular comorbidities</i>	102
<i>Table 10. The number of histologically based VP and NVP in the symptomatic and asymptomatic group</i>	103
<i>Table 11. Risk factors and comorbidities in the vulnerable vs stable group</i>	103
<i>Table 12. Composition of the plaques in the VP vs NVP group and symptomatic vs asymptomatic group</i>	103
<i>Table 13. HU components and PVFA in the VP vs NVP group and symptomatic vs asymptomatic group (SD= standard deviation).....</i>	109
<i>Table 14. Statistical analysis of the dielectric constant in the different groups of patients... </i>	113
<i>Table 15. Multivariate analysis to predict VP.</i>	115
<i>Table 16. The frequency shift, dielectric constant, and losses of the first pig samples</i>	130
<i>Table 17. The parameters recorded during the experiment and the extracted results of the pig sample.....</i>	135
<i>Table 18. Dimensions of the carotid phantom used (ID = Inside Diameter, OD= Outside diameter)</i>	140
<i>Table 19. First practical measures of the skin phantom</i>	141

Résumé

Conception et mise en œuvre d'un biocapteur miniaturisé à micro-ondes pour le diagnostic de l'athérosclérose carotidienne

Mots clés : [capteur, microonde, carotide, CSRR]

L'imagerie par micro-ondes suscite une grande attention dans le domaine médical en raison de sa capacité à pénétrer dans le corps et à différencier les propriétés diélectriques des tissus humains, ce qui permet de distinguer les tissus anormaux des tissus sains. Dans cette thèse, un biocapteur micro-ondes miniaturisé, capable de quantifier la permittivité relative des tissus biologiques, est utilisé en raison de ses nombreux avantages tels que la portabilité, la simplicité de conception, le faible coût et l'absence de risques pour le praticien et le patient. Basé sur une structure CSRR, il a été développé pour mesurer localement la composition des plaques d'athérosclérose dans l'artère carotidienne.

Les premiers tests du capteur ont été effectués sur une cinquantaine de plaques d'athérosclérose de la carotide. L'histologie, le scanner et l'échographie des lésions des patients ont été effectués pour valider les résultats du capteur. Une analyse statistique complète a été réalisée pour corréler les résultats des micro-ondes à l'histologie et les comparer aux techniques radiologiques actuelles. Par ailleurs, le biocapteur a été utilisé pour caractériser une variété de tissus animaux afin de simuler le modèle du cou humain. Il a aussi été utilisé par comparaison pour caractériser un fantôme de cou humain. Les données préliminaires ont été comparées aux résultats de la modélisation électromagnétique et des simulations 3D du biocapteur chargé par les matériaux testés. Le prototype original du capteur ayant été conçu sur un substrat relativement à forte pertes, sa sensibilité est limitée en profondeur et nécessite de développer d'autres CSRRs mieux adaptés à la détection de tissus plus épais.

Les résultats de simulation électromagnétique du biocapteur sont tout à fait comparables aux données expérimentales. Ils ont permis de montrer que le biocapteur pouvait distinguer les plaques carotidiennes à haut risque de celles à faible risque et caractériser les couches biologiques individuelles, mais qu'il manquait de précision pour les modèles multicouches.